University of Nevada, Reno

A 3D Characterization of the Astor Pass Geothermal System, Washoe County, Nevada

A thesis submitted in partial fulfillment of the
requirements for the degree of Master of Science in Geology

by

Brett A. Mayhew

Dr. James E. Faulds/Thesis Advisor

August, 2013

University of Nevada, Reno
Statewide • Worldwide

THE GRADUATE SCHOOL

We recommend that the thesis
prepared under our supervision by

BRETT A. MAYHEW

entitled

3D Characterization Of The Astor Pass Geothermal System, Washoe County, Nevada

be accepted in partial fulfillment of the
requirements for the degree of

MASTER OF SCIENCE

James E. Faulds, Phd, Advisor

John Louie, Phd, Committee Member

Jill Heaton, Phd, Graduate School Representative

Marsha H. Read, Ph. D., Dean, Graduate School

August, 2013

Abstract

Seismic reflection interpretation, detailed analysis of well cuttings, stress field analysis, and construction of a 3D geologic model have been used in the characterization of the stratigraphic and structural framework of the Astor Pass geothermal area. The Astor Pass geothermal system resides in the northwestern part of the Pyramid Lake Paiute Reservation, on the margins of the Basin and Range and Walker Lane tectonic provinces in northwestern Nevada. The area is primarily comprised of middle Miocene Pyramid sequence volcanic and sedimentary rocks, nonconformably overlying Mesozoic metamorphic and granitic rocks. Previous investigations of the Astor Pass area focused on the general structural setting, argillic alteration of the Miocene rocks, lineations of Quaternary tufa mounds, and a shallow temperature survey. Wells drilled at Astor Pass show reservoir temperatures of ~95°C. Analyses of well cuttings show a ~1 km thick section of highly transmissive and permeable Miocene volcanic and sedimentary rocks overlying a relatively impermeable granodiorite and metavolcanic basement. Seismic reflection interpretation confirms a high fault density in the geothermal area, with many possible fluid pathways penetrating into the Mesozoic basement.

Stress field analysis using borehole breakout data from the wells reveals a regionally consistent west-northwest-trending least principal stress direction, with stress magnitudes reflecting a complex transtensional faulting regime. A lack of data on the mechanical properties of the reservoir rocks, such as strength parameters, results in some ambiguity in the calculated stress field. However, reasonable assumptions regarding these variables produced both a normal faulting and strike-slip faulting regime.

Taking into consideration both possible stress regimes, the stress data were utilized in a slip and dilation tendency analysis of the fault model, which suggests two promising fault areas that would control the upwelling geothermal fluid. The first is a moderately dipping fault intersection plunging to the northwest away from the prominent tufa mound in the center of Astor Pass. The second subvertical fault intersection is directly beneath the tufa mound and closest to the highest temperatures measured in the geothermal system. Both of these fault intersection areas show positive attributes for controlling geothermal fluids, but hydrologic tests show the 1 km thick volcanic section is highly transmissive. Thus, focused upwellings along discrete fault conduits may be confined to the Mesozoic basement before fluids diffuse into the Miocene volcanic reservoir above.

Astor Pass contains a moderate temperature geothermal system with a large, diffuse reservoir in the Miocene volcanic rocks, capable of sustaining high pump rates. Understanding this type of system may be helpful in exploring for large, permeable reservoirs in deep sedimentary basins of the eastern Basin and Range and the highly fractured volcanic geothermal reservoirs in the Snake River Plain and elsewhere.

Acknowledgments

Foremost I would like to thank my advisor, Dr. James Faulds, who encouraged and facilitated my interest in structural geology, modeling, and fluid movement in geothermal systems by offering his mentorship, wisdom, wit, and constructive criticism during this project. I would like to thank Nick Hinz for help with drill cuttings and general musings of the Walker Lane. Thank you to Drew Siler for extensive help and collaboration in building the Astor Pass 3D model. Thank you David McNamara for your work on interpreting borehole breakouts. Thank you to Robert McFaul for support with EarthVision software. I thank the Pyramid Lake Paiute Tribe for sharing seismic reflection data, well logs, and allowing access to the field area, with special thanks to Donna Noel for helping facilitate this research on the tribal lands. Thank you to John Louie for help with software, seismic reflection interpretation, and contributions as a committee member. I also thank Jill Heaton as a thoughtful committee member. Thank you to Garrett Vice for all of your previous work in the Astor Pass area. Thank you to Greg Dering, Ryan Anderson, and Sean Long for extensive and sometimes silly rambling regarding fluid flow and the upper crust in general. This work was supported by a Department of Energy American Recovery and Reinvestment Act grant (EE0002842) awarded to the Pyramid Lake Paiute Tribe, along with grants from the Nevada Petroleum and Geothermal Society and Exxon Mobil. I would like to thank my parents for their support, and finally, Emily Seider, for her encouragement, tolerance and constant support.

Table of Contents

List of Figures

Introduction

The Great Basin region in the western USA contains an unusual combination of geologic features that foster geothermal activity, including an anomalously high geothermal gradient, active faulting, and regional extension. Although the northern Basin and Range has experienced active volcanism as recently as 10 to 3 Ma, this volcanism is thought to have little effect on the current geothermal gradient (Blackwell, 1983; Faulds et al., 2006). Only a small number of systems (e.g., Roosevelt Hot Springs, Coso, and Steamboat) on the margins of the Great Basin show evidence of active magmatism (Figure 1). Thus, the majority of the ~430 known geothermal systems in the Great Basin (Faulds et al., 2011a) are considered amagmatic, relying on elevated crustal heat flow of ~75±5 mWm-2 and deep fluid circulation and pathways to the surface via faults (Blackwell, 1983; Curewitz and Karson, 1997; Faulds et al., 2006). The high crustal heat flow is likely the result of the regional extension, which has thinned the crust to ~30 km in most areas (Blackwell et al., 2007; Henry et al., 2011).

Recent studies of over 300 of the geothermal systems in the Great Basin region have shown that certain structural settings act as more effective conduits for these deep-seated fluids. Steeply dipping normal faults that have discrete steps, terminations, intersections with other faults (including oppositely dipping normal faults), or reside in transtensional pull-aparts are the preferred settings. Fault steps or relay ramps (cf., Larsen, 1988) are the most common setting and appear to control roughly 1/3 of the systems studied (Figure1) (Faulds et al., 2006, 2010, 2011a; Vice et al., 2007; Hinz et al., 2008, 2010, 2011). These fault geometries generate favorable subvertical, high- fault and

-fracture density zones that act as preferential fluid pathways (Curewitz and Karson, 1997; Faulds et al., 2006). The fluid flow in these fault zones is formed and maintained by continued slip and dilation, further increased when critically stressed with respect to the ambient stress conditions (Ferrill and Morris, 2003; Moeck et al., 2009).

In the Great Basin, up to one third of known fault-controlled geothermal systems do not reach the surface and are considered “blind”, lacking geothermal surface expressions (Coolbaugh et al., 2006). Therefore, these blind systems must be found using subsurface data or inferred from surface features, such as siliceous sinter, travertine, and/or a preferred structural setting. Examples of developed blind geothermal systems include Desert Peak (Benoit et al., 1982; Faulds et al., 2010) and Blue Mountain (Faulds and Melosh, 2008).

Astor Pass is a blind, fault-controlled geothermal system within the Pyramid Lake Paiute Indian Reservation. It lies close to the California-Nevada border near the transition between the northern Walker Lane and the western Basin and Range province (Figure 1). The system was identified by Coolbaugh et al. (2006) in a reconnaissance of the Pyramid Lake region based on nearby argillic alteration of the Miocene rocks, the presence of linear belts of tufa towers, and promising results from a shallow temperature survey (Figure 2). The Astor Pass tufa is ~ 6 km northwest and along strike from a large modern geothermal outflow at Needle Rocks, a large tufa formation where boiling water emanates from springs and geothermal wells drilled in the 1960s, with peak water temperatures of 117°C. The Needle Rocks have significant cultural significance to the Pyramid Lake Paiute Tribe and are thus off limits to development. Other parts of the reservation have been reviewed for blind geothermal systems, which led to the discovery of the Astor Pass system. The initial structural investigation of Astor Pass suggested a dilational fault intersection in the vicinity of the tufa mounds as the main control on the geothermal system (Vice, 2008).

The goals of this study are to develop a comprehensive understanding of the structures at Astor Pass and related blind geothermal system by: 1) constructing a detailed three-dimensional (3D) geologic model, 2) identifying the structural elements conducive to fluid flow, and 3) continuing to develop the stratigraphic, kinematic, and dynamic framework of the area. To develop a 3D geologic model and elucidate the structural controls of the geothermal system, multiple datasets were interpreted and synthesized, including: 1) seismic reflection data, 2) well cuttings, 3) preexisting and new geologic mapping in the northern Virginia Mountains, 4) petrographic data, and 5) other available geophysical surveys, including magnetotelluric and gravity data. All of these data were then integrated to construct detailed cross sections and build a 3D structural model using EarthVision software (Dynamic Graphics, Inc.). In addition, borehole breakout data were used to define the regional stress field and, in turn, calculate slip and dilation tendency (Morris et al., 1996) on faults within the study area.

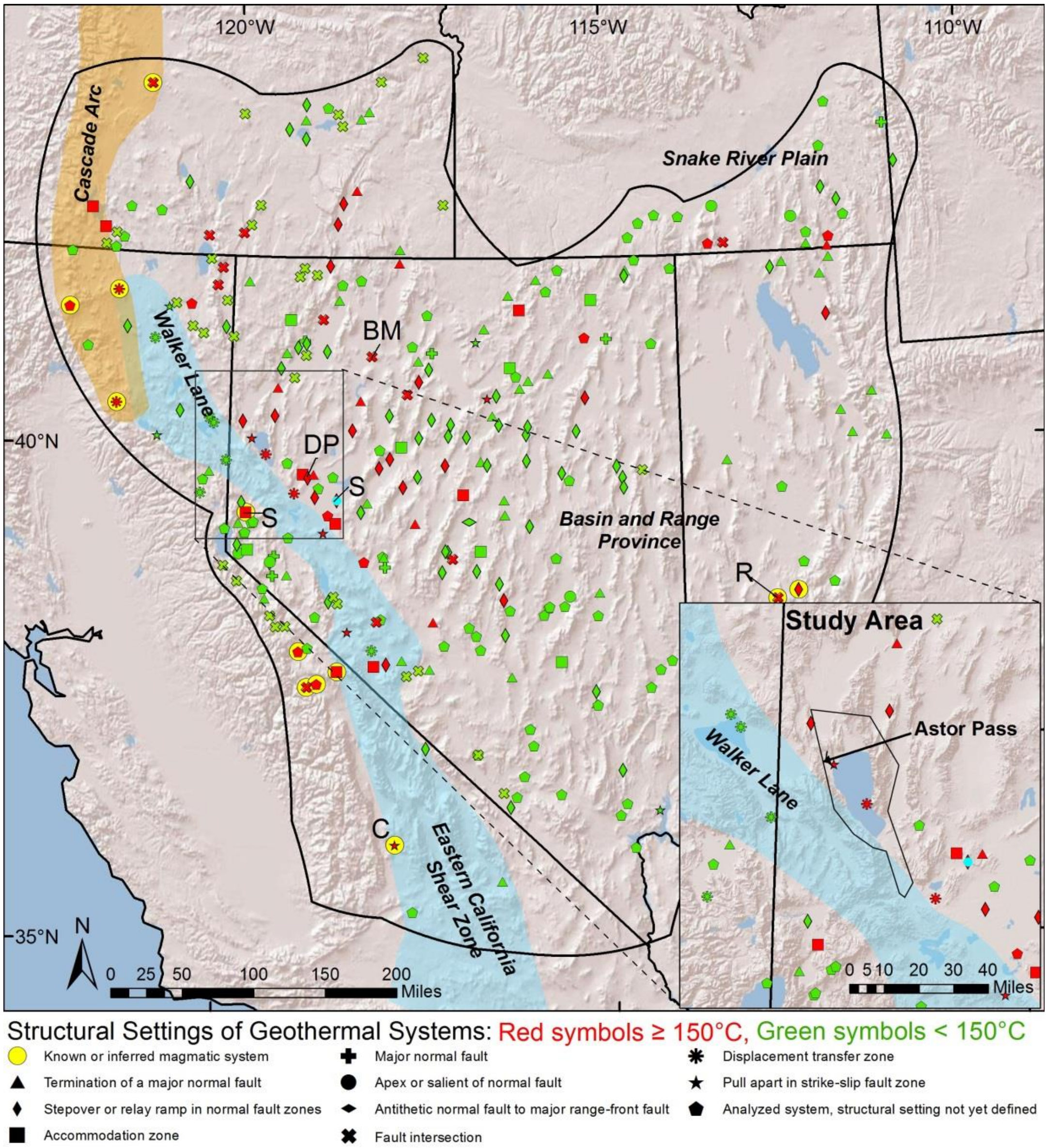

Figure 1. Geothermal systems in the Great Basin (modified from Faulds et al., 2011a) and the Astor Pass study area shown in the inset. Note the high concentration of "hot" systems (> 150°C) along the margin of the Walker Lane. Inset box shows location of systems and tectonic provinces in vicinity of Astor Pass and outline of Pyramid Lake Reservation. Locations of other notable geothermal systems are BM – Blue Mountain; C – Coso; DP – Desert Peak; R – Roosevelt; S – Stillwater; and SB – Steamboat.

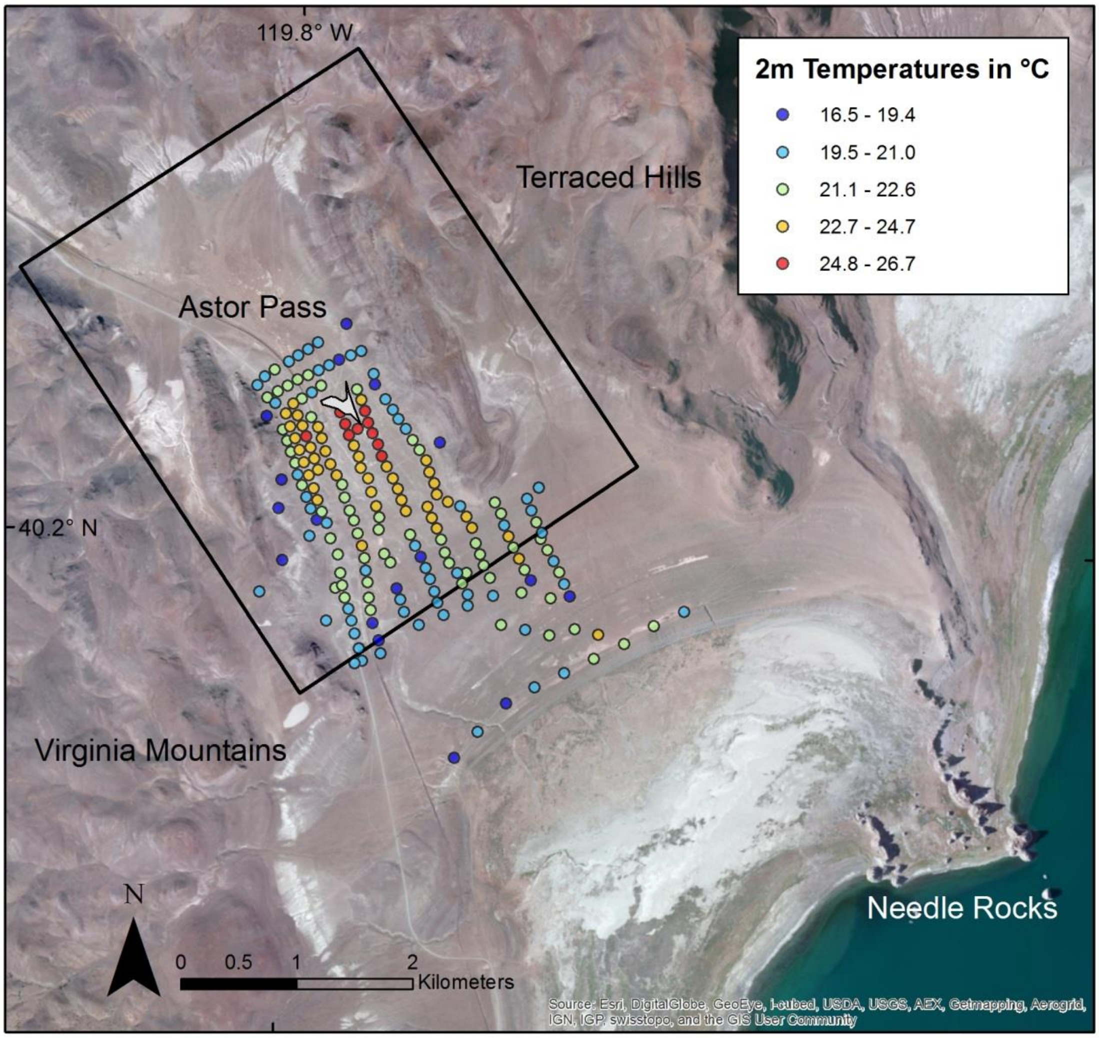

Figure 2. Aerial view of Astor Pass, Terraced Hills, and northern Virginia Mountains. Also shown are the 2 m temperature survey results (Kratt et al., 2010), with the hottest temperatures just south of the tufa mound (outlined in white). Black outline is the extent of the 3D model area.

Geologic Setting

Astor Pass is in northwestern Nevada within the transition between the western Basin and Range and the northern Walker Lane (Figure 1). The Walker Lane, along with the eastern California Shear Zone, is a system of dextral faults in the western Great Basin that accommodates ~20% of the Pacific-North American plate motion (Faulds and Henry, 2008; Kreemer et al., 2009). In comparison to the San Andreas dextral system, which accommodates the other 80% of plate motion with relatively continuous interconnected faults up to several hundred kilometers in length, the Walker Lane is characterized by relatively short, discontinuous, en echelon dextral faults (Stewart, 1988; Faulds et al., 2005a; Wesnousky, 2005; Faulds and Henry, 2008). Astor Pass lies in a group of geothermal systems defined as the “transitional Walker Lane” (Faulds et al., 2006). These geothermal systems reside in a transtensional structural setting of northwest-striking right-lateral faults and northerly striking normal faults.

The dextral faults of the northern Walker Lane and northerly striking normal faults are both simultaneously active based on seismological (Ichinose, 1998), kinematic (Faulds, 2005a), Quaternary fault (Briggs and Wesnousky, 2004, 2005), and geodetic data (Hammond and Thatcher, 2004; Hammond et al., 2011). Geodetic studies of the northern Walker Lane show dextral shear rates of ~1 cm/year (Thatcher, 2003; Briggs and Wesnousky, 2004; Hammond and Thatcher, 2004; Hammond et al., 2009). To the east, the relatively high shear Walker Lane gives way to lesser west-northwest-directed (~N55W) extension of 4.6 mm/yr relative to stable North America (Hammond et al., 2011).

Timing of Cenozoic deformation in the area is complex. Initial basin formation appears to coincide with the onset of east-northeast-directed extension at 12-13 Ma (Trexler et al., 2000; Henry et al., 2007). Normal faulting has continued episodically since ~13 Ma to the present as Basin and Range extension propagated westward. Dextral faulting within the northern Walker Lane initiated ~9 to 3 Ma (Cashman and Fontaine, 2000; Henry et al., 2007; Faulds et al., 2005b; Faulds and Henry, 2008; Hinz et al., 2009).

Onset of dextral movement in the northern Walker Lane is thought to be related to the northward migration of the Mendocino triple junction (Faulds et al., 2005a). The northern Walker Lane may be one of the youngest, least developed parts of the Pacific-North American plate boundary, as evidenced by relatively small cumulative dextral offset compared to other parts of the Walker Lane and eastern California shear zone (Faulds et al., 2005a).

The Astor Pass area exhibits structural elements of both the Walker Lane and Basin and Range province, with a west-northwest-striking dextral fault intersecting northerly striking normal and normal-dextral faults near a conspicuous tufa deposit. The pass itself is a narrow gap between the northern extent of the Virginia Mountains and the Terraced Hills (Figure 3). The southern part of Astor Pass (Figure 3), as it transitions to the shorelines of Pyramid Lake, is approximately on trend with a major dextral fault in the northern Walker Lane at the opposite end of Pyramid Lake, referred to as the Pyramid Lake fault zone (Figures 3 and 6).

Stratigraphic Framework

The Terraced Hills and northern Virginia Mountains are composed of Mesozoic metavolcanic and granitic rocks nonconformably overlain by a thick (~1 km) section of middle Miocene volcanic and sedimentary rocks (Figure 4) (Bonham and Papke, 1969; Drakos, 2007; Vice, 2008). The Miocene section is dominated by volcanic rocks of the middle Miocene Pyramid sequence, first described by Bonham and Papke (1969), which extensively covers the area surrounding Astor Pass and the Pyramid Lake region. The Pyramid sequence has been associated with ancestral Cascade arc volcanism that began

~22 Ma and abated by ~4 Ma in the region (Faulds and Henry, 2002; Faulds et al., 2005a). Arc volcanism terminated in the region as subduction ceased with the northwestward propagation of the San Andreas fault system and Walker Lane. Quaternary alluvium, spring, and lacustrine deposits onlap older units and dominate low-lying Astor Pass.

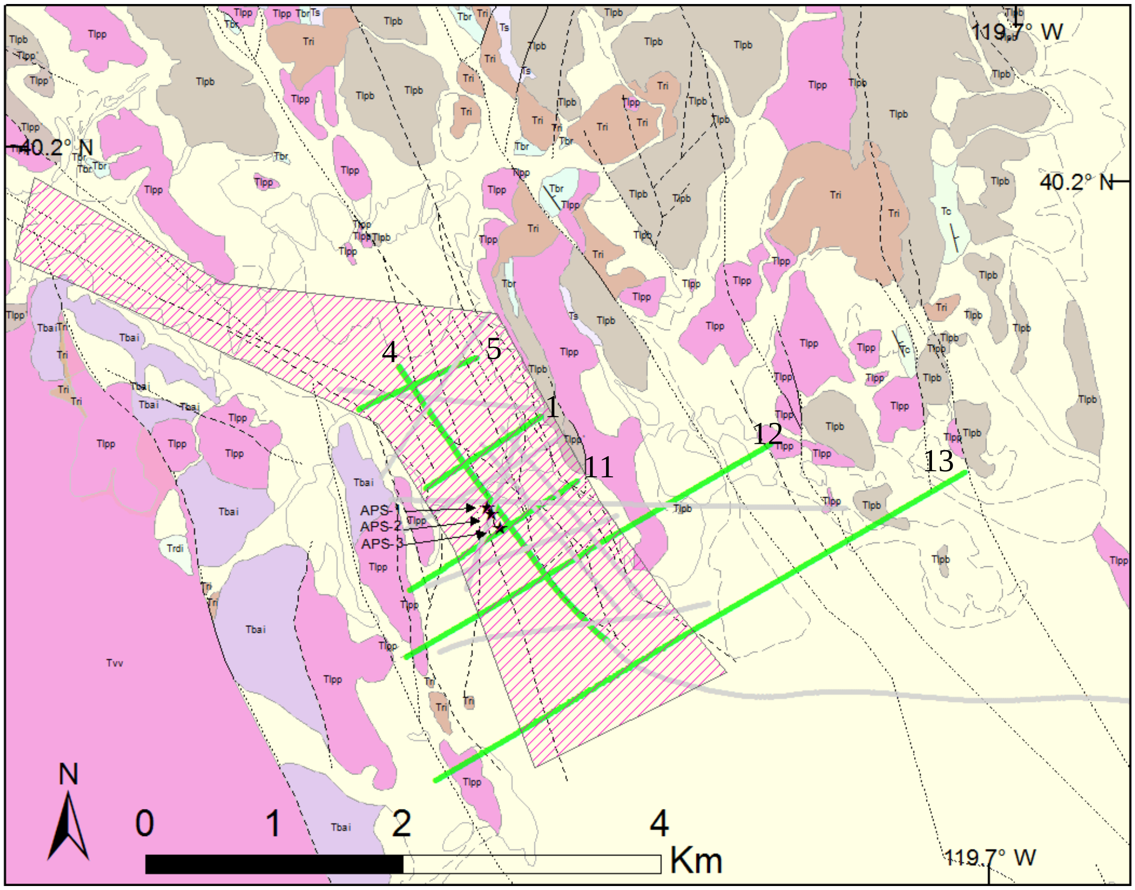

Figure 3. Simplified geologic map of the Astor Pass region. Brown, pink, purple, and gray units are Tertiary volcanic and sedimentary rocks. Yellow units are Quaternary alluvium, tufa, and other sediments. See Figure 4 stratigraphic column for explanation of unit abbreviations. Green lines show locations of seismic reflection profiles used in the 3D model. Line 11 also represents the cross section shown in Figure 6. Hatched area shows extent of Astor Pass. Stars in the middle of Astor Pass show locations of the APS wells (modified from Vice, 2008).

Mesozoic Basement

The Mesozoic basement is not exposed in the northern Virginia Mountains or Terraced Hills, but plutonic and metavolcanic rocks appear in the well cuttings at depths of ~1200 m in Astor Pass wells 2 and 3 (APS-2, APS-3). Although Mesozoic metasedimentary rocks, likely correlative with the Cottonwood Canyon formation (Kinsella, 2010), crop out extensively to the east in the Fox and Lake Ranges, these rocks do not appear in the well cuttings or outcrop in the Astor Pass area. Instead, basement cuttings from APS-2 and APS-3 consist of Mesozoic plutonic rocks and metavolcanic rocks. The metavolcanic rocks appear only in APS-3 as metamorphosed, porphyritic andesite lavas and are similar to exposures in the Dogskin Mountain Quadrangle, roughly 30 km to the south, other Jurassic metavolcanic rocks distributed across western Nevada (Henry et al., 2004). Above the metavolcanic rocks in APS-3 and the lowest unit in APS-2 is a plutonic granodiorite of likely Cretaceous age and similar to those mapped in the southern Virginia Mountains (Faulds et al., 2001), Dogskin

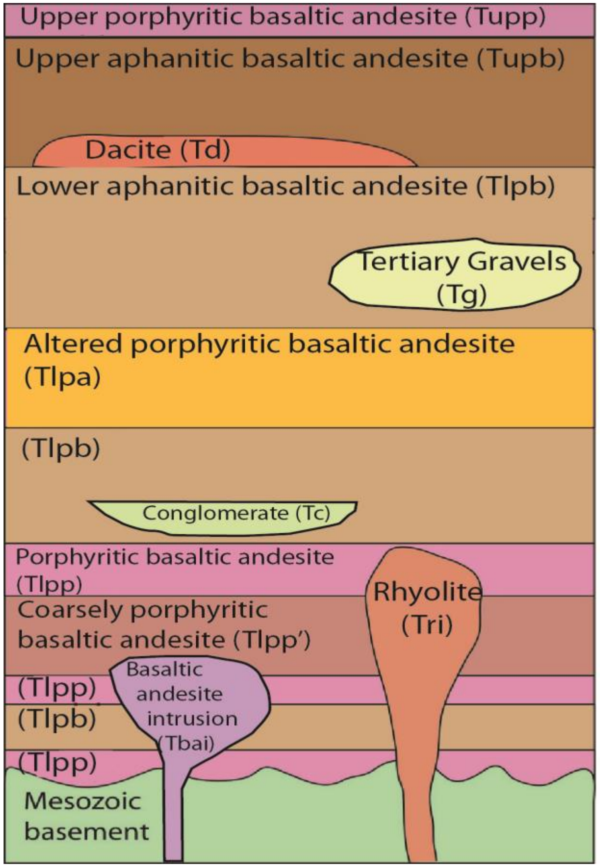

Figure 4. Simplified stratigraphic column of the Astor Pass area showing Tertiary volcanic and sedimentary units lying disconformably with Mesozoic basement. Not all units outcrop in the map shown in Figure 3. (modified from Vice, 2008).

Mountain (Henry et al., 2004) and in the Fox Range (Anderson, 2013). These plutons intruded the older Mesozoic metasedimentary and metavolcanic units. This Cretaceous monzodiorite to granodiorite is presumably associated with the Sierra Nevada Batholith and was likely emplaced between 90-105 Ma (Bonham and Papke, 1969; Drakos, 2007; Henry et al., 2007).

Tertiary

The ridges surrounding Astor Pass in the northern Virginia Mountains and Terraced Hills are largely composed of a thick section of middle Miocene volcanic rocks informally known as the Pyramid sequence (Bonham and Papke, 1969; Faulds et al., 2001; Faulds and Henry, 2002; Henry et al., 2004; Drakos, 2007; Vice, 2008).

This thick sequence (~1000 m) of intermediate to mafic volcanic rocks nonconformably overlies Mesozoic basement or rests disconformably on Oligocene-early Miocene ash-flow tuffs. Multiple Ar^{40}/Ar^{39} geochronology studies have yielded ages in the Pyramid sequence ranging from ~17.8-11.7 Ma (Ressel, 1996; Faulds et al., 2003; Drakos, 2007). In the Astor Pass area, the Pyramid sequence has yielded 40Ar/39Ar ages ranging from ~15.6 to 13.2 Ma (Vice, 2008). One local Pyramid sequence source is a remnant volcanic eruptive center in the northern Virginia Mountains (Faulds and Henry, 2002). In addition, several intrusions of basaltic andesite crop out directly west and southwest of Astor Pass (Vice, 2008).

Locally, the Pyramid sequence is broken into an upper and lower sequence, separated by the middle Miocene tuff of Mullen Pass (Vice, 2008). This tuff crops out stratigraphically up-section of Miocene rocks exposed at Astor Pass to the east in the Terraced Hills and does not appear in the drill cuttings or outcrop in the northern Virginia Mountains (Appendix B). Thus, the volcanic and volcaniclastic units found in Astor Pass appear to correlate with the lower Pyramid sequence. The lower part of the sequence is primarily composed of interfingering basalt and basaltic andesite flows, volcaniclastic rocks, and discontinuous rhyolitic domes and flows (Henry et al., 2004, 2007; Vice, 2008).

Cuttings from wells drilled at Astor Pass show that the Pyramid sequence is approximately 1100 m thick (Appendix B). The mafic lavas include a variety of textures, including aphanitic to finely porphyritic to more coarsely porphyritic with phenocrysts to 9 mm long. Some of the flows are intercalated with volcaniclastic rocks. The clastic deposits found in the Astor Pass cuttings are matrix supported, poorly to moderately sorted, light gray conglomerates, breccias, and sandstones. The clasts found in the sedimentary rocks were derived primarily from the Pyramid sequence volcanic rocks, with the sandstone and matrix in the conglomerates also consisting of feldspars and lithics sourced from the Pyramid sequence. These findings agree with previous descriptions of the Pyramid sequence volcanic and sedimentary units in the surrounding area (Faulds et al., 2003, 2007; Henry et al., 2004; Drakos, 2007; Vice, 2008).

Quaternary

Much of Astor Pass is overlain by Quaternary deposits, primarily lacustrine deposits, tufa deposits, and young alluvial fans (Vice, 2008). The tufa in Astor Pass is of particular importance. The tufa mounds that crop out on the floor of Astor Pass occur in linear trends, suggesting a fault-controlled origin and recent geothermal activity. These tufa mounds locally exceed 90 m in height as at the Needle Rocks (Figure 2) ~6 km to the southeast of Astor Pass (Coolbaugh et al., 2006).

Structural Framework

Astor Pass is on the eastern boundary of the northern Walker Lane, a 100 km wide, largely transtensional zone of discontinuous, left stepping, dextral faults (Faulds et al., 2005a; Faulds and Henry, 2008) accommodating ~20% of Pacific-North American plate motion (Hammond and Thatcher, 2004; Hammond et al., 2011). The relative immaturity of the northern Walker Lane is directly related to a lack of larger, through-going dextral faults. The discontinuous, en echelon left-stepping dextral faults are kinematically linked at each end with arrays of northerly to north-northeast-striking normal faults (Faulds et al., 2005b; Faulds and Henry, 2008; Figure 5).

The Pyramid Lake fault zone is the eastern boundary of the northern Walker Lane and accommodates 25-70% of the dextral motion in the northern Walker Lane (Briggs and Wesnousky, 2004). An offset Oligocene paleovalley indicates ~5-10 km of dextral slip along the Pyramid Lake fault zone, with cumulative displacement across the northern Walker Lane totaling ~25 km since ~9-3 Ma (Faulds et al., 2005b). As the Pyramid Lake fault terminates northwestward in the southern part of Pyramid Lake, dextral shear appears to be transferred to an array of west-dipping normal faults in the Lake Range and Nightingale Mountains (Drakos, 2007) and multiple discontinuous normal and dextral faults cutting the floor of Pyramid Lake (Eisses, 2012). Northerly striking faults in the Lake Range shows accommodated ~11-13 km of normal offset, which corresponds to ~6-

7 km of horizontal movement, well within the estimates of dextral offset on the Pyramid Lake fault (Faulds et al., 2005b; Drakos, 2007). This leaves 3-4 km of the dextral shear from the Pyramid Lake fault as unaccounted for in the southern part of the Pyramid Lake area. As described by Vice (2008), the Astor Pass area consists of a series of fault bounded, relatively low-relief, north-northwest-trending discontinuous fault blocks (Figures 3 and 6). The ridges generally follow the strike of the faults and are tilted to the east to northeast. Tilt magnitudes vary but generally do not exceed 45°. Attitudes within the lower part of the Miocene section appear to be similar to those in the upper part of the section. Based on limited kinematic data, morphology of Quaternary fault scarps, and offset of Miocene volcanic units, the faults probably accommodated normal and/or dextral-normal displacement. It is noteworthy that the Terraced Hills-Astor Pass area lies on trend with the Pyramid Lake fault zone, and thus some of the faults in the area may be related to the terminus of that fault.

Detailed studies in the northern Pyramid Lake area demonstrate the transtensional nature of the Astor Pass area. For example, trenching of a northerly striking fault in the eastern Terraced Hills showed little to no evidence of dextral movement but rather normal offset of ~2 m in the Quaternary (Vice, 2008). In contrast, dextral-oblique movement is evident on faults of a similar strike farther west in the Terraced Hills and Astor Pass.

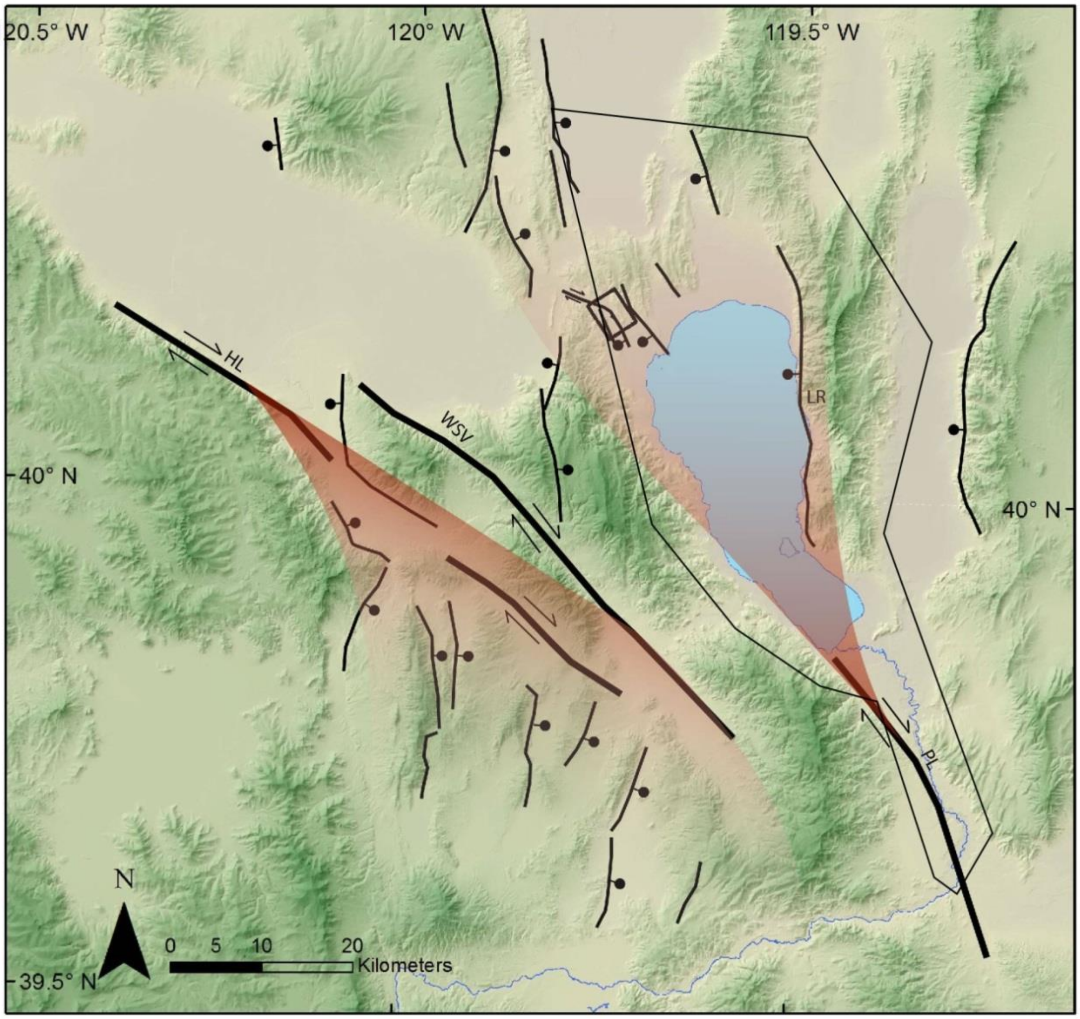

Figure 5. Digital elevation model of the northern Walker Lane. Dextral faults in this region are discontinuous and left-stepping. Near their terminations, dextral shear appears to be transferred to northerly striking normal fault systems. A dextral-oblique fault in the northwest part of Astor Pass strikes similarly to that of other Walker Lane dextral faults. Box is outline of Astor Pass 3D model area with polygon showing the border of the Pyramid Lake Paiute Tribe. Labeled faults: HL – Honey Lake; LR – Lake Range; PL – Pyramid Lake; WSV – Warm Springs Valley.

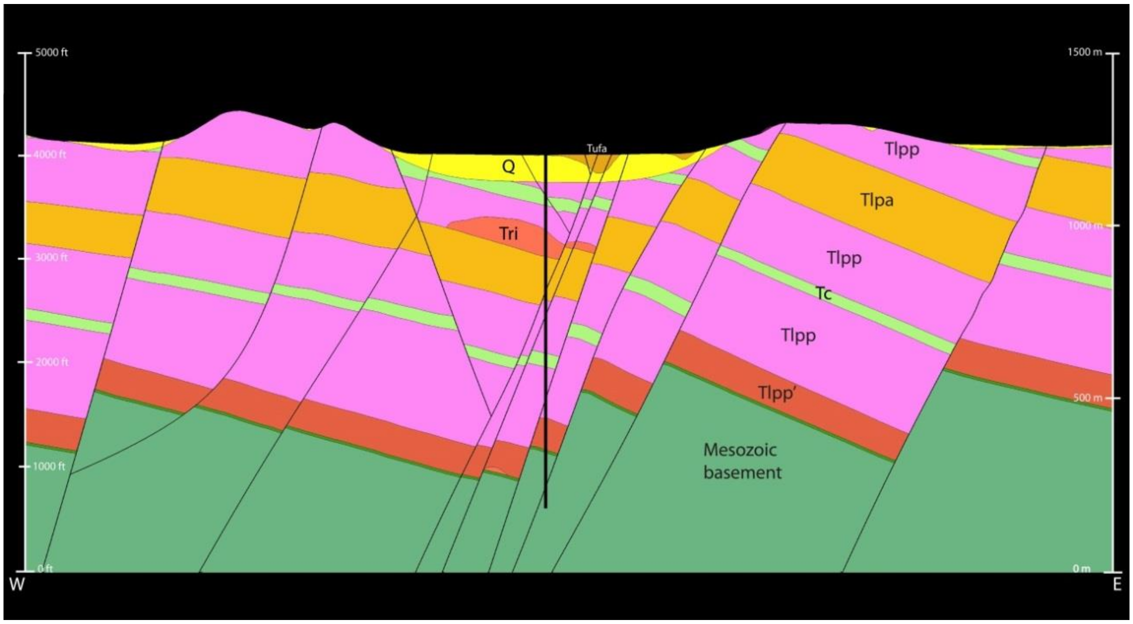

Figure 6. Representative cross section tracing seismic line 11 including intersecting APS #3, as shown in Figure 3. Units primarily consist of repeating Pyramid sequence volcanic and sedimentary rocks.

A north-northwest-striking fault directly east of Astor Pass accommodated ~600 m of dextral offset of a rhyolite intrusion as well as normal displacement of ~150 m. In addition, paleomagnetic data from the Terraced Hills indicate minor (~12°) clockwise vertical-axis rotation (Vice, 2008), which may accommodate minor amounts of dextral shear. Regional relations, the complex deformation expressed in sediments on the floor of Pyramid Lake (Eisses, 2012), both normal and dextral-normal faults in the Terraced Hills (Vice, 2008), and minor clockwise rotation (Vice, 2008) demonstrate that the Astor Pass area resides in a transtensional setting in which some dextral shear from the northward terminating Pyramid Lake fault is transferred northward to the Terraced Hills into arrays of normal and dextral-normal faults.

The transfer of dextral shear from the Pyramid Lake fault to normal fault systems appears to generate a region of enhanced extension in the Pyramid Lake area (Faulds et al., 2011b). Areas where strike-slip faults diffuse into normal fault systems have been referred to as displacement transfer zones (Faulds et al., 2011a, b). Enhanced dilation on normal faults in such a region favors deep circulation of meteoric fluids and thus increases the potential for geothermal activity. A critical question in such areas concerns the nature of the stress field as it transitions from strike-slip to extensional. This is important for understanding which fault orientations are more prone to dilation or slip and thus are more likely to channel fluids. Borehole breakout data from the APS-2 and APS-3 wells in Astor Pass were therefore analyzed to constrain the regional stress regime at Astor Pass, thereby fostering slip and dilation tendency analysis on the myriad of local faults.

Geothermal System

The basis of the 3D model and study of the Astor Pass geothermal system started with a detailed geologic investigation of the area by Vice (2008). His work at Astor Pass and the Terraced Hills revealed further evidence of a geothermal system at depth and targeted a presumed dilatant quadrant of a fault intersection for geothermal exploitation. A very steeply dipping, WNW-striking dextral-normal fault appears to intersect and terminate into a northwest-striking, west-dipping normal-dextral fault in the vicinity of tufa towers on the floor of Astor Pass. Mapped stratigraphic units are mildly to moderately east-tilted (30- 45°) and cut by north-northwest-striking faults in the Terraced Hills. His conclusions relied heavily on surface data, including detailed geologic mapping of the Terraced Hills and surrounding area, tufa lineations that presumably corresponded with fault traces, trenching, and supplemental gravity data. Gravity data, offset stratigraphy, and limited fault kinematic data confirmed fault dips and slip directions. The targeted dilatant fault intersection corresponded with an intersection of two linear trends of tufa towers in Astor Pass on trend with mapped nearby faults. The 2 m temperature survey (Coolbaugh et al., 2006), showed anomalously high temperatures in the southwestern, presumably dilatant quadrant of this fault intersection (Figure 2). This led to drilling exploration in this area, which showed water temperatures of ~90°C at ~200 m in a 550 m deep well (APS-1).

Additional geologic data has been collected since Vice (2008) as part of the continuing investigation of the geothermal potential at Astor Pass. The new geologic data is derived from the drilling of exploration/production wells APS-2 and APS-3. These wells were drilled to depths of 1315 m (APS-2) and 1378 m (APS-3), giving stratigraphic control to basement rocks in the center of the geothermal field. This also confirmed the local thickness of the Pyramid sequence. These boreholes were imaged for borehole breakout analysis, allowing stress directions and magnitudes to be calculated.

Though Astor Pass has no active geothermal expression, the tufa mounds may represent past geothermal activity. Water measured during drilling and well tests of APS-2 and APS-3 has peak temperatures of 95°C. The temperature profiles in both wells show a quickly increasing curve to ~90-93°C followed by a nearly isothermal path to the final depth of the wells. Geothermometer temperatures of 130-143°C have been recorded at Astor Pass, showing the possibility of higher fluid temperatures nearby (Coolbaugh et al., 2006; Vice, 2008). The closest active geothermal surface expression to Astor Pass is 6 km to the southeast at the Needle Rocks, which has large tufa towers, subsurface well temperatures of 117°C, and geothermometer temperatures ranging from 143°C to 213°C (Coolbaugh et al., 2006). The Needles Rocks will not be developed because of the cultural value to the Pyramid Lake Paiute Reservation.

Geologic Data

Borehole Imaging

Borehole imaging was conducted in the lower intervals of wells APS-2 and APS-3. Acoustic and resistivity imaging was collected from 991-1313 m in APS-2 and 655-1376 m in APS-3 by Baker Hughes (Figure 7). This high-resolution acoustic and resistivity image allows fault and fracture analysis of the wellbore. Wellbore breakouts manifest themselves on the wellbore image as dark bands of low reflection amplitudes or out-of-focus patches on the electrical imaging log (Zoback et al., 2003). Breakouts will normally form symmetrically on both sides of the borehole wall, where the stress concentration exceeds the strength of the rock (Figure 8). Although symmetrical, breakouts are measured independently for azimuth and width (Barton et al., 1988). The width of the breakout corresponds with the difference between the strength of the rock and the compressive stress at the wellbore, and its azimuth corresponds with the least principal horizontal stress (S_{hmin}) (Barton et al., 1988; Zoback et al., 1985; 2003).

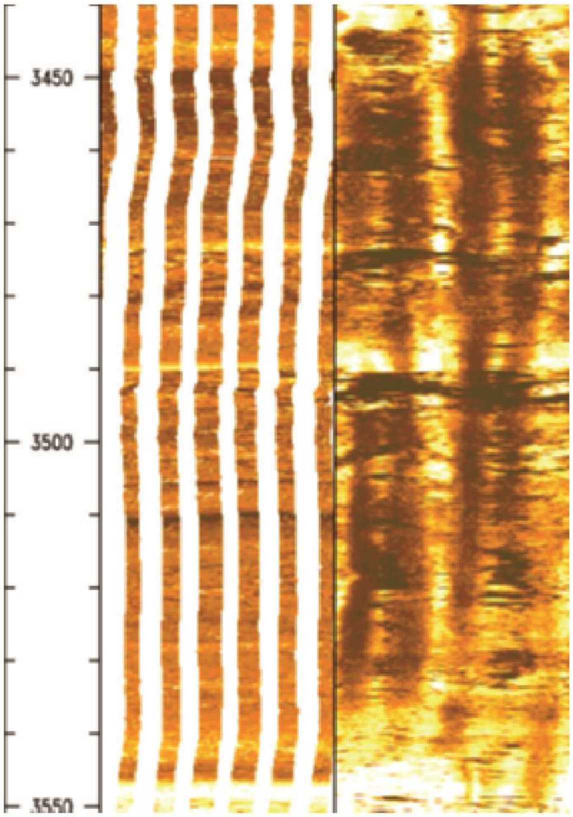

Depth	Azimuth	Type	Width (deg)
3450	273	BREAKOUT	27
3451	269	BREAKOUT	35
3453	266	BREAKOUT	30
3454	269	BREAKOUT	32
3457	87	BREAKOUT	35
3459	284	BREAKOUT	32
3460	265	BREAKOUT	40
3466	116	BREAKOUT	60
3469	296	BREAKOUT	48
3479	290	BREAKOUT	40
3480	109	BREAKOUT	29
3481	98	BREAKOUT	28
3484	94	BREAKOUT	45
3497	102	BREAKOUT	42
3503	112	BREAKOUT	34
3505	265	BREAKOUT	40
3516	268	BREAKOUT	47
3517	282	BREAKOUT	40
3518	276	BREAKOUT	45
3519	261	BREAKOUT	54
3520	290	BREAKOUT	25
3530	275	BREAKOUT	53
3532	264	BREAKOUT	33
3542	272	BREAKOUT	29

Figure 7. Image log from APS-3. Dark bands mark breakouts in the unwrapped image showing 0-360 degrees from left to right. Corresponding breakouts and drilling-induced tensile fractures measured by McNamara (written communication, 2013) with depth, type, azimuth, and breakout width for this image section.

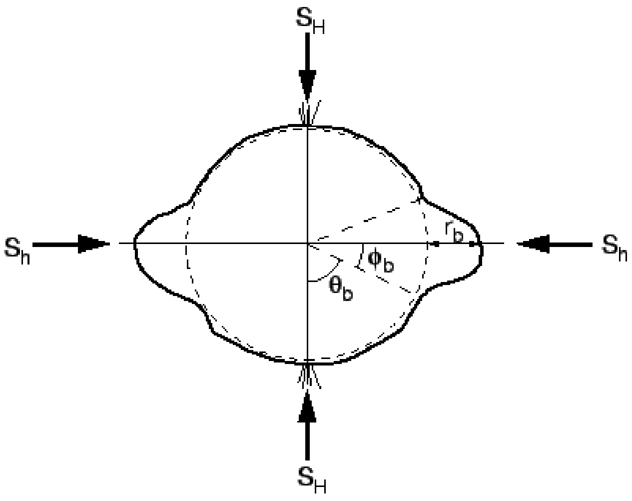

Figure 8. Schematic of borehole breakout showing S_{hmin} (S_h) and S_{Hmax} (S_H) relative to breakout. R_b is breakout depth while φ_b and θ_b correspond to breakout opening half-angle and breakout orientation angle. Also note the tensile fractures at the same azimuth as S_{Hmax}.

Breakout width is also useful in estimating the maximum horizontal stress, where combined with unconfined compressive rock strength and S_{hmin} values (Barton et al., 1988). In addition, drilling-induced tensile fractures can appear in the wellbore at similar azimuths to S_{Hmax}, 90° from the breakouts. These tensile fractures form only if the two horizontal stresses are significantly different, indicating the wellbore failed in both compression and tension where accompanied by breakouts.

Stress Field Analysis

A common method of gathering stress data in the field is from fault plane and kinematic analysis. This provides insight into the regional stress field condition but is dependent upon outcrop quality along with general assumptions of how the shear stress interacts with the fault plane (Angelier, 1984; Marrett and Allmendinger, 1990). Because of the low number of exposed fault planes with kinematic indicators found in the Astor Pass area, using this method to calculate the regional stress field is unreliable. Therefore, the stress field was estimated from borehole breakout data.

Calculation of In Situ Stresses at Depth

Stress calculations at depth from drill holes can also provide accurate insight into the regional stress field. Drilling boreholes allows relatively straightforward measurements of the in situ stress field at depth, producing practical data that can address a wide range of structural and geomechanical problems. Although stress as a tensor describes forces acting on all surfaces passing through a given point, these tensors are simplified and combined from a 9 component system into a principal 3 component system (Zoback et al., 2007). Principal stress orientations (σ_1, σ_2 and σ_3) and the stress ratio were calculated using borehole cuttings for density calculations and imaging data. With the assumption that the strength of the crust at depth constrains the difference in maximum stress magnitudes, there is a limit to the ratio of maximum principal effective stress and the minimum principal effective stress (Jaeger and Cook, 1979; Zoback et al., 2003). We use the Andersonian theory of faulting (Anderson, 1951) to determine which principal stress (S_v = vertical stress, S_{hmin} = minimum horizontal stress, and S_{hmax} = maximum horizontal stress) correspond to σ_1, σ_2 and σ_3, and to establish the range of stress values. For normal faulting,

$$\frac{\sigma_1}{\sigma_3} = \frac{S_v - P_p}{S_{hmin} - P_p} \leq \left[(\mu^2 + 1)^{\frac{1}{2}} + \mu\right]^2, \tag{1}$$

and strike-slip faulting,

$$\frac{\sigma_1}{\sigma_3} = \frac{S_{Hmax} - P_p}{S_{hmin} - P_p} \leq \left[(\mu^2 + 1)^{\frac{1}{2}} + \mu\right]^2, \tag{2}$$

with P_p being the pore pressure and μ the coefficient of friction (Zoback et al., 2003). This allows an estimation of the limiting principal effective stress differences using a standard value for μ and hydrostatic pressure for P_p. In the case of the transtensional regime at Astor Pass, σ_1 is typically S_{Hmax} (Eqn. (2), whereas σ_2 and σ_3 correspond with S_v and S_{hmin} (Equation 1).

The vertical stress is calculated by integrating the density of the overburden,

$$S_V = \int_0^z \rho(z) g dz \approx \bar{p}\, gz\ , \tag{3}$$

with $\rho(z)$ representing the density function, g the gravitational constant, and $\bar{p}$ the average overburden density (Zoback et al., 2003). With accurate borehole logs and rock densities, S_v can be calculated for APS-2 and APS-3 (Figure 9). The vertical stress increases with depth, with values increasing to 35.1 MPa at 1524 m in APS-3, with similar values calculated in APS-2.

With knowledge of the vertical stress at Astor Pass, we can determine the orientation and magnitudes of S_{Hmax} and S_{hmin} in APS-2 and APS-3, assuming a normal faulting environment. The minimum horizontal stress magnitude is calculated by solving Equation (1) for S_{hmin} using a coefficient of friction value between 0.6 and 1.0, typical for rocks at depths of 1-5 km (Figure 9) (Zoback et al., 2003). Hydrostatic pressure was used in place of the measured pore pressure during drilling to simiplify the equation. The orientation of S_{hmin} is estimated from the averaged azimuths of borehole breakouts viewed from the borehole image logs (Figure 10). Minimum horizontal stress values were 10.8 MPa at 760 m and 22 MPa at 1524 m in APS-3.

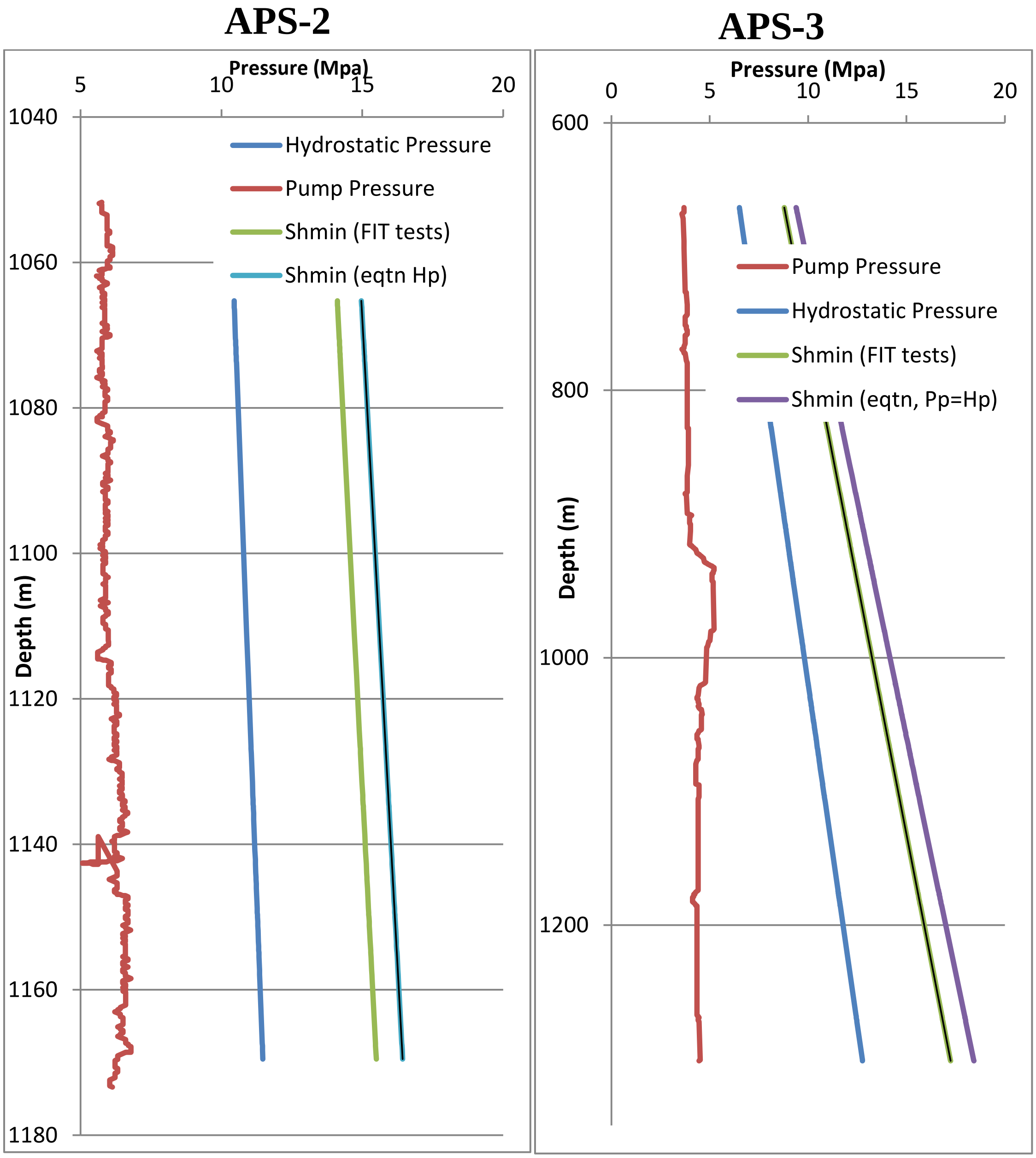

APS-2

APS-3

Figure 9. Shmin and Pore Pressure measurements and calculations for APS-2 and APS-3. Hp = Hydrostatic Pressure, Pp = Pore Pressure, FIT = Formation Integrity Test. Calculations by McNamara (written communication, 2013).

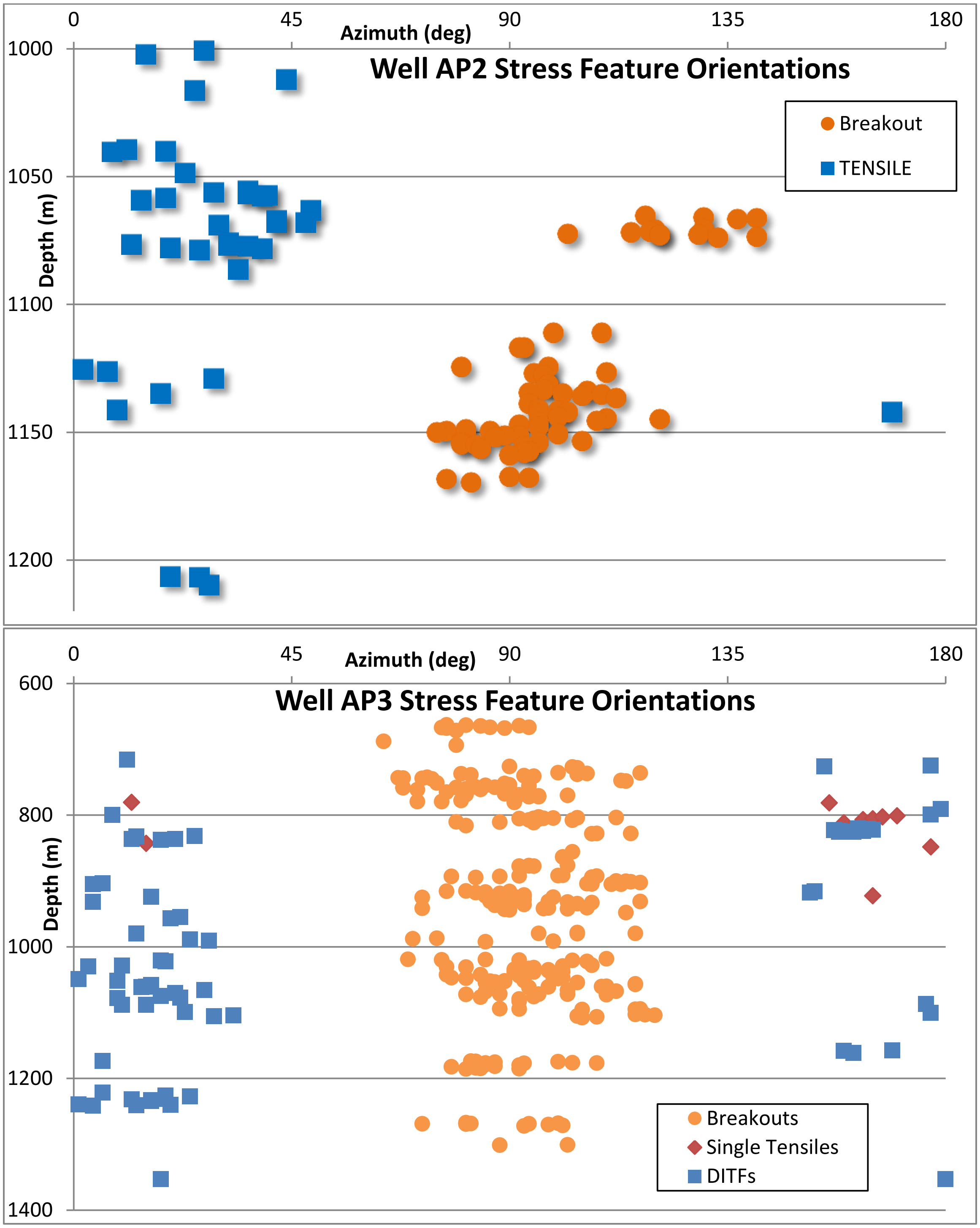

Figure 10. Borehole breakouts, single tensile fractures and drilling-induced tensile fractures used in stress calculations for APS-2 and APS-3. Calculations by McNamara (written communication, 2013).

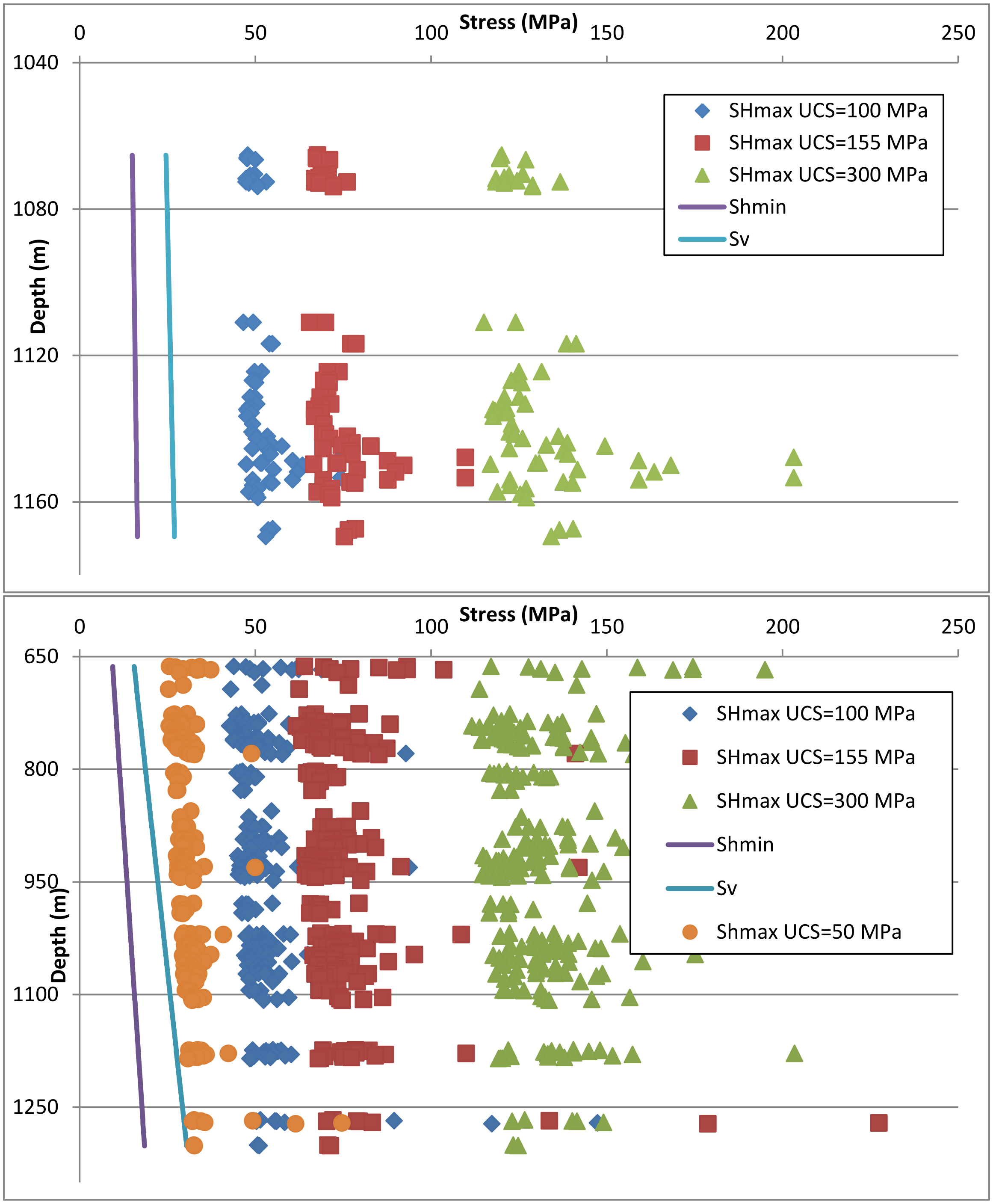

Figure 11. Maximum horizontal stress values from borehole breakout measurements in APS-2 and APS-3. Shmax values calculated using multiple UCS numbers because actual rock strength is unknown. UCS - Unconfined compressional rock strength. Calculations by McNamara (written communication, 2013).

Deriving S_{Hmax} is more difficult to estimate, because it relies on three variables, unconfined compressive rock strength (C_o), S_{hmin}, and breakout width (Barton et al., 1988; Zoback et al., 2003). It is worth noting that the fracture depth of the breakout (R_b in Figure 7) can increase after initial borehole failure, but these breakouts do not widen over time from stress (Zoback et al., 1985; Barton et al., 1988). Because the initial breakout angle does not change over time, Barton et al. (1988) developed a methodology of relating the breakout angle to circumferential stress, which is also equal to the unconfined compressive rock strength. This allows use of breakout width to estimate S_{Hmax} by setting the compressive rock strength equal to the circumferential stress in Equation (4), then converting to principal stresses and solving for S_{Hmax} in Equation (6),

$$\sigma_\theta = (\sigma_1 + \sigma_3) - 2(\sigma_1 - \sigma_3)Cos2\theta - \Delta P_W, \tag{4}$$

$$C_0 = \sigma_\theta = (\sigma_1 + \sigma_3) - 2(\sigma_1 - \sigma_3)Cos2\theta - \Delta P_W, \tag{5}$$

$$S_{Hmax} = \frac{(C_0 + 2P_p + \Delta P + \sigma^{\Delta T}) - S_{hmin}(1 + 2cos2\theta_b)}{1 - 2cos2\theta_b}, \tag{6}$$

where $2\theta_b = \pi - w_{bo}$, w_{bo} being breakout width. This method provides S_{Hmax} results but is highly dependent on an accurate unconfined compressive rock strength for a given breakout width (Figure 10) (Barton et al., 1988; Zoback et al., 2003; Zoback, 2007). Because the exact rock strength of the basalts and basaltic andesites is not known, multiple values were used between standardized values for the rock type in the western US.

Results using a range of rock strength values show a strong strike-slip component, with S_{Hmax} consistently larger than S_v. Average values of S_{Hmax} orientations in APS-2 are 26 NE, but a strong bi-modal nature exists with orientations above 1100 m showing a 30

NE azimuth, but below 1100 m the S_{Hmax} direction changes to a more northerly 14 NE trend. Standard deviations for these measurements are 12 and 14, above and below 1100 m, respectively. S_{Hmax} orientations in APS-3 do not show a bi-modal nature, and data from 660 to 1300 m show a fairly consistent average azimuth of 4 NE with a standard deviation of 16. S_{Hmax} magnitudes vary considerably by the rock strength used in the calculation. Stress magnitudes used for slip and dilation tendency followed a profile similar to the unconfined rock strength curve of 100 MPa, with a maximum S_{Hmax} at 1524 m of 66.5 MPa.

One problem with using Equation (6) to derive S_{Hmax}, using borehole breakout data from APS-2 and APS-3, is the assumption that σ_1 is vertical, which the data in Figure (11) clearly disputes. Equation (6) relies on a value of S_{hmin} to complete the calculation. With the data available at Astor Pass, the only way to solve for S_{hmin} is using Equation (1) using the known, calculated value of S_v. Using Equation (2) for a strike-slip regime is precluded due to two unknown variables. To use the correct equations to calculate S_{hmin} and S_{Hmax} would require additional well data, such as a leak-off test. These results in calculated stress values, though close to actual values, may not be completely accurate for S_{hmin} and S_v.

Geophysical Data

Seismic Reflection

The seismic reflection data collected at Astor Pass were used to pick faults and stratigraphy, extending to depth the overall data resolution of the surface geologic mapping in the area. Data were first collected in 2006 by ZAPATA-Blackhawk using a small seismic vibrator source called a minivibe with short offset receivers, producing five lines of data with a fairly shallow depth of usable resolution (Louie et al., 2011). In May 2010,Optim Inc. recollected the 4th line of this dataset along with an additional 11 lines of 2d seismic-reflection-refraction using three heavy (60,000 lb.) vibrator sources with over 200 channels recorded simultaneously. All 16 of the 2d lines were then processed or reprocessed by Optim Inc. using advanced seismic analysis, including first-arrival velocity optimization and pre-stack depth migration (Louie et al., 2011). This allowed for usable data resolution to depths of ~1500 m on some lines with velocity control to 900 m. The seismic reflection data collected in 2010 were shot with long offsets, optimized to image steeply dipping structures at the lower predicted reservoir depths. The majority of these additional lines were shot perpendicular to the predominately north- to northwest-striking faults in Astor Pass, along an east-northeast trend, to maximize viewing angle (Figure 3).

Interpretation of the processed data concentrated on identifying faults hidden beneath the Quaternary deposits in Astor Pass and not exposed in outcrop or evident due to stratigraphic repetition (Appendix A). Special attention was paid to identifying trends of offset (A), terminating (B), and dipping (C) seismic reflectors analogous to faulted or offset stratigraphy (Figure 12). The majority of interpreted faults corresponded well with known, concealed, or inferred faults found in the detailed surface mapping, with the seismic constraining the fault strike and dip in the basin sediments. Only smaller fault segments and faults completely concealed by Quaternary sediments were found exclusively in the seismic reflection data.

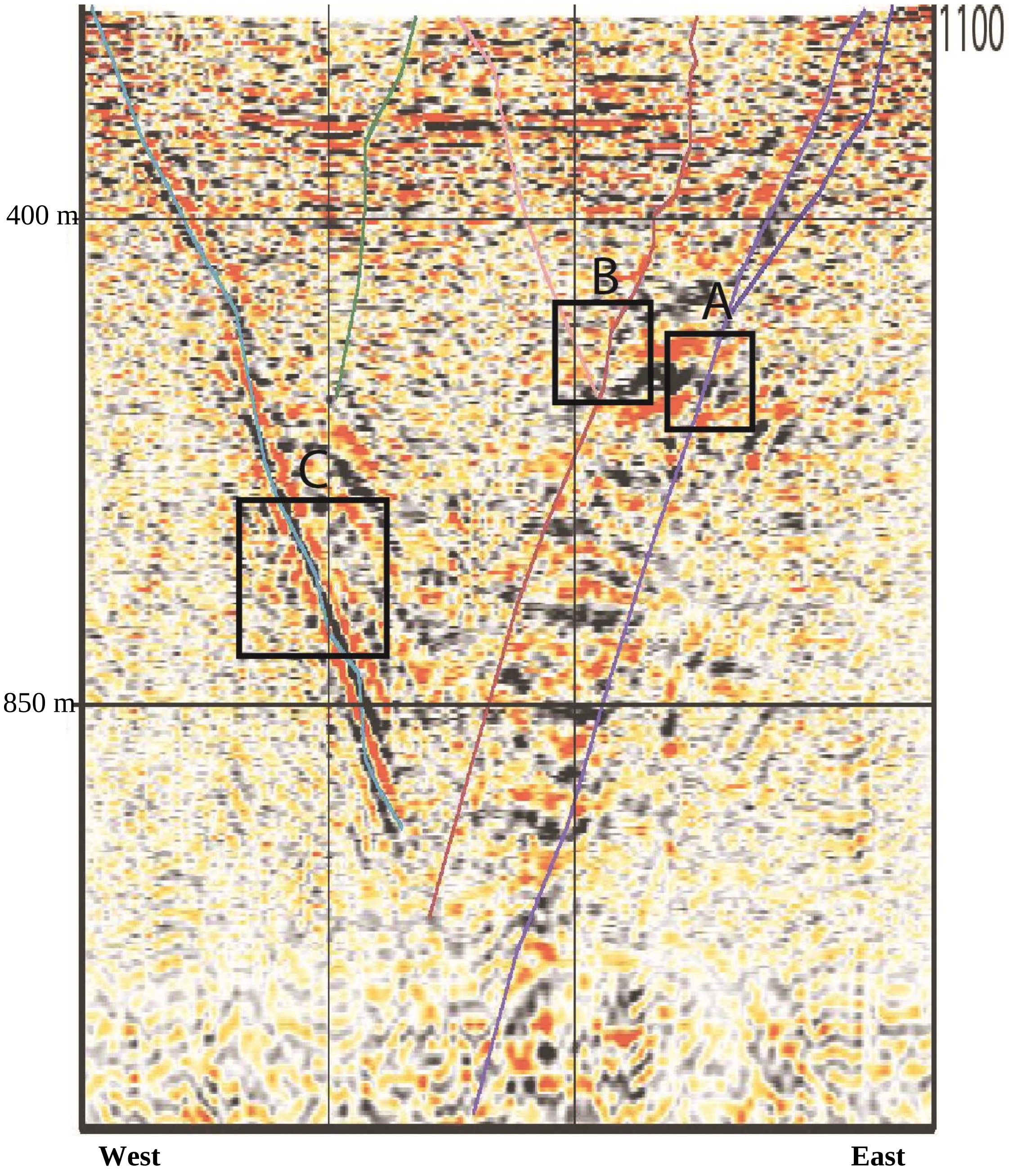

Figure 12. Example seismic reflection interpretation taken from seismic line 1 (Figure 3). Boxes outline various interpretative methods for faults. Box A shows offset reflectors, Box B abrupt reflector termination, and Box C steeply dipping fault-plane reflectors. Seismic line is ~1.5 km in length.

The velocity model of each 2D line was also examined and compared to the reflection profile to further assess and constrain fault picks (Figure 13). Due to the high impedance and complex, high reflection amplitudes in thevolcanic rocks combined with poor well control (only 2 lines spatially intersected boreholes), distinguishing volcanic stratigraphy proved difficult (as for Zuo and Fan, 2011). The thick section of Miocene volcanic rocks (~1200 m) and the limited depth resolution of the seismic reflection data (<1000 m) precluded imaging of the basement contact in any seismic lines. In contrast, the Quaternary/Tertiary boundary was picked for each line on the basis of prominent reflectors and where possible by well cuttings. These picks were incorporated into the 3D model.

Magnetotelluric Survey

A magnetotelluric survey of Astor pass was conducted in March 2010 by Zonge Geosciences, Incorporated. Five magnetotelluric data lines were acquired, with line locations corresponding with existing seismic reflection lines (Figure 14). Lines were collected using 100 m spacing of electric-field receiver dipoles. Magnetotelluric measurements were made over a frequency range of 0.0015 – 8192 Hz. Data quality was deemed generally acceptable, with relatively low cultural interference. Zonge performed a smooth model Cagniard resistivity and impedance phase data inversion using a SCS2D proprietary algorithm. Analysis of the 5 lines of magnetotelluric data show promise in constraining the geothermal anomaly. Line 4 suggests a deep zone beneath the tufa towers of low resistivity, which may correlate with geothermal fluids (Figure 15). Lower resistivity zones found in other geothermal areas, such as Coso and Beowawe, have been correlated with areas of conductive geothermal fluids (Garg et al., 2007; Newman et al., 2008).

However, tensor evaluation of this anomaly could be suspect in Line 4 because it subparallels major faults that may control fluid flow. Also, modeled structures using this 2D resistivity can only be inverted to depths of approximately 2/3 the line length. Although a low resistivity anomaly under the tufa tower could exist, the lower bound and shape of such an anomaly is unconstrained because of lack of data resolution. The upper dome shape of the anomaly is constrained with measured data.

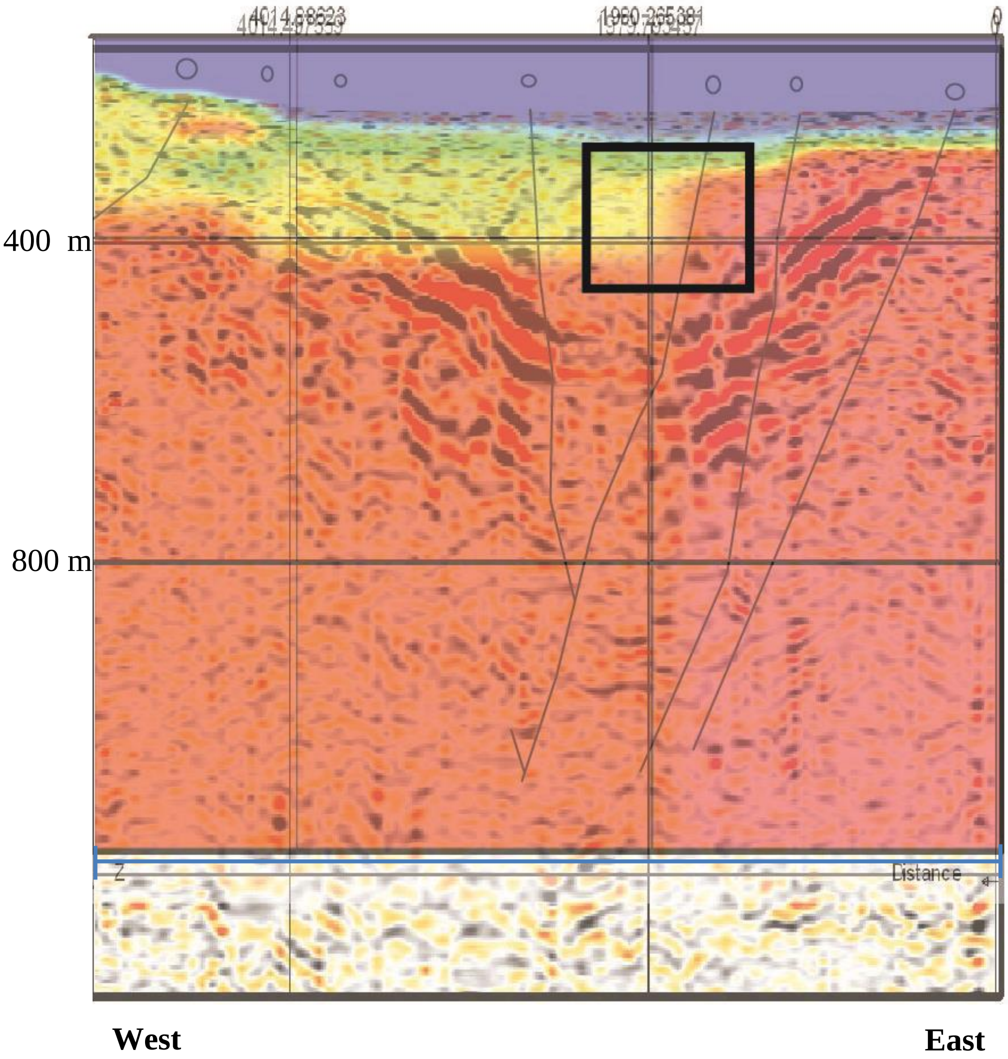

Figure 13. Seismic line 11 (Figure 3) showing Optim's SeisOpt® optimized velocity field of the section. Box outlines the abrupt lateral velocity change that indicates a fault.

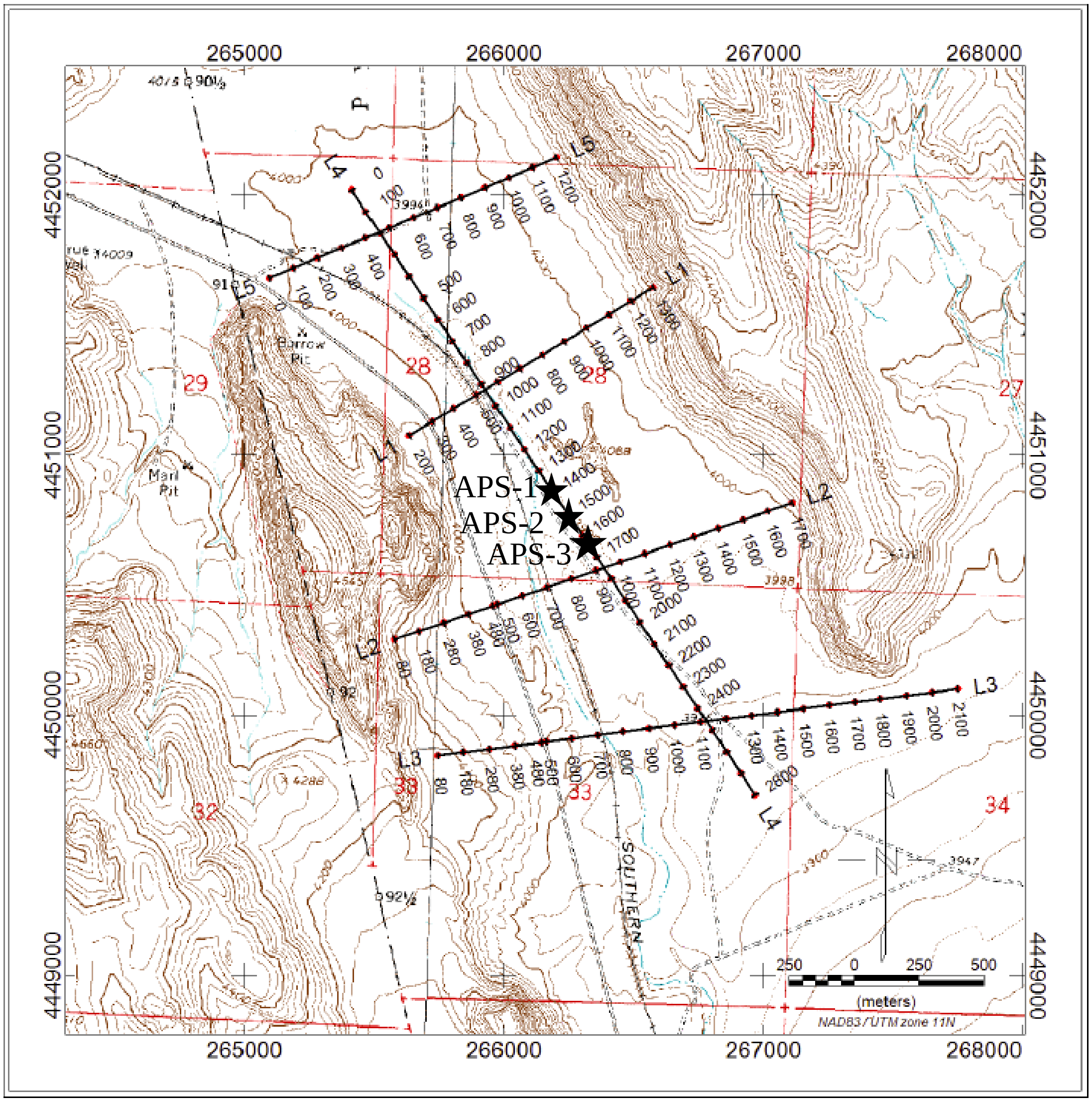

Figure 14. Location of magnetotelluric lines and approximate well locations of APS-1, APS-2, and APS-3.

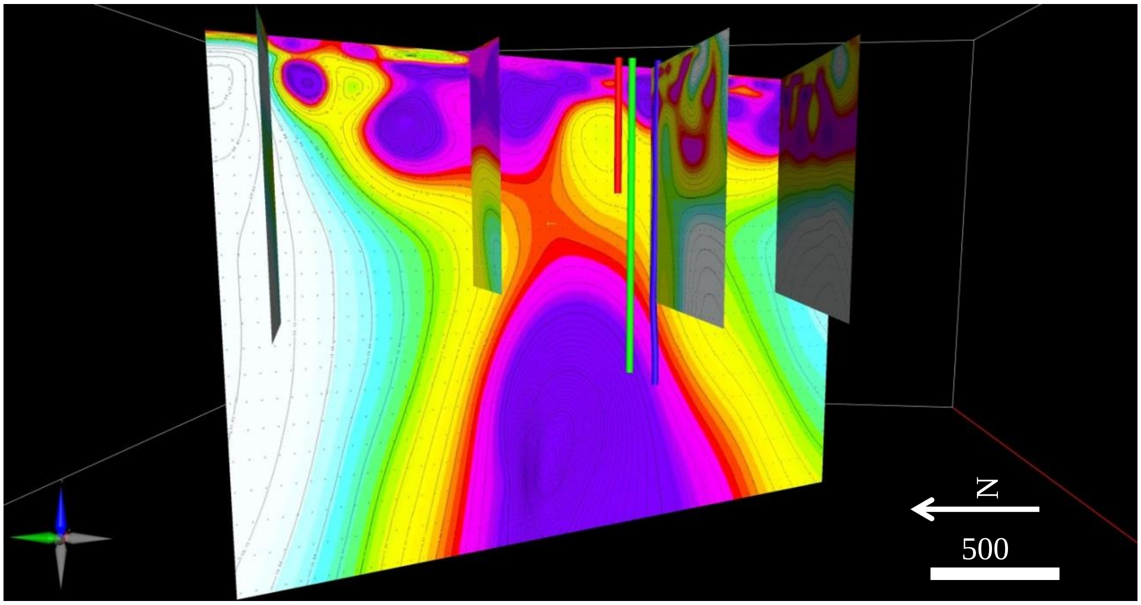

Figure 15. Line 4 of 2D Inversion of magnetotelluric data. View is looking due east. Warmer colors equate with lower resistivity. Red, green, and blue well paths represent APS-1,-2, and -3 respectively. Shape of lower portion of the low resistivity anomaly is unconstrained, but upper anomaly should accurately model resistivity.

3D Model

Model Construction

Three-dimensional modeling allows viewing of multiple, integrated, data sources, ideally allowing a greater understanding of the structural characteristics of a geologic area. The Astor Pass 3D structural geologic model was constructed using Dynamic Graphics EarthVision software from detailed cross-sections, surface geologic mapping, and borehole data. The interpreted seismic reflection data were integrated into the cross-sections (Figure 16). Magnetotelluric data were not used in the 3D model construction but were valuable in picking drilling targets and forming hypotheses of the geothermal system.

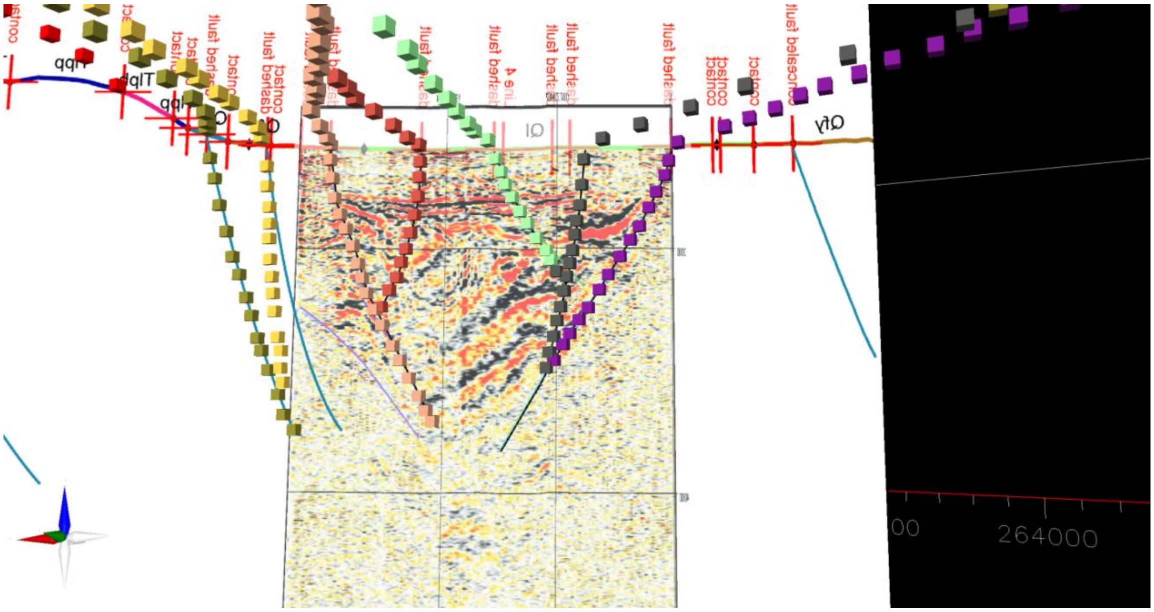

Figure 16. Digitizing seismic reflection cross sections for fault data. Each color of digitized points represents a separate fault segment. Points digitized from surface map of fault traces are also shown.

The surface of the 3D model was generated by overlaying the 1:24000 scale geologic map (Vice, 2008) on a 10 m Digital Elevation Map (DEM). This surface contains detailed geologic mapping, fault traces from the seismic interpretation, and geographic markers for the tips of the cross-section lines (Figure 17). The map and DEM were then clipped to a predetermined model area of approximately 10 km^2. To input the surface data into the model, faults and stratigraphic units were separated into individual fault strands and units. Each individual unit or fault strand was then manually digitized (Figure 16, 18). Fault and horizon data files were then expanded with the addition of subsurface data. Subsurface data used in the 3D model construction consisted of cross-sections and well data. Cross sections were exported from ArcGIS using the surface traces of 6 of the 2D seismic reflection profiles (Figure 3), which were contained within the 3D model volume (Figure 3).

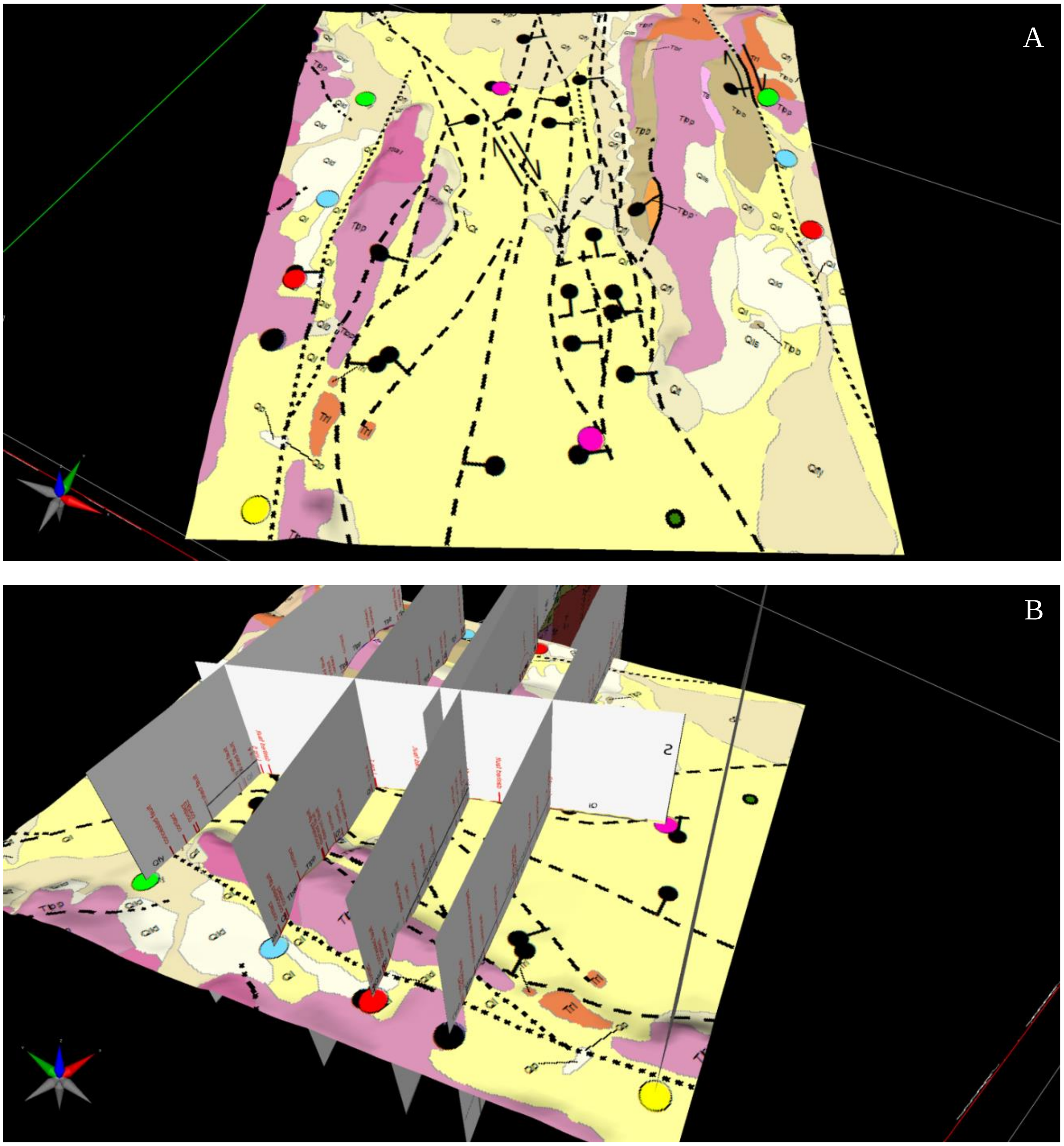

Figure 17. A. Surface map trimmed to model area. Colored dots mark the endpoints of the 6 cross-sections used in the model, shown in B. Each fault trace and contact were digitized and input into the model. Model surface is 3 km by 4km.

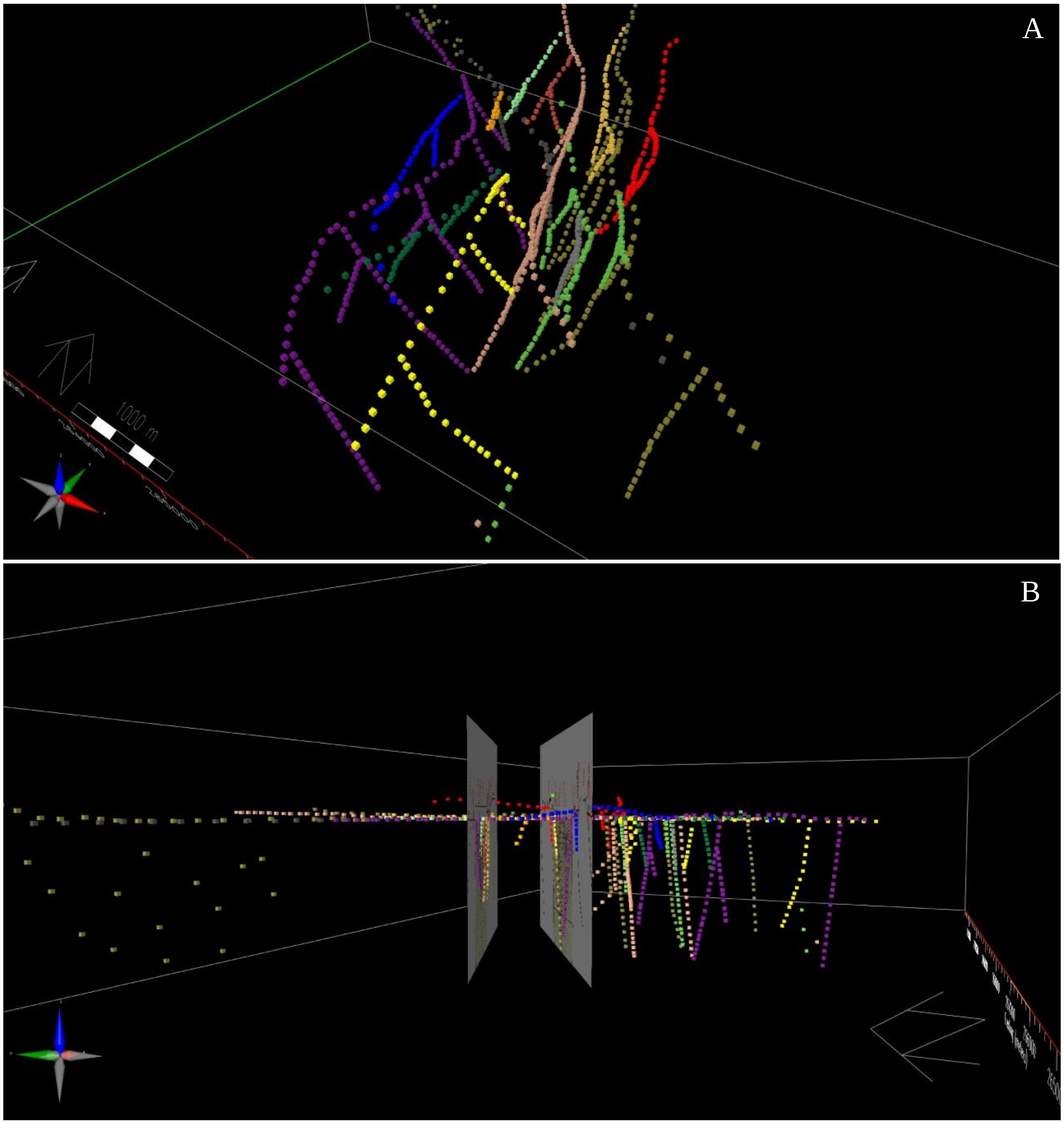

Figure 18. Completed fault digitizing, resulting in 19 faults each represented by a different color. A. Looking northwest from above the model. B. Showing subsurface fault controls looking northeast at ground level. Seismic reflection images are ~1200 m deep. Model area is 4 by 3 km wide shown by the outline box.

Along with the surface fault and stratigraphic data contained in the cross sections, interpreted faults on each seismic reflection line were added to each cross section. These faults were then linked to their respective surface traces when digitized (Figure 18). The cross sections were constructed to depths averaging 1500 m, dependent on topography.

This also corresponded with the maximum well depth of 1379 m and formed the vertical constraint of the 3D model (Figure 19).

Well data input into the model was derived from well logs using xyz data and modified by the analysis of well cuttings. The logs and analysis of cuttings allowed for detailed picks of lithologic contacts, possible fault zones, lost circulation zones, and areas of notable mineral alteration. These lithologic data were then simplified for input into the model into 17 lithologic units shown in the model (Figure 16).

Fault Modeling

Faults were generated by manually digitizing data points along the corresponding lines of input surfaces and control points. Each fault data file produced from the surface fault trace was modified to include digitized traces found on cross sections and additional control points from wells where available (Figures 14 and 16). EarthVision grids each file of digitized points into a surface using 2D minimum tension gridding with trend control. This gridding algorithm uses a 2nd derivative of curvature control to honor the data as closely as possible in conjunction with adding a tension parameter to eliminate large oscillations and extraneous inflection points (Smith and Wessel, 1990). These fault surface grid files are placed into a fault tree hierarchy, dictating the cross-cutting and intersection relationships between all faults in the model. Faults with higher priority and certainty are implemented higher into the fault tree, as they have greater influence on the model (Jolie et al., in press). Dying faults and other boundary conditions are then added to these grid files before computation. Each fault is subsequently modified with additional control points after gridding has been completed to account for algorithm errors and geologic and geometry accuracy if needed. A total of 19 faults were included in the Astor Pass model.

Horizon Modeling

Modeled horizons were constructed primarily with input from the detailed geologic map (Vice, 2008) and the analysis of well cuttings from APS-1, 2, and 3. The number of specific stratigraphic horizons was simplified for this model because of repeating units and ease of model building. Seventeen distinct stratigraphic horizons were used in the Astor Pass model. The EarthVision software models horizons from the bottom of the model upward, using the lowest layer as a reference depositional layer. It then computes additional horizon layers based on the previous, lower horizons following three general rules. The first rule is deposition, placing horizon layers as they would have been deposited in a bottom up sequence.

True vertical stratigraphic thickness is used for depositional horizons, calculated from well and surface measurements. The other two horizon modeling rules concern erosion and unconformities, as well as discontinuous units. Horizons with erosional contacts or discontinuous bodies are not modeled by thickness but rather with a reference erosional surface cutting into depositional surfaces. In the Astor Pass model, this includes the unconformity at the base of the Quaternary, rhyolite bodies, and the DEM surface topography (Figure 20). Because of the discontinuous nature of rhyolite flows and domes in the study area and surrounding region, these units are modeled as separate, individual horizons using the unconformity rule (Figure 20). This rule uses both erosional and depositional characteristics to erode and fill model space. Modeling rhyolites in Astor

Pass was further hindered by poor lateral control resulting from the tight well spacing with respect to the model volume. Therefore, these units were modeled compatible with rhyolites found in nearby surface outcrops for extent and thickness.

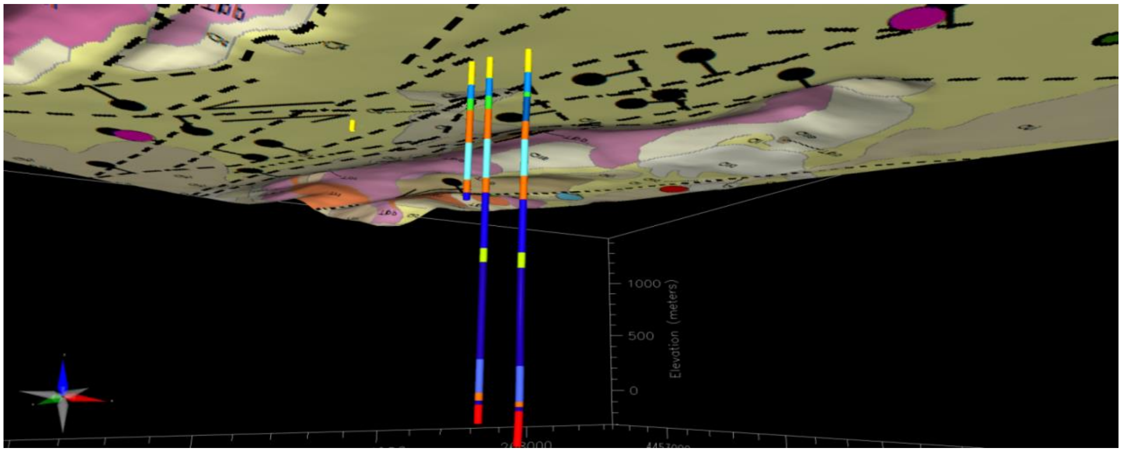

Figure 19. Well data model input from below looking upward at the model surface. Colors reference unit groups: basement – red, andesites and basalts – blues and greens, rhyolite bodies – orange, and Quaternary – yellow.

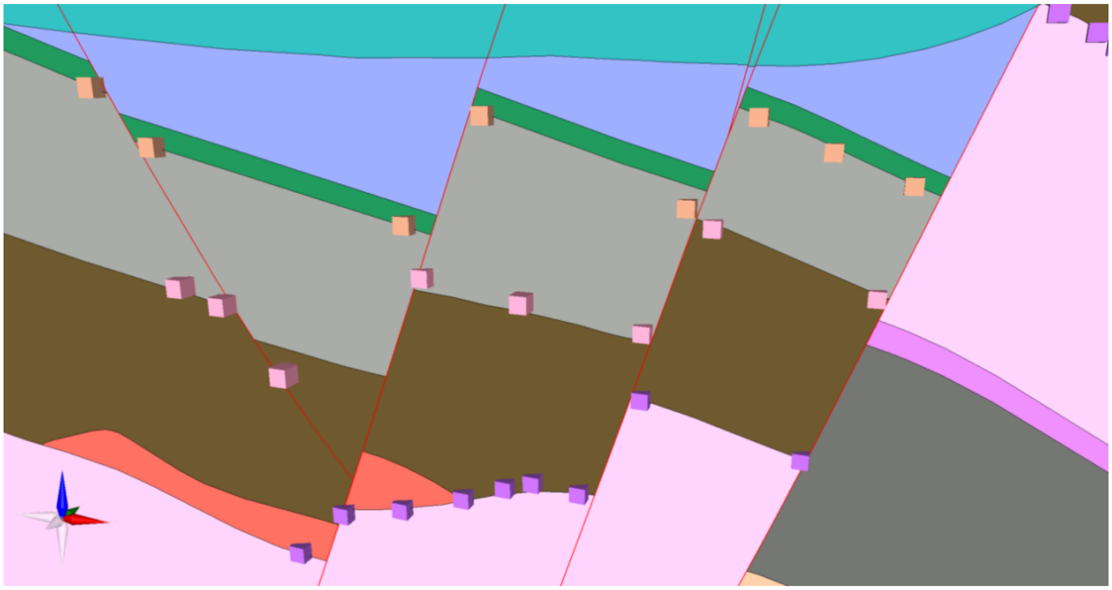

Figure 20. Horizon modeling. Each horizon uses control points in individual fault blocks to conform to known fault offsets and stratigraphic thickness. Note the teal Quaternary surface at the top of the figure etched into the volcanic light blue surface below. Also, note the salmon-colored discontinuous rhyolite unit modeled as an intrusion invading the brown volcanic unit.

Model Results

Complete, the Astor Pass model is composed of 20 faults and 17 separate stratigraphic horizons covering ~12 km^2 and 1500 m of depth (Figure 21). The model allows a revealing 3D perspective into the associations between various surfaces throughout Astor Pass, such as fault intersections, fault/strata interactions, and comparing faults/stratigraphy to geophysical anomalies. It also provides a critical framework for hydrologic studies in the area. This also allows a view into important fault relationships and their proximity to the current production wells and therefore facilitates planning of future exploration of the geothermal system. In addition to viewing these geologic associations, the completed fault model can be further explored using the stress data calculated from the borehole breakouts. By using the stress field calculated from the breakout data, slip and dilation tendency analysis can be calculated to determine which faults may be more likely to contain deep-circulated geothermal fluids.

Slip and Dilation Tendency Analysis

Slip and dilation tendency analysis is a method of using stress data to determine which faults are more favorably oriented for slip and/or dilation. Hydrothermal fluids in can quickly seal any faults or fractures in the absence of recent ruptures. Continued slip, dilation, and stress on faults and fractures can facilitate fluid flow and maintain these fluid pathways for extended amounts of time (Curewitz and Karson, 1997; Ferrill and Morris, 2003). These zones of high slip and/or dilation show continued fault movement, keeping fluid conduits open and/or generating new fluid pathways, thus constituting excellent drilling targets (Curewitz and Karson, 1997). Zones of fault intersections that contain areas of high slip and/or dilation can possibly enhance this open fluid conduit phenomenon. The 3D structural model affords visual analysis and identification of zones of high slip and dilation, further constraining possible drilling targets.

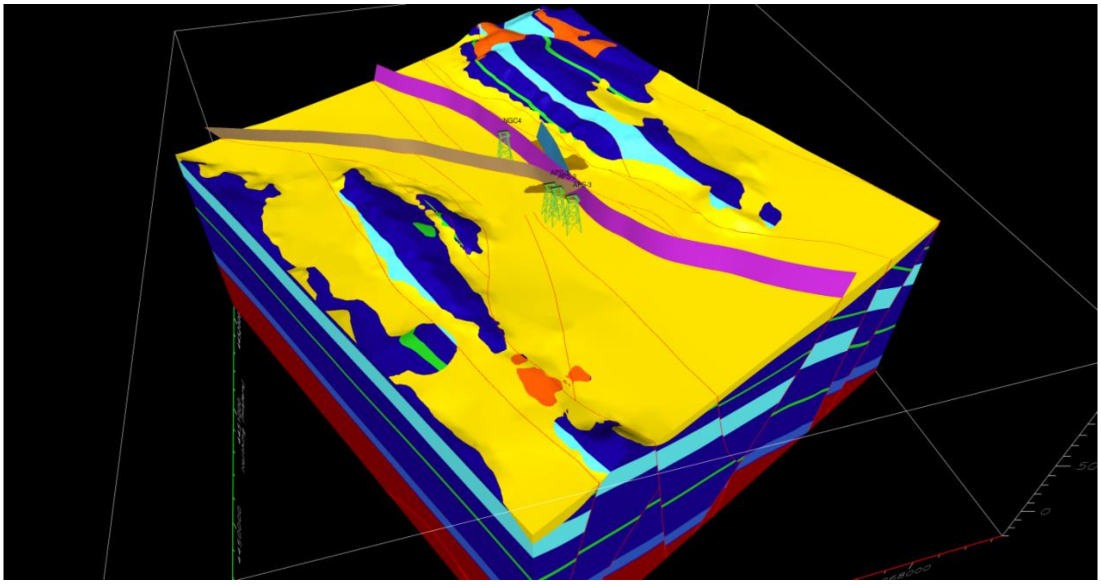

Figure 21. Complete structural model, including 20 faults and 17 horizons. Faults related to the tufa alignments in Astor Pass are shown above the model surface. Well locations are marked by green derricks. Red unit is Mesozoic basement; blue units are middle Miocene basalts and andesites, orange are rhyolites, and yellow are Quaternary deposits. Model area is 3 by 4 km with a depth of ~1500 m.

Slip will likely occur on a plane when the resolved shear stress (component of shear stress resolved in direction of slip) becomes greater or equal to the sliding resistance on that plane (Morris et al., 1996). Actual slip on a surface depends on the cohesive nature of the rock and the coefficient of internal friction of the plane. The coefficient of friction (μ) is proportional to the ratio of shear stress, $\tau,$ over normal stress, $\sigma_n,$ on a plane. Slip tendency is given by (Equation. 7), where the shear stress is greater than or equal to the frictional coefficient (Morris et al, 1996; Moeck et al., 2009).

$$T_s = \frac{\tau}{\sigma_n} \geq \mu \qquad (7)$$

The slip tendency is dependent on the stress field (stress tensor) and the orientation of the surface.

Dilation of a plane is a function of the resolved normal stress, itself a function of lithostatic and tectonic stress, along with fluid pressure (Moeck et al., 2009). Dilation tendency (T_d) is a ratio between the maximum principal stress less the normal stress and the differential stress (Equation 8).

$$T_d = \frac{\sigma_1-\sigma_n}{\sigma_1-\sigma_3} \tag{8}$$

Slip and dilation tendency stereoplots are obtained by resolving the shear and normal stresses for all planes in 3D space. To conduct a slip and dilation tendency analysis, principal stress values are needed. The values for this study were obtained from the stress numbers produced from the borehole breakout calculations. The same assumptions were used for slip and dilation analysis as for the borehole breakout calculations: normal faulting regime, unconfined compressive rock strength of 100 MPa, and frictional coefficients between 0.6 and 1.0.

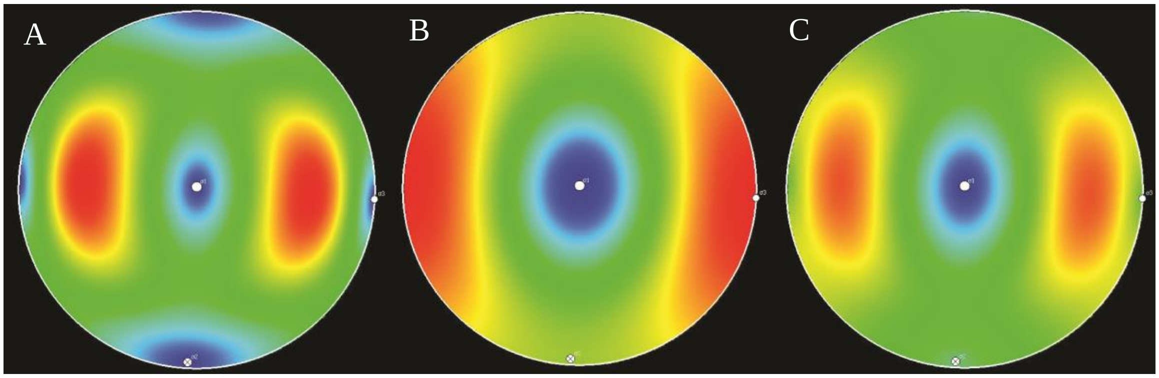

Figure 22. Slip (a), Dilation (b), and combined slip and dilation (c) tendency lower-hemisphere stereoplots using a normal fault stress regime. Warmer colors are higher tendency. High slip tendency for moderate dipping faults striking north-northeast. High dilation tendency for steeply dipping faults striking north to north-northeast. North-northeast striking faults of moderate to steep dips show high slip and dilation tendency.

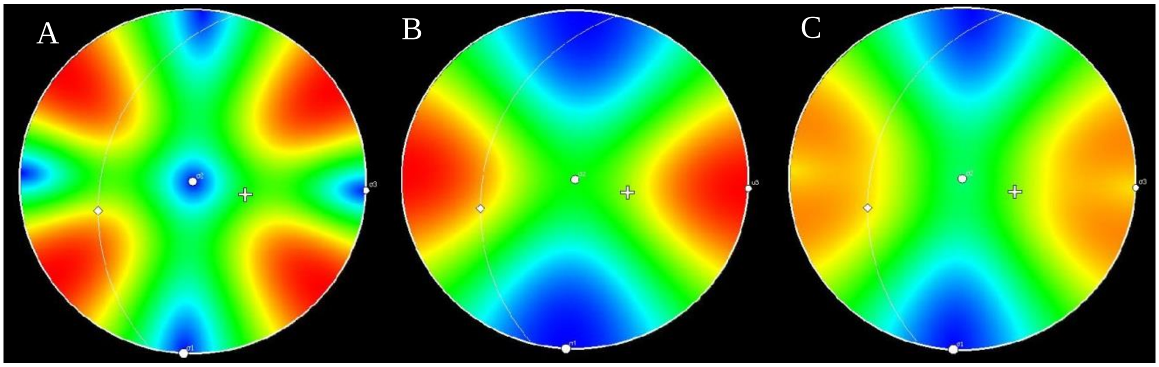

Figure 23 Slip (A), dilation (B), and slip and dilation (C) tendency shown on lower-hemisphere stereoplots using a strike-slip fault regime. Horizontal stress magnitude of 45 MPa. Warmer colors indicate higher tendency. High slip tendency for moderate to steeply dipping northwest- and northeast-striking faults. High dilation tendency for north-striking faults that are moderate to steeply dipping.

Stress value profiles of the vertical and horizontal stresses from the breakout data were then input into the 3DStress program to compute slip and dilation tendency for all possible planes (Figure 22 and 23). 3DStress allows for easy construction and viewing of stress data stereoplots using data from the borehole breakout analysis. These stereoplots were then transferred as separate slip and dilation values onto the modeled 3D fault surfaces in EarthVision (Figures 24 and 25). This allows for analysis of partial, narrow sections of fault surfaces, as well as interactions with other faults and fault intersections.

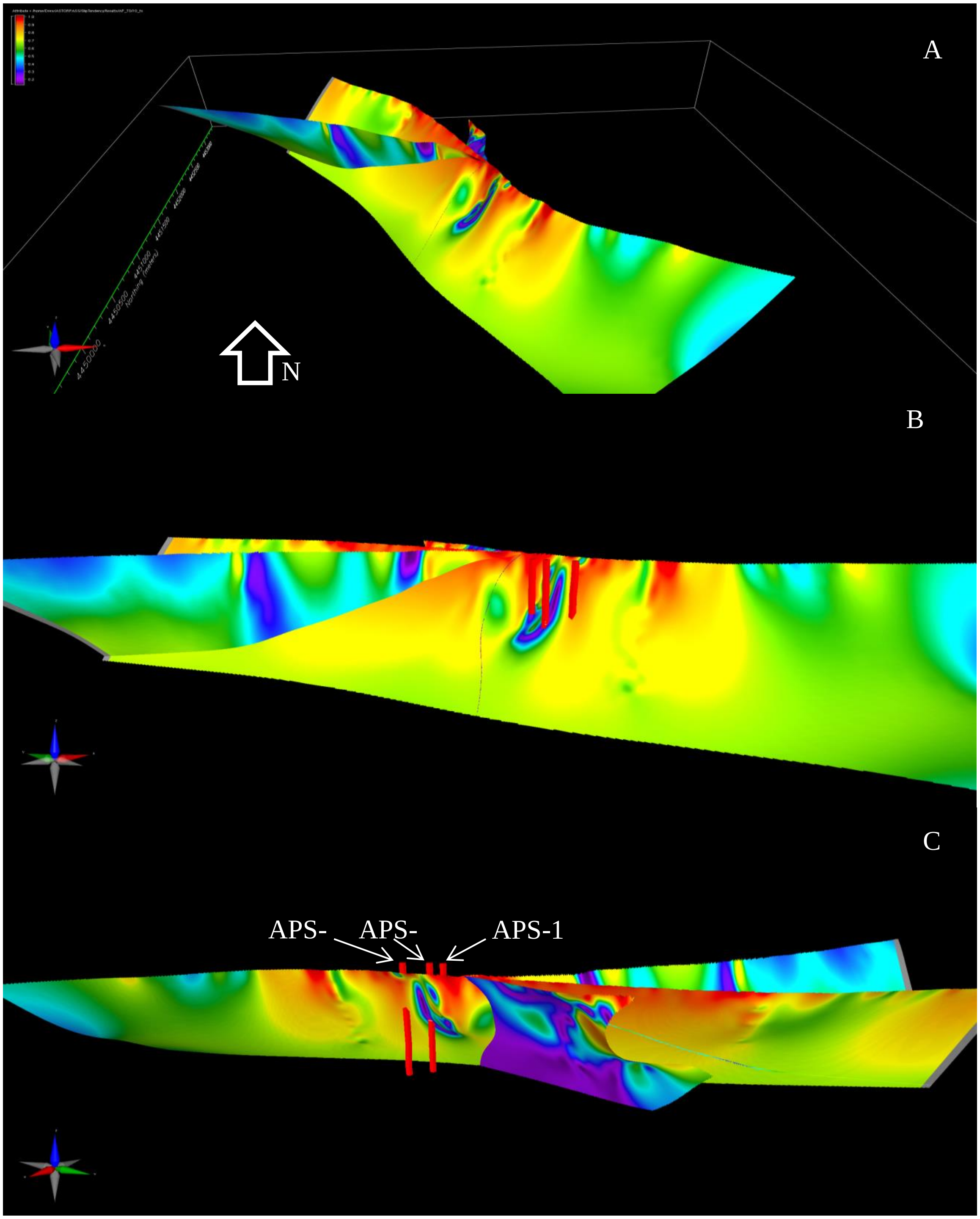

Figure 24 Slip Tendency for three faults controlling the tufa mounds using a strike-slip fault regime. Warmer colors are higher slip tendency. Notice slip variations along the same fault with length and depth. Vertical red paths are APS-1, -2, -3 from north to south, respectively. Green arrow on compass points north. Vertical scale is ~1500 m, longest fault segment is ~4 km in length.

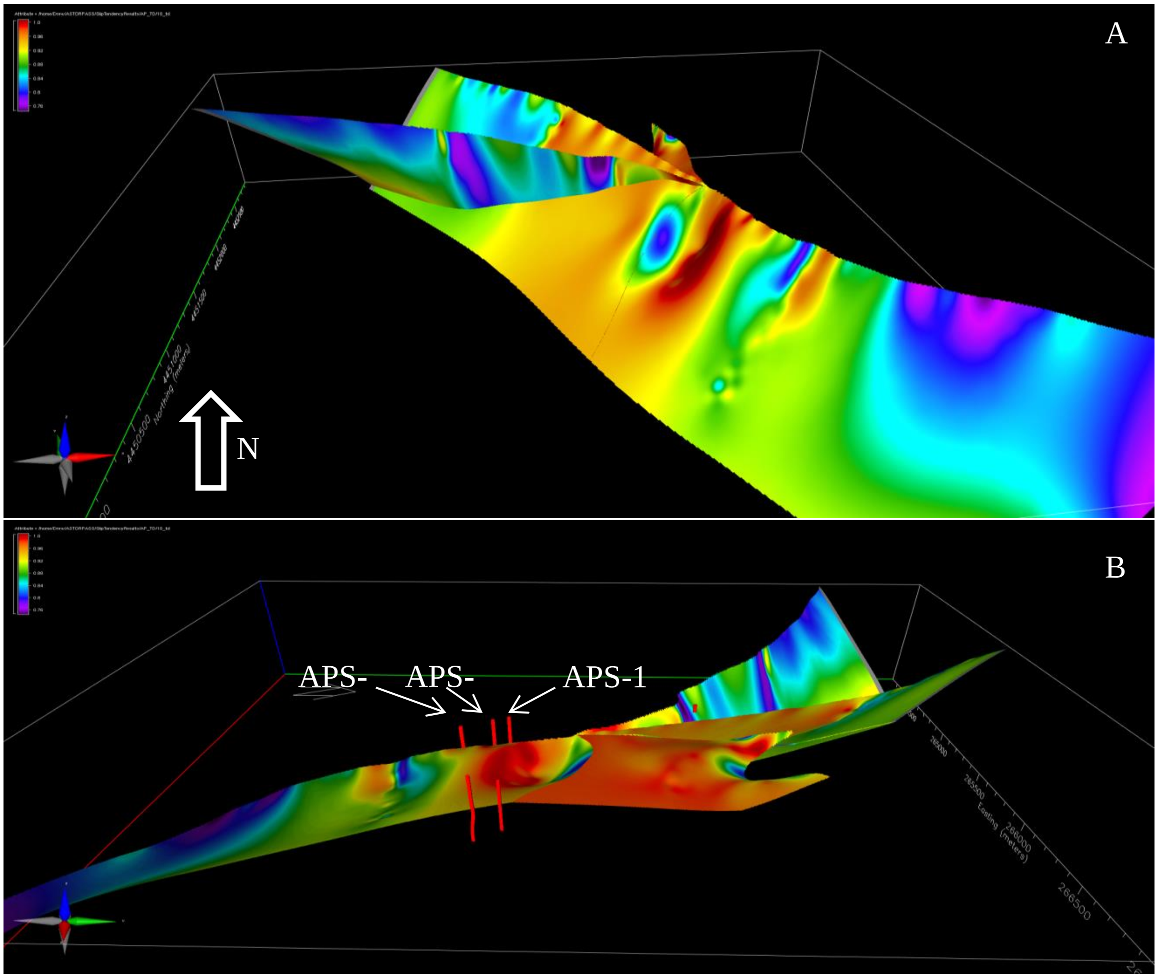

Figure 25. Two views of dilation tendency assuming a strike-slip stress regime of the 3 faults currently thought to control the tufa mounds. Wells shown in second figure just southwest of the tufa mounds. Warmer colors mark higher dilation tendency. Highly dilational zone penetrated by all three wells is not associated with any known lost circulation or fault zones. Green arrow on compass points north. Vertical scale of faults is ~1500 m, longest fault segment is ~4 km.

Discussion

Stress Implications at Astor Pass

The majority of geothermal systems in the Great Basin reside in an extensional setting. Critically stressed faults, fractures, and dilatant fault intersections oriented perpendicular to the least principal stress control upwelling fluids (Faulds et al., 2006, 2011a; Moeck et al., 2009). Understanding the stress regime is thus important to identifying the critical structural features of the Astor Pass geothermal system.

The measured stress azimuths at Astor Pass generally agree with collected data from nearby geothermal systems and regional geodetic studies. Emerson Pass (~280°), San Emidio (~299°), and Desert Peak (294°±17°) all display minimum horizontal stress directions trending west-northwest to east-west (Hickman and Davatzes, 2010; Rhodes et al., 2011; Anderson, 2013). The fluid controlling faults in these systems strike approximately orthogonal to the least principal stress (e.g., Faulds et al., 2010; Rhodes et al., 2011; Anderson, 2013). On the basis of borehole breakout data, the minimum horizontal stress direction at Astor Pass trends west-northwest (273°), more east-west than other measurements from throughout the region. Regional studies from earthquake and geodetic data suggest an extensional direction of ~N70W°-N80W°, very similar to Emerson and Astor Pass (Ichinose et al., 2003; Kreemer et al., 2009).

Interestingly, although the stress azimuths at Astor Pass are similar to those from throughout the region, the borehole breakout data show a maximum principal stress that could be horizontal instead of vertical, as assumed at Emerson Pass, San Emidio, and

Desert Peak. If one assumes that Astor Pass falls under a normal-faulting stress regime and calculates stress magnitudes using the breakout width method, the resulting values actually show a strike-slip stress regime. However, the stress magnitudes are slightly uncertain due to their reliance on the actual unconfined compressive rock (UCS) strength. Unconfined rock strength values for common basalts and andesites typically vary from 100-300 MPa. Even using the lower bound of 50 MPa UCS, the Astor Pass stress data still show a strongly strike-slip environment instead of a dominant vertical stress or extensional stress regime (Figure 9). For a general basaltic rock to have a UCS of 50 MPa, it would need to be moderately to severely weathered with a moisture content above 5% (Gu et al., 2008), not typical of the rock observed in wells APS-2 and APS-3 at the depths the breakout data were collected.

Another assumption brings a different result. If one assumes a strike-slip stress regime at Astor Pass and uses drilling-induced tensile-fractures to solve for the maximum horizontal stress, the results show a weak normal-faulting stress regime (Figure 26). The magnitudes of the estimated vertical stress and maximum horizontal stress are within a few MPa of each other. Because the calculations for both methods use multiple non-discrete variables and rock properties could sway the data significantly, Astor Pass is likely in an area of transtension, exhibiting traits of both strike-slip and normal faulting regimes. Applying the slip and dilation tendency analysis from these stress data to the fault model at Astor Pass shows some interesting qualities regarding fluid flow.

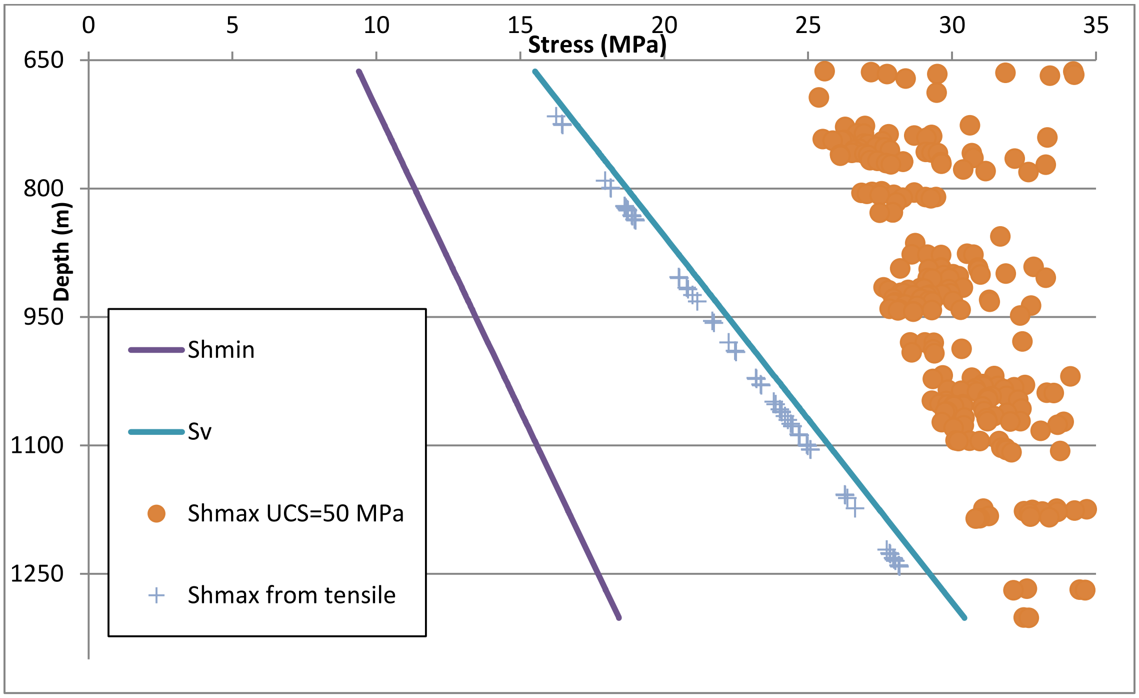

Figure 26. Stress data from APS-3 showing maximum horizontal stress calculated from UCS rock strength (normal faulting regime) and tensile fractures (strike-slip faulting regime).

Slip tendency differs dramatically in assuming a strike-slip or normal faulting regime. One of the three faults that intersect the tufa mound at Astor Pass is a known oblique-slip fault striking ~N55W-N75W°. Assuming a strike-slip stress regime, this fault exhibits a moderate slip tendency (Figures 23 and 24). The slip tendency is diminished for the more north-northwest-striking normal faults in the model area relative to the optimally oriented northwest-striking faults, but some of the more northerly striking faults still exhibit moderate slip tendency (Figure 24). Assuming a normal faulting regime, the slip tendency changes quite dramatically, favoring moderate to steeply dipping, northerly striking faults (Figures 22 and 27). This limits the slip tendency on most faults in the Astor Pass model, as faults in the area predominately strike north-northwest except for a few smaller fault segments at the north and southwest section of the model space.

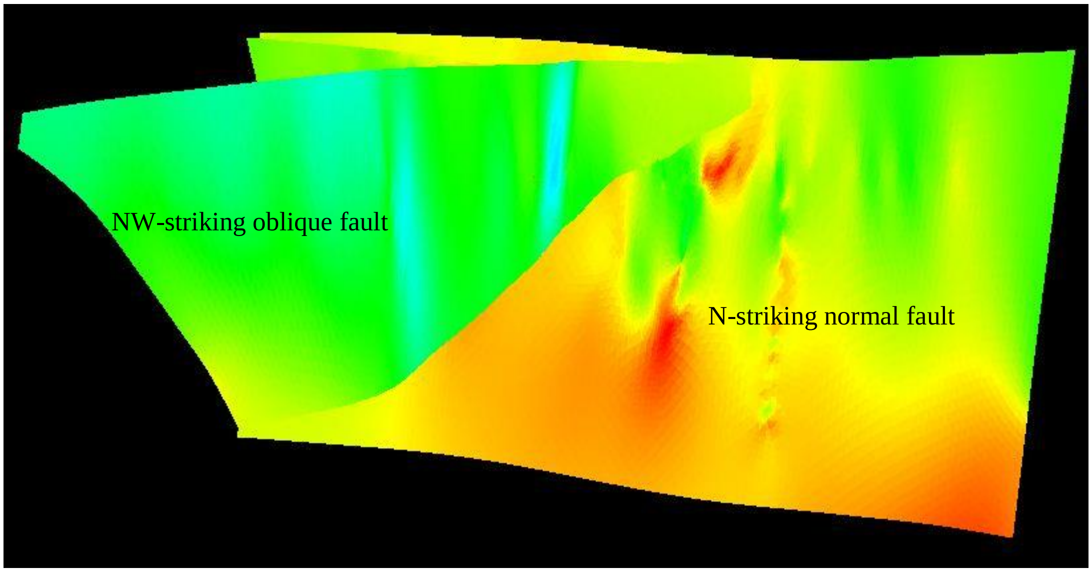

Figure 27. Figure showing slip tendency on two of the faults intersecting the tufa mound. Warmer colors indicate higher slip tendency. Oblique view looking northeast. North-striking normal fault segment is ~4 km long.

Dilation tendency differs from slip tendency in that north-striking, moderate to steeply dipping faults have the highest tendency to dilate in both strike-slip and normal faulting regimes (Figures 22, 23, and 25). The range of strikes for favorable dilation tendency is relaxed as well, allowing for a higher number of the north-northwest-striking faults to fall into a zone of relatively high dilation tendency. Faults in the Astor Pass model are generally steeply dipping, > 70°, falling in the middle range of acceptable dips for high dilation tendency. Moderate dips of less than 70° show high dilation tendency on north-striking faults for strike-slip and normal regimes, but faults striking north-northwest or north-northeast require high dips (Figure 23 and 25) to maintain the same dilation tendency.

This transtensional regime results in the majority of Astor Pass faults showing moderate slip tendency, with many of these faults also exhibiting moderate to high dilation tendency. This places most of the faults in the Astor Pass model in a position for generating permeable conduits and maintaining current fracture and fluid networks. The level of recent movement on individual faults in the model is unknown. Only one fault has an exposed surface, and many of the faults have only been imagined in seismic reflection data. Further, earthquake data for the area are not specific enough to attribute to individual faults.

Thus, the type of active slip regime in the model area is poorly understood. Astor Pass could be simultaneously active in strike-slip and pure extension, these slip regimes may alternate activity, or strike-slip activity could dominate, reactivating preferentially oriented, preexisting normal faults. Regardless of the current type of fault movement, the modeled area of Astor Pass contains a high number of critically stressed faults with high slip and dilation tendency, producing a large area of high fault and fracture density that corresponds to high permeability and transmissivity.

Controls on the Astor Pass Geothermal System

The majority of geothermal systems in the Great Basin are extensional, relying on critically stressed faults, fractures, and dilatant faults and fault intersections oriented perpendicular to the least principal stress to control upwelling fluids (Faulds et al., 2006, 2011a; Moeck et al., 2009). The 3D structural model of Astor Pass in conjunction with slip and dilational tendency analysis of stress data allow a detailed examination and characterization of the Astor Pass geothermal system at depth. The structural model initially shows all of the hallmarks of other productive Great Basin geothermal systems: high concentration of critically stressed faults and fractures conducive to fluid flow, with many of these structures favorably oriented to take advantage of the local stress field and therefore exhibiting high slip and dilation tendency.

The 3D model also allows for investigation of specific areas of concentrated fault intersections. Two areas in particular appear important to fluid flow near the surface: 1) A north-northwest trending fault intersection moderately plunging away from the tufa mound supplemented by multiple smaller faults interacting with this intersection at depth (Figure 28 and 29) a subvertically plunging fault intersection between three faults found directly beneath the tufa mound (Figure 29). If the critically stressed faults in Astor Pass were indeed controlling fluid flow to near surface levels, these two intersection swarms would warrant further investigation. Both of these intersections areas approach the surface at the location of the tufa mound, close to a shallow temperature gradient hole, the source of the highest measured temperatures at Astor Pass. This suggests that a fault or fault intersection controls fluids and generated the tufa mound. The moderately plunging fault intersection is particularly interesting, because a number of additional small faults interact with the main intersection near the Tertiary-Mesozoic basement contact.

This basement contact is important, because the hydrologic model of Astor Pass shows a fairly impermeable basement (Reeves et al., 2012), albeit relatively little is known about the basement as wells only penetrated its uppermost part. The highly fractured Miocene volcanic section above the basement appears to constitute the primary geothermal reservoir, with the basement lacking widespread transmissivity. Thirty-day flow tests show a large, robust reservoir with little drawdown and no significant temperature variations, with shallow wells over 1 km away near the surface reacting to pumping at the base of the Tertiary volcanic section (Pyramid sequence). This suggests that faults, at least above the Mesozoic basement rocks, are not inhibiting or focusing fluid flow, and that the overall fracture density and permeability in the volcanic rocks is high enough to broadly diffuse any upwellings of hot fluids coming up along discrete faults.

The source location(s) of these hot, upwelling fluids through the basement remains unknown. Of the two fault intersection areas described above (Figures 25 and 26), the subvertical intersection is not likely to be the primary control on hot fluids because of the lack of temperature increase within the nearby APS-3 well during flow testing. However, this fault intersection probably controlled fluid flow in the latest Pleistocene, as evidenced by the large tufa tower directly above it.

The moderately plunging fault intersection is ~2 km to the northwest of the APS wells and has a greater possibility as the source of the basement fluid conduit. Unlike the subvertical intersection beneath the tufa, the shallowly plunging intersection contains a known oblique-slip fault, which may be more active based on the current transtensional stress field. If this intersection area is indeed the primary basement fluid conduit, pumping the aquifer from a 2 km distance did not measurably affect this conduit in its fluid delivery to the APS well locations.

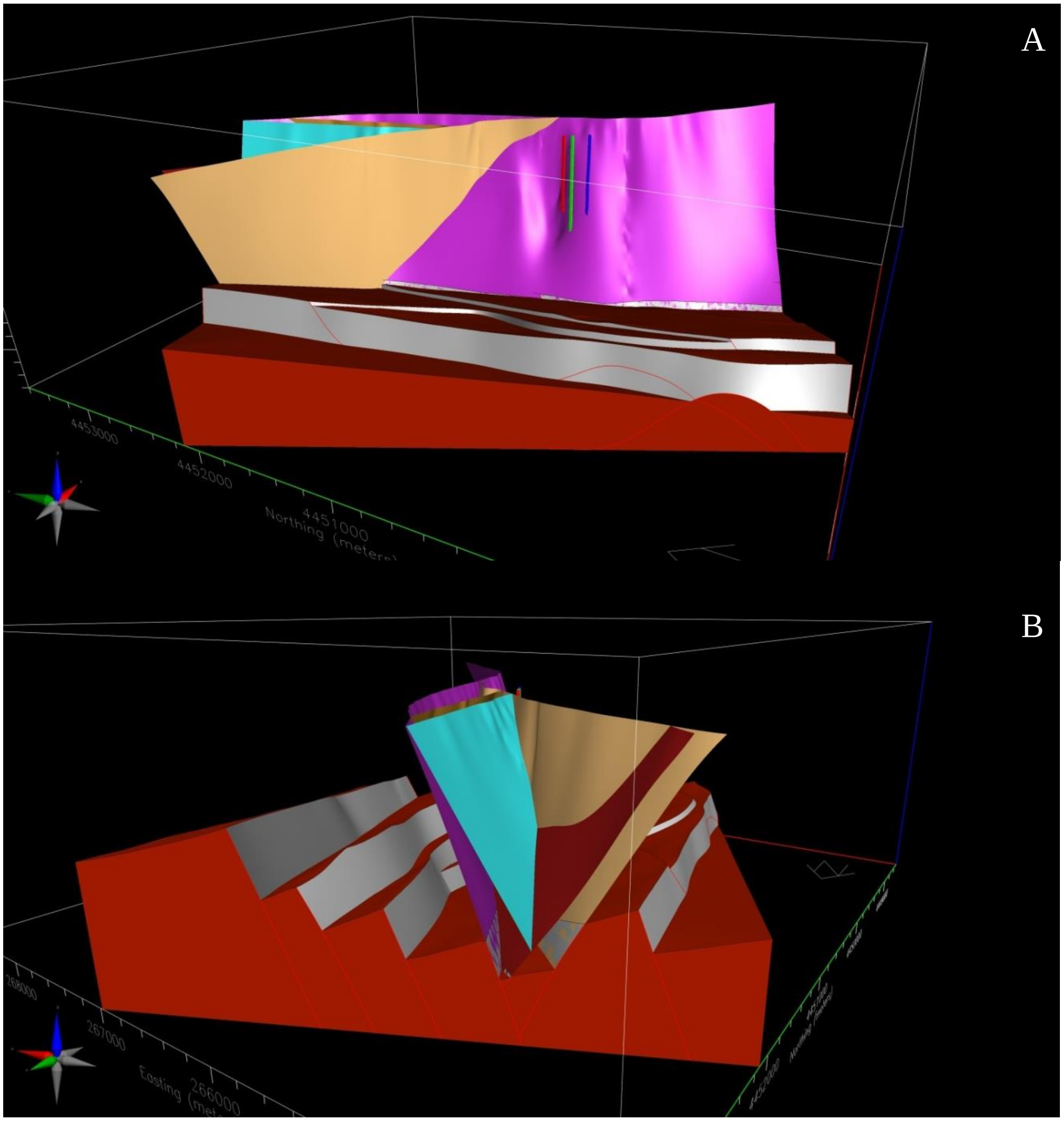

Figure 28. A. Looking northeast at the moderately plunging fault intersection between the brown oblique-slip fault and purple normal fault, which is ~4 km long. B. Looking southeast at the high intersection density of smaller faults as the plunging fault intersection enters the basement. Faults are ~ 1 km in height with no vertical exaggeration.

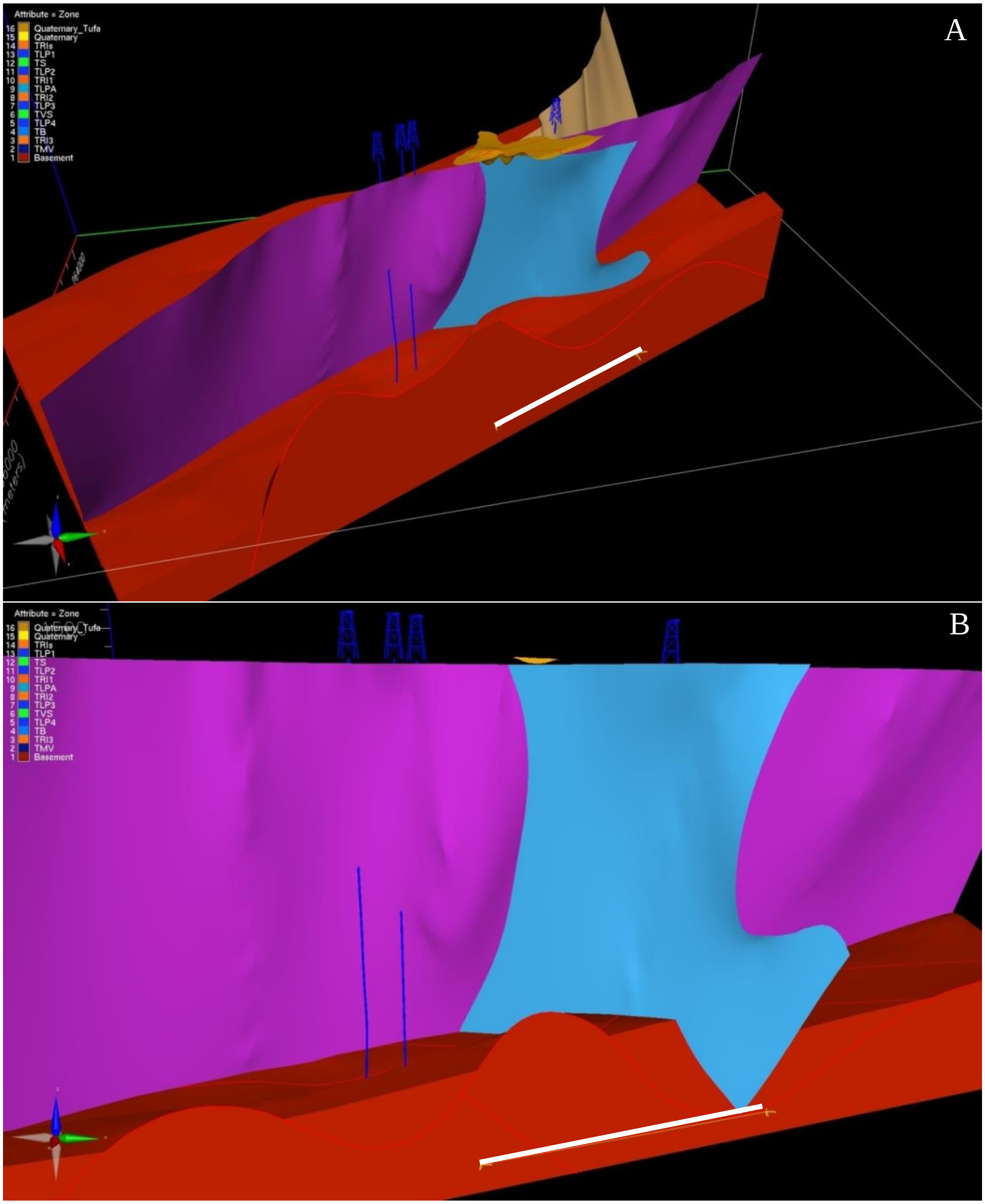

Figure 29. Vertical fault intersection below the tufa mound, shown in light orange on the surface. Intersection involved main north-northwest striking normal fault (purple) and small blue fault striking northeast (A). Wells APS-2 and APS-3 penetrate through the purple fault but are 100's of meters from the fault intersection (B). Red stratigraphic layer represents the modeled basement rocks. Green arrow points north, White line is 1 km for scale.

Although both fault intersection models structurally agree with a discrete fluid upwelling approaching the surface at the tufa mounds, the limited hydrologic testing at APS-3 and transmissivity of the Miocene volcanic section do not support this interpretation. However, the flow test was only performed at a single location, multiple kilometers from the moderately plunging fault intersection at depth. Further testing closer to this moderately plunging fault intersection would be needed to constrain its effect on fluid flow at Astor Pass and the tufa mound.

Although Astor Pass may lack ideal temperatures for large binary geothermal power production within the Pyramid sequence, it does offer a robust reservoir and high overall transmissivity in the Miocene volcanic section. Furthermore, it resides in a transtensional stress regime and contains many faults with high slip and dilation tendency. Thus, Astor Pass could probably sustain development of a low-temperature geothermal system, applicable to many direct uses, and possibly for low-level power generation. Alternatively, future exploration could target some of the major fault intersections within the basement and potential feeders of a relatively high-temperature system (e.g., ~130^{o}C based on geothermometry).

In addition, the evidence for a broadly dispersed geothermal reservoir at Astor Pass may have analogs in the western U.S. For example, the Snake River Plain is a region of high geothermal gradient and thick (e.g., 1800 m at the Mountain Home geothermal system) section of volcanic rocks, primarily basalts and rhyolites (Arney et al., 1982; Fleischmann, 2006). Temperatures in many areas are greater than at Astor Pass, between 100° and 150°C, but have yet to be developed into geothermal power plants. The geothermal system at Mountain Home Air Force Base has wells producing artesian water @150°C at a depth of ~1800 m (Lachmar et al., 2012). The aquifer for this system is basalt and rhyolite (Lachmar et al., 2012; Delahunty et al., 2012). Other sites, such as Mount Bennett Hills, have completed successful flow tests of 10,000 gpm with reservoir temperatures at 132°C in interbedded basalts and rhyolites, but the lower sustained temperature dissuaded further development when the pump test was conducted in the early 1980's (Arney et al., 1982; Fleischmann, 2006). The structure of Mount Bennett Hills is also similar to Astor Pass, consisting of northwest-striking, steeply dipping normal faults that enhance the permeability of the volcanic section (Arney and Goff, 1982).

A second approach to exploring analogs to the Astor Pass system involves sedimentary hosted geothermal reservoirs in some of the deep basins in the eastern Great Basin. A potential geothermal reservoir using rocks beneath the Tertiary basin sediments would require high permeability, heat flows greater than 80 mW/m^2, reservoir temperatures greater than 175°C, and depths of less than 4 km (Allis et al., 2013). The heat flow is high enough in the Great Basin that reservoirs of highly permeable Paleozoic rocks could be fractured and used in a larger scale EGS (enhanced geothermal system) development. Temperatures in oil exploration wells have been recorded at over 200°C at less than 4km depth in permeable Paleozoic carbonate units. But aside from their high temperatures, these potential reservoirs are massive, spanning hundreds of square kilometers (Allis et al., 2013). With further exploration, these basin-centered reservoirs could provide an alternative to geothermal systems focused on targeted upwelling.

Similarly, vast reservoirs may also reside in fractured volcanic rocks, and such systems may ultimately facilitate greater development of geothermal energy in the Great Basin and adjoining regions than currently projected.

Conclusions and Implications

Construction of the Astor Pass 3D model from analyses of seismic reflection profiles, drill cuttings, stress field, and geologic mapping have allowed for characterization of the geothermal system. Astor Pass is identified by its tufa mound in the center of the pass and characterized as a transtensional fault intersection. It lies between the Virginia Mountains and the Terraced Hills, which consist primarily of moderately east-tilted fault blocks bound by west-dipping normal faults. These west-dipping normal faults also interact with a number of northwest-striking oblique-slip faults and east-dipping faults, forming complex transtensional fault intersection areas. The fault blocks are composed of middle Miocene Pyramid sequence volcanic and sedimentary rocks that nonconformably overlie Mesozoic granitic, metavolcanic, and metasedimentary basement.

Stress field data derived from borehole breakout data show a west-trending least principal stress direction, compatible with regional geodetic, kinematic, and focal mechanism data. Stress magnitudes are more complex, with a strike-slip or normal faulting stress regime depending on how the raw data are interpreted. Slip and dilation tendency analysis on all of the faults in the model area show faults and fault intersection areas that have a high propensity for slip and/or dilation in both stress regimes. Two separate fault intersection areas show the highest tendency for slip and dilation. One involves an oblique-slip fault and prominent normal fault plunging moderately to the northwest away from the tufa mound. The second is a subvertical intersection beneath the tufa mound. These may be areas to focus on for future exploration, but hydrologic studies suggest that the Pyramid sequence is too permeable and transmissive to support discrete fault-fluid conduits. However, these fault intersections as they enter the relatively impermeable basement rocks might provide discrete fluid pathways for geothermal fluids and therefore represent promising exploration targets.

Drilling at Astor Pass confirms a moderate temperature geothermal system with temperatures peaking at 95°C in a large, diffuse reservoir, capable of sustaining high pump rates. Though probably not capable of supporting a large binary geothermal power plant, the Astor Pass system may support a direct-use application and/or a small power plant, while also proving useful as an analog in exploration and development of other geothermal systems in large, permeable reservoirs. Higher temperature systems in deep sedimentary basins of the eastern Basin and Range and the thick, highly fractured volcanic rock in the Snake River Plain both contain large, permeable reservoirs for geothermal systems that are not controlled by discrete fault-fluid conduits. The detailed 3D geologic characterization at Astor Pass may provide valuable information in efficiently exploring and developing these analogous systems.

References

Allis, R., Moore, J.N., Anderson, T., Deo, M., Kirby, S., Roehner, R., and Spencer, T., 2013, Characterizing the power potential of hot stratigraphic reservoirs in the Western U.S.: Stanford Workshop on Geothermal Reservoir Engineering, v. 38, p. 1–11.

Anderson, E. M., 1951, The dynamics of faulting and dyke formation with applications to Britain: Edinburgh, Oliver and Boyd, 206 p.

Anderson, R, 2013, Structural controls of the Emerson Pass Geothermal System, Washoe County, Nevada: [M.S. Thesis]: University of Nevada, Reno, 108 p.

Angelier, J., 1984, Tectonic analysis of fault slip data sets: Journal of Geophysical Research, v. 89, p. 5835–5848.

Arney, B.H., Goff, F., and Harding Lawson Associates, 1982, Evaluation of the hot-dry-rock geothermal potential of an area near Mountain Home, Idaho: U.S. Department of Energy, HDR site selection report no. 6, 74 p.

Barton, C.A., Zoback, M.D., and Burns, K.L., 1988, In-situ stress orientation and magnitude at the Fenton geothermal site, New Mexico, determined from wellbore breakouts: Geophysical Research Letters, v. 15, no. 5, p. 467–470.

Benoit, W.R., Hiner, J.E., and Forest, R.T., 1982, Discovery and geology of the Desert Peak geothermal field: A case history: Nevada Bureau of Mines and Geology Bulletin 97, 82 p.

Blackwell, D.D.., 1983, Heat flow in the northern Basin and Range province: Geothermal Resources Council Special Report 13 p. 81–93.

Blackwell, D.D., Negraru, P.T., and Richards, M.C., 2007, Assessment of the enhanced geothermal system resource base of the United States: Natural Resources Research, v. 15, no. 4, p. 283–308.

Bonham, H.F., and Papke, K.G., 1969, Geology and mineral deposits of Washoe and Storey Counties, Nevada: Nevada Bureau of Mines and Geology Bulletin 70, scale 1:250,000, 140 p.

Briggs, R.W., and Wesnousky, S.G., 2004, Late Pleistocene fault slip rate, earthquake recurrence, and recency of slip along the Pyramid Lake fault zone, northern Walker Lane, United States: Journal of Geophysical Research, v. 109, p. 1–16.

Briggs, R.W., Wesnousky, S.G., and Adams, K.D., 2005, Late Pleistocene and late Holocene lake highstands in the Pyramid Lake sub basin of Lake Lahontan, Nevada, USA: Quaternary Research, v. 64, p. 257–263.

Cashman, P.H., and Fontaine, S. A, 2000, Strain partitioning in the northern Walker Lane, western Nevada and northeastern California: Tectonophysics, v. 326, p. 111–130, doi: 10.1016/S0040-1951(00)00149-9.

Coolbaugh, M.F., Faulds, J.E., Kratt, C., Oppliger, G.L., Shevenell, L., Calvin, W., Ehni, W.J., and Zehner, R.E., 2006, Geothermal potential of the Pyramid Lake Paiute Reservation, Nevada , USA: Evidence of previously unrecognized moderate-temperature (150-170°C) geothermal systems: Geothermal Resources Council, v. 30, p. 59–68.

Curewitz, D., and Karson, J. A, 1997, Structural settings of hydrothermal outflow: Fracture permeability maintained by fault propagation and interaction: Journal of Volcanology and Geothermal Research, v. 79, no. 3-4, p. 149–168.

Delahunty, C., Nielson, D.L., and Shervais, J.W., 2012, Deep core drilling of three slim geothermal holes, Snake River Plain, Idaho: Geothermal Resources Council Transactions, v. 36, p. 641–648.

Drakos, P.S., 2007, Tertiary Stratigraphy and Structure of the southern Lake Range northwest Nevada: Assessment of kinematic links between strike-slip and normal faults in the northern Walker Lane [M.S. thesis]: University of Nevada, Reno, 165 p.

Eisses, A., 2012, New constraints on slip-rates, recurrence intervals, and strain partitioning beneath Pyramid Lake, Nevada [M.S. thesis]: University of Nevada, Reno, 60p.

Faulds, J.E., Henry, C.D., and Craig, M., 2001, Preliminary geologic map of the Tule Peak Quadrangle, Washoe County, Nevada: Nevada Bureau of Mines and Geology Open-File Report 03-10, scale 1:24,000.

Faulds, J.E., and Henry, C.D., 2002, Tertiary stratigraphy and structure of the Virginia Mountains, western Nevada: Implications for development of the northern Walker Lane: Geological Society of America Abstracts with Programs, v. 34, no. 5, p. 84.

Faulds, J.E., Garside, L.J., and Oppliger, G.L., 2003, Structural analysis of the Desert Peak-Brady geothermal fields, northwestern Nevada: Implications for understanding linkages between northeast-trending structures and geothermal reservoirs in the Humboldt structural zone: Geothermal Resources Council Transactions, v. 27, p. 859–864.

Faulds, J.E., Henry, C.D., and Hinz, N.H., 2005a, Kinematics of the northern Walker Lane: An incipient transform fault along the Pacific–North American plate boundary: Geology, v. 33, no. 6, p. 505-508.

Faulds, J.E., Henry, C.D., Hinz, N.H., Drakos, P.S., and Delwiche, B., 2005b, Transect across the northern Walker Lane, northwest Nevada and northeast California : An incipient transform fault along the Pacific – North American plate boundary: Geological Society of America Field Guide 6, p. 129–150, doi:10.1130/2005.fld006(06).

Faulds, J.E., Coolbaugh, M.F., Vice, G.S., and Edwards, M.L., 2006, Characterizing structural controls of geothermal fields in the northwestern Great Basin: A progress report: Geothermal Resources Council Transactions, v. 30, p. 69–76.

Faulds, J.E., and Henry, C.D., 2008, Tectonic influences on the spatial and temporal evolution of the Walker Lane : An incipient transform fault along the evolving Pacific – North American plate boundary: Arizona Geological Society, v. 22, p. 437–470.

Faulds, J.E. and Melosh, G., 2008, A preliminary structural model for the Blue Mountain geothermal field, Humboldt County, Nevada: Geothermal Resources Council Transactions, v. 32, p. 273-278.

Faulds, J.E., Coolbaugh, M.F., Benoit, W.R., Oppliger, G., Perkins, M., Moeck, I., and Drakos, P., 2010, Structural controls of geothermal activity in the northern Hot Springs Mountains, western Nevada: The tale of three geothermal systems (Brady's, Desert Peak, and Desert Queen): Geothermal Resources Council Transactions, v. 34, p. 675–684.

Faulds, J.E., Hinz, N.H., Coolbaugh, M.F., Cashman, P.H., Kratt, C., Dering, G., Edwards, J., Mayhew, B., and McLachlan, H., 2011a, Assessment of favorable structural settings of geothermal systems in the Great Basin, western USA: Geothermal Resources Council Transactions, v. 35, p. 777–783.

Faulds, J., Drakos, P., Vice, G., Mayhew, B., and Noel, D., 2011b, The Pyramid Lake Paiute Reservation, western Nevada (USA): Exploration for blind geothermal systems in a transtensional displacement transfer zone: New Zealand Geothermal Workshop, p. 1–5.

Ferrill, D. A., and Morris, A.P., 2003, Dilational normal faults: Journal of Structural Geology, v. 25, no. 2, p. 183–196.

Fleischmann, D.J., 2006, Geothermal development needs in Idaho: Geothermal Energy Association, U.S. Department of Energy, 51 p.

Garg, S.K., Pritchett, J.W., Wannamaker, P.E., and Combs, J., 2007, Characterization of geothermal reservoirs with electrical surveys: Beowawe geothermal field: Geothermics, v. 36, no. 6, p. 487–517.

Gu, D.X., Tamblyn, W., Lamb, I., and Ramsey, N., 2008, Effect of weathering on strength and modulus of basalt and siltstone: American Rock Mechanics Association, v. 42, p. 1–8.

Hammond, W.C., and Thatcher, W., 2004, Contemporary tectonic deformation of the Basin and Range province, western United States: 10 years of observation with the global positioning system: Journal of Geophysical Research, v. 109, no. B8, p. 1–21.

Hammond, W.C., 2009, Geodetic constraints on contemporary deformation in the northern Walker Lane : 3. Central Nevada seismic belt postseismic relaxation: Geological Society of America Special Paper 447, no. 03, p. 33–54, doi: 10.1130/2009.2447(03).

Hammond, W.C., Blewitt, G., and Kreemer, C., 2011, Block modeling of crustal deformation of the northern Walker Lane and Basin and Range from GPS velocities: Journal of Geophysical Research, v. 116, no. B4, p. 1–28.

Henry, C.D., Faulds, J.E., and Craig, M., 2007, Geometry and timing of strike-slip and normal faults in the northern Walker Lane, northwestern Nevada and northeastern California: Strain partitioning or sequential extensional and strike-slip deformation?: Geological Society of America Special Paper 434, p. 59–79.

Henry, C.D., Faulds, J.E., Craig, M., and Davis, D.A., 2004, Geologic map of the Dogskin Mountain Quadrangle, northern Walker Lane, Nevada: Nevada Bureau of Mines and Geology Map 148, scale 1:24,000, p. 13.

Henry, C., McGrew, A., Colgan, J., Snoke, A., Bruseke, M., 2011, Timing, distribution, amount, and style of Cenozoic extension in the northern Great Basin, *in* Lee, J., and Evans, J., ads., Geologic Field Trips to the Basin and Range, Rocky Mountains, Snake River Plain, and Terranes of the U.S. Cordillera: Geological Society of America Field Guide 21, p. 27-66.

Hickman, S., Davatzes, N., 2010, In-situ stress and fracture characterization for planning of an EGS stimulation in the Desert Peak geothermal field, Nevada, Proceedings, Twenty-Fifth Workshop on Geothermal Reservoir Engineering, Stanford University, Stanford, California, SGP-TR-188.

Hinz, N.H., Faulds, J.E., and Oppliger, G.L., 2008, Structural controls of Lee Hot Springs, southern Churchill County, western Nevada: A small pull-apart in the dextral shear zone of the Walker Lane: Geothermal Resources Council Transactions, v. 32, p. 285–290.

Hinz, N.H., Faulds, J.E., and Henry, C.D., 2009, Tertiary volcanic stratigraphy and paleotopography of the Diamond and Fort Sage Mountains: Constraining slip along the Honey Lake fault zone in the northern Walker Lane, northeastern California and western Nevada: Geological Society of America Special Paper 447, no. 07, p. 1-32, doi: 10.1130/2009.2447(07).

Hinz, N.H., Faulds, J.E., Moeck, I., Bell, J.W., and Oldow, J.S., 2010, Structural controls of three blind geothermal resources at the Hawthorne Ammunition Depot, west-central Nevada: Geothermal Resources Council Transactions, v. 34, p. 785–790.

Hinz, N.H., Faulds, J.E., Stroup, C., 2011, Stratigraphic and structural framework of the Reese River geothermal area, Lander County, Nevada: A new conceptual structural model: Geothermal Resources Council Transactions, v. 35, p. 827–832.

Ichinose, G.A., Smith, K.D., and Anderson, J.G., 1998, Moment Tensor Solutions of the 1994 to 1996 Double Spring Flat, Nevada, Earthquake Sequence and Implications for Local Tectonic Models: Bulletin of the Seismological Society of America, v. 88, no. 6, p. 1363–1378.

Ichinose, G. A., Anderson, J. G., Smith, K. D., and Zeng, Y., 2003, Source parameters of eastern California and western Nevada earthquakes from regional moment tensor inversion: Bulletin of the Seismological Society of America, v. 93, p. 61-84.

Jaeger, J.C. and Cook, N.G.W, 1979, Fundamentals of rock mechanics, Third edition, New York: Chapman and Hall, p. 28-30.

Kinsella, M.E., 2010, The Fox Range, northwest Nevada; displaced fragment along an early Cretaceous dextral strike-slip fault [M.S. Thesis]: University of Georgia, Athens.

Kratt, C., Sladek, C., and Coolbaugh, M., 2010, Boom and bust with the latest 2 m temperature surveys: Dead Horse Wells, Hawthorne Army Depot, Terraced Hills, and other areas in Nevada: Geothermal Resources Council Transactions, v. 34, p. 567-574.

Kreemer, C., Blewitt, G., and Hammond, W.C., 2009, Geodetic constraints on contemporary deformation in the northern Walker Lane : 2. Velocity and strain rate tensor analysis: Geological Society of America Special Paper 447, p. 17–31, doi: 10.1130/2009.2447(02).

Lachmar, T.E., Freeman, T.G., Wood, T.R., Shervais, J.W., and Nielson, D.L., 2012, Chemistry and thermometry of geothermal water from Mountain Home Test Well MH-2B S: Preliminary Results: Geothermal Resources Council Transactions, v. 36, p. 689–692.

Larsen, P.-H., 1988, Relay structures in a Lower Permian basement-involved extension system, East Greenland: Journal of Structural Geology, v. 10, p. 3–8.

Louie, J.N., Pullammanappallil, S., Faulds, J.E., Eisses, A., Kell, A., Frary, R., and Kent, G., 2011, Astor Pass seismic surveys preliminary report: 25 p.

Marrett, R., and Allmendinger, R.W., 1990, Kinematic analysis of fault-slip data: Journal of Structural Geology, v. 12, no. 8, p. 973–986.

Moeck, I., Kwiatek, G., and Zimmermann, G., 2009, Slip tendency analysis, fault reactivation potential and induced seismicity in a deep geothermal reservoir: Journal of Structural Geology, v. 31, no. 10, p. 1174–1182.

Morris, A., Ferrill, D.A., and Henderson, D.B., 1996, Slip-tendency analysis and fault reactivation: Geology, v. 24, no. 3, p. 275-278.

Newman, G.A., Gasperikova, E., Hoversten, G.M., and Wannamaker, P.E., 2008, Three-dimensional magnetotelluric characterization of the Coso geothermal field: Geothermics, v. 37, no. 4, p. 369–399.

Reeves, D.M., Pohll, G.M., Lyles, B., Faulds, J., Louie, J.N., Ehni, B., Kratt, C., Cooper, C., Parashar, R., Pullammanappallil, S., and Noel, D., 2012, Geothermal resource characterization and evaluation at Astor Pass , Nevada: Geothermal Resources Council Transactions, v. 36, p. 1371–1376.

Ressel, M. W., 1996, A transitional basaltic center in west-central Nevada: Petrochemistry and constraints on regional middle Miocene magmatism and tectonism [M.S. thesis]: University Nevada, Reno.

Rhodes, Greg T., 2011, Structural controls of the San Emidio geothermal system, Northwestern Nevada [M.S. Thesis], University of Nevada, Reno, 73 p.

Smith, W.H.F., and Wessel, P., 1990, Gridding with continuous curvature splines in tension: v. 55, no. 3, p. 293–305.

Stewart, J.H., 1988, Tectonics of the Walker Lane belt, western Great Basin: Mesozoic and Cenozoic deformation in a zone of shear, in Ernst, W. G., ed., Metamorphism and crustal evolution of the western United States: Prentice Hall, Englewood Cliffs, New Jersey, p. 681-713.

Thatcher, W., 2003, GPS constraints on the kinematics of continental deformation: International Geology Review, v. 45, p. 191–212.

Trexler, J.H., Cashman, P.H., Henry, C.D., Muntean, T., Schwartz, K., Tenbrink, A., Faulds, J.E., Perkins, M., and Kelly, T., 2000, Neogene basins in western Nevada document the tectonic history of the Sierra Nevada – Basin and Range transition zone for the last 12 Ma: Geological Society of America Field Guide 2, p. 97–116.

Vice, G.S., J.E. Faulds, W.J. Ehni, and M.F. Coolbaugh, 2007, Structural controls of a blind geothermal system in Northern Pyramid Lake Area, Northwestern Nevada: Geothermal Resources Council Transactions, v. 31, p. 133-137.

Vice, G.S., 2008, Structural controls of the Astor Pass-Terraced Hills geothermal system in a region of strain transfer in the western Great Basin, northwestern Nevada [M.S. thesis]: University of Nevada, Reno, 114 p.

Wesnousky, S.G., 2005, Active faulting in the Walker Lane: Tectonics, v. 24, no. 3, p. 1–35, doi: 10.1029/2004TC001645.

Zoback, M.D., Moos, D., Mastin, L., and Anderson, R.N., 1985, Well bore breakouts and in situ stress: Journal of Geophysical Research, v. 90, p. 5523.

Zoback, M.D., Barton, C.A., Brudy, M., Castillo, D.A., Finkbeiner, T., Grollimund, B.R., Moos, D.B., Peska, P., Ward, C.D., and Wiprut, D.J., 2003, Determination of stress orientation and magnitude in deep wells: International Journal of Rock Mechanics and Mining Sciences, v. 40, p. 1049–1076.

Zoback, M.D., 2007, Reservoir geomechanics: Earth stress and rock mechanics applied to exploration, production and wellbore stability: Cambridge Press, 449 p.

Zuo, G., and Fan, G., 2011, A study of volcanic rocks identification by seismic methods in Subei Basin, Jiangsu Province, China: AAPG Search and Discovery Article, no. 10352, p. 1-6.

Appendix A – Raw and Interpreted 2D Seismic profiles

The seismic reflection data were first collected in 2006 by ZAPATA-Blackhawk using a minivibe with short offset receivers, producing five lines of data with a fairly shallow depth of usable resolution. In May 2010, the 4th line of this dataset was recollected along with an additional 11 lines of 2d seismic-reflection-refraction using three heavy (60,000 lb.) vibrator sources with over 200 channels by Optim Inc. All 16 of the 2d lines were then processed or reprocessed by Optim using advanced seismic analysis, including first-arrival velocity optimization and pre-stack depth migration. The seismic reflection data collected in 2010 were shot with long offsets, optimized to image steeply dipping structures at the lower predicted reservoir depths. All scales on the seismic lines are in feet. The vertical scale for each profile is relative to a datum of ~4,600 feet above sea level. See map below for the location of each seismic reflection line. Green seismic lines were used as cross sections for 3D model generation, whereas blue lines were only used in fault and stratigraphy interpretation.

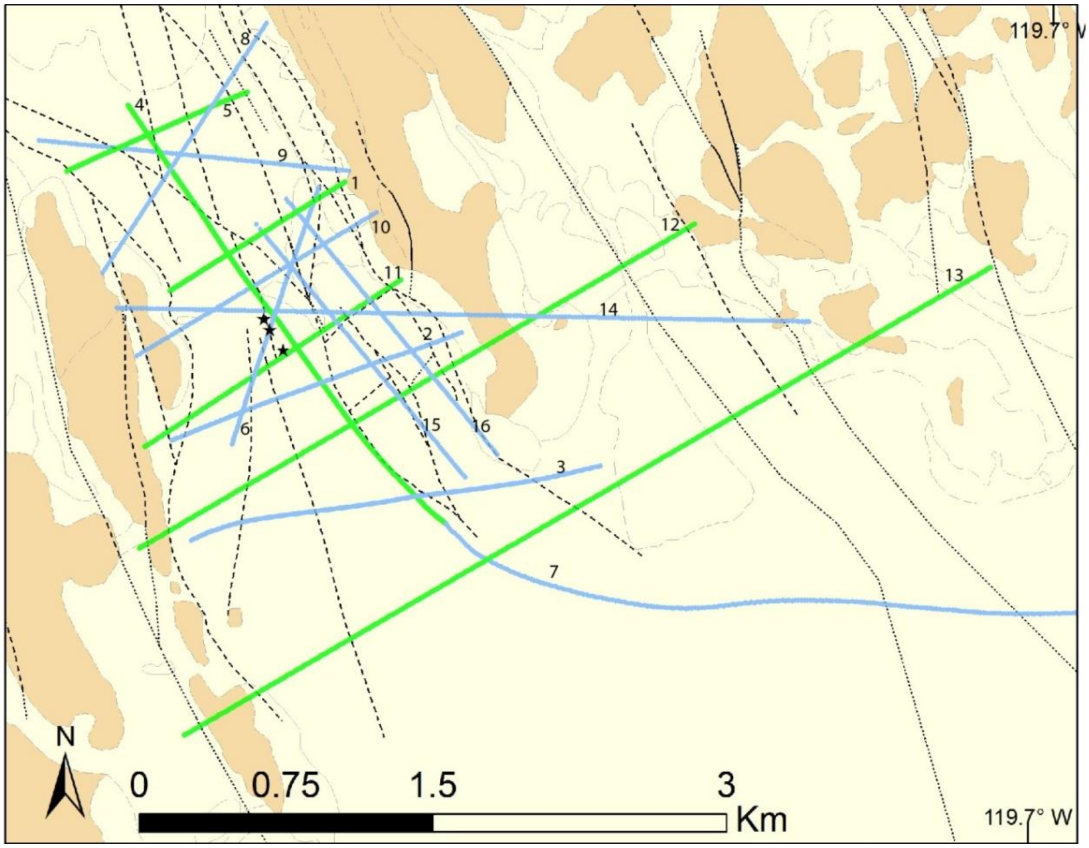

Figure A1. Map of all 16 2D seismic reflection profiles. Green and blue profiles were used for fault and stratigraphic interpretation. Green profiles were additionally used as cross sections for generation of the 3D model.

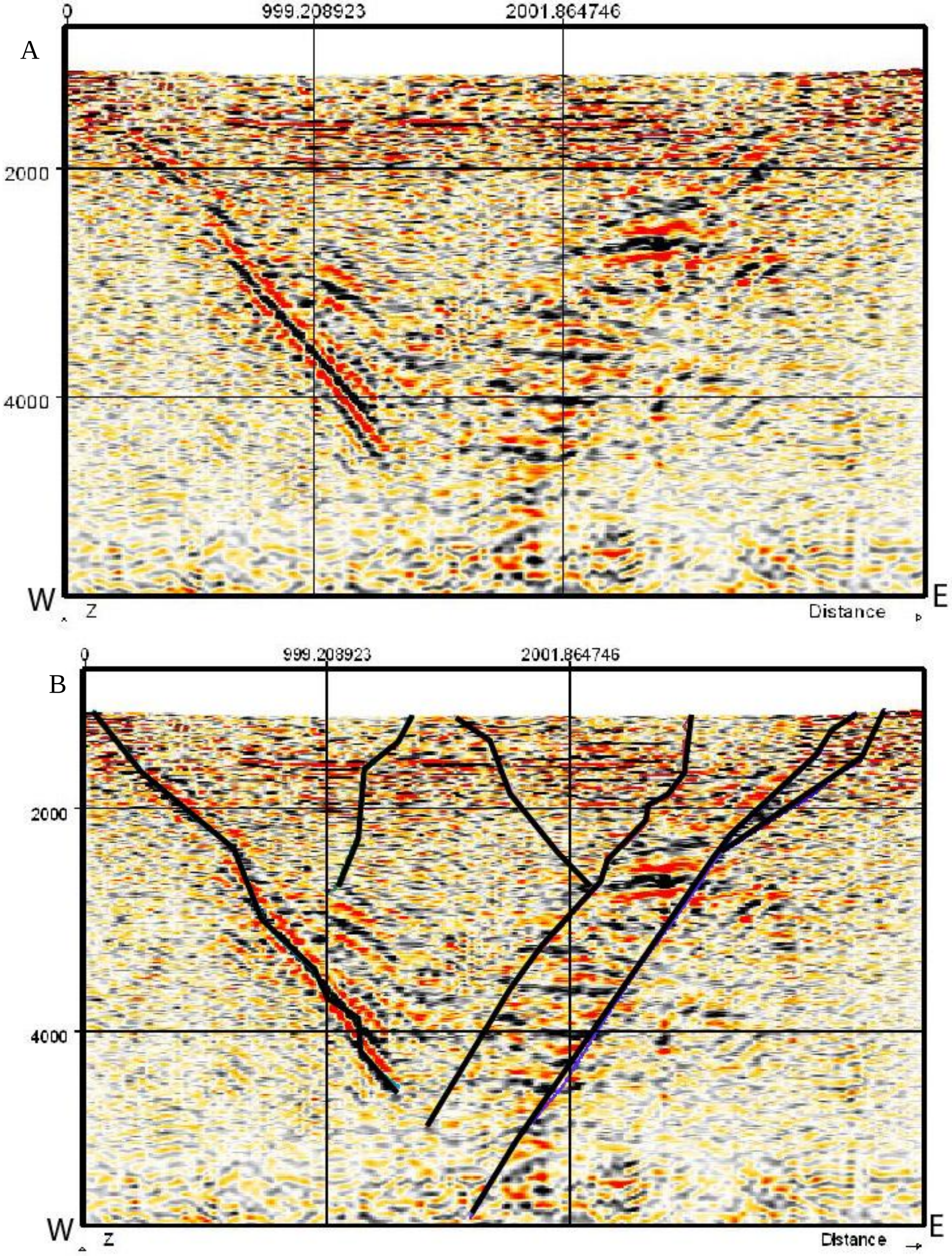

Figure A2. Seismic profile 1, used in cross section and 3D model. A. Uninterpreted. B. Initial interpretations in color with final interpretations in black.

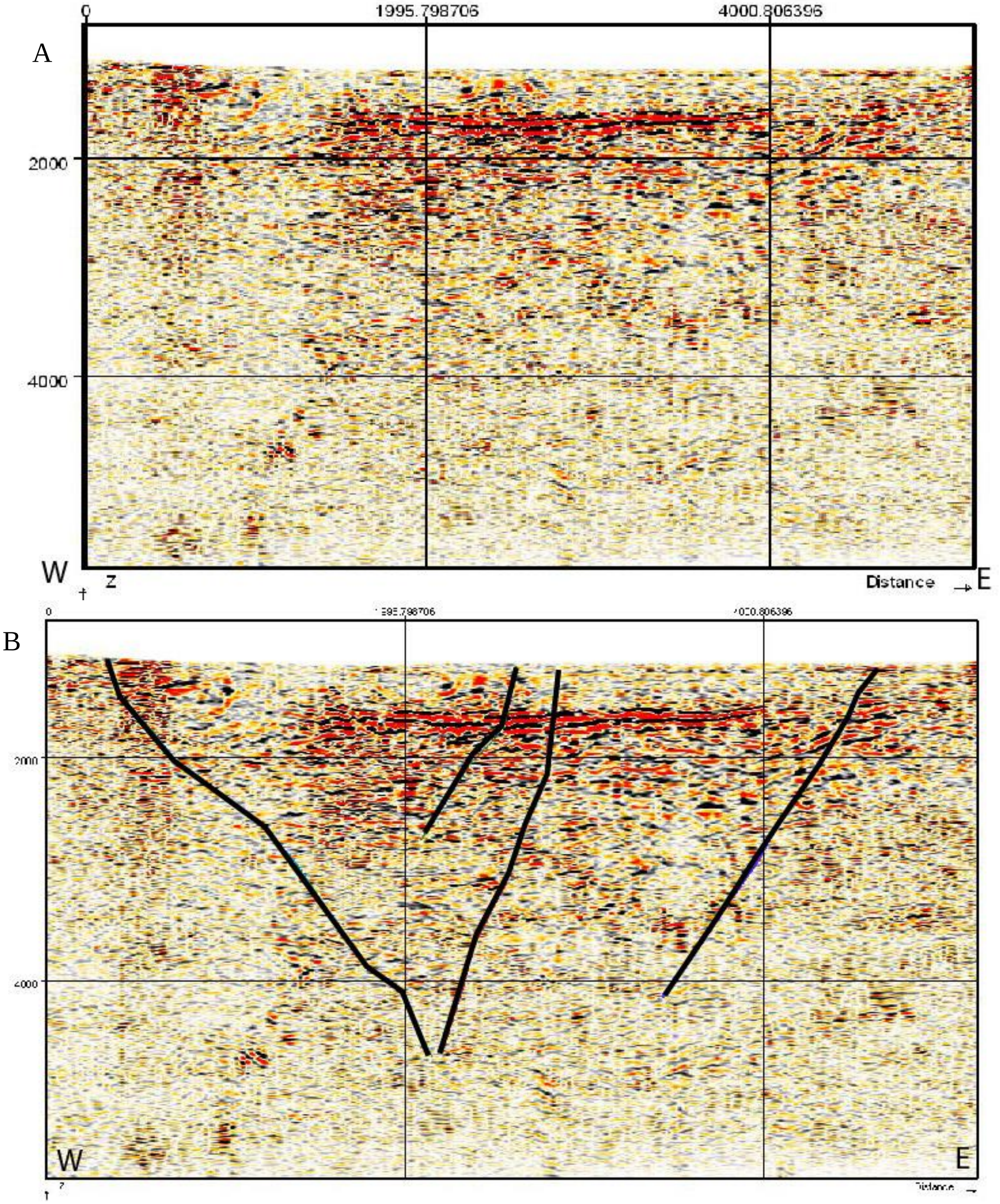

Figure A3 Seismic profile 2. A. Uninterpreted. B. Final interpretations in black.

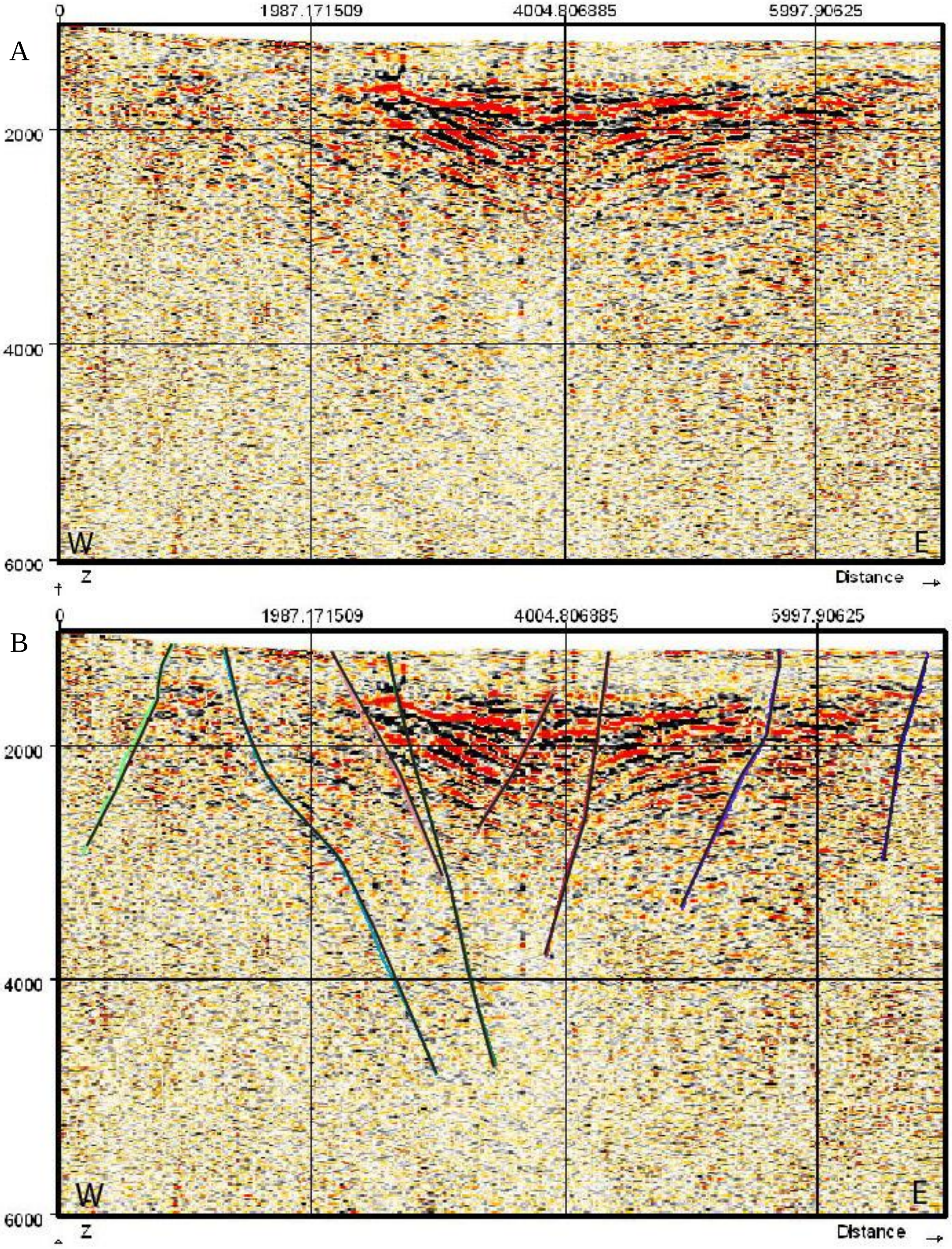

Figure A4. Seismic profile 3. A. Uninterpreted. B. Initial interpretation in color with final interpretations in black.

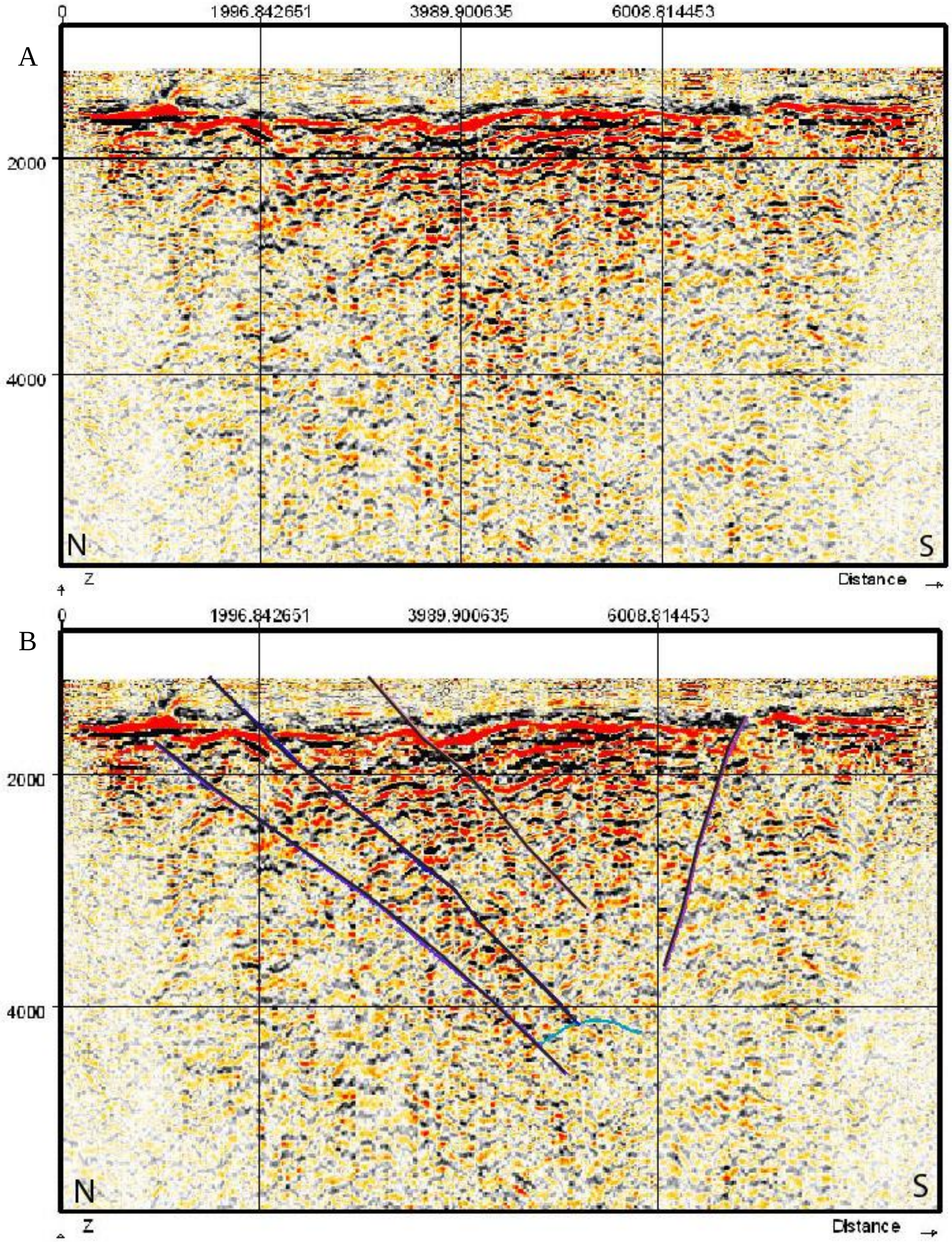

Figure A5. Seismic profile 4 used as cross section in 3D model as the north-south connecting profile. A. Uninterpreted. B. Initial interpretations in color with final interpretations in black.

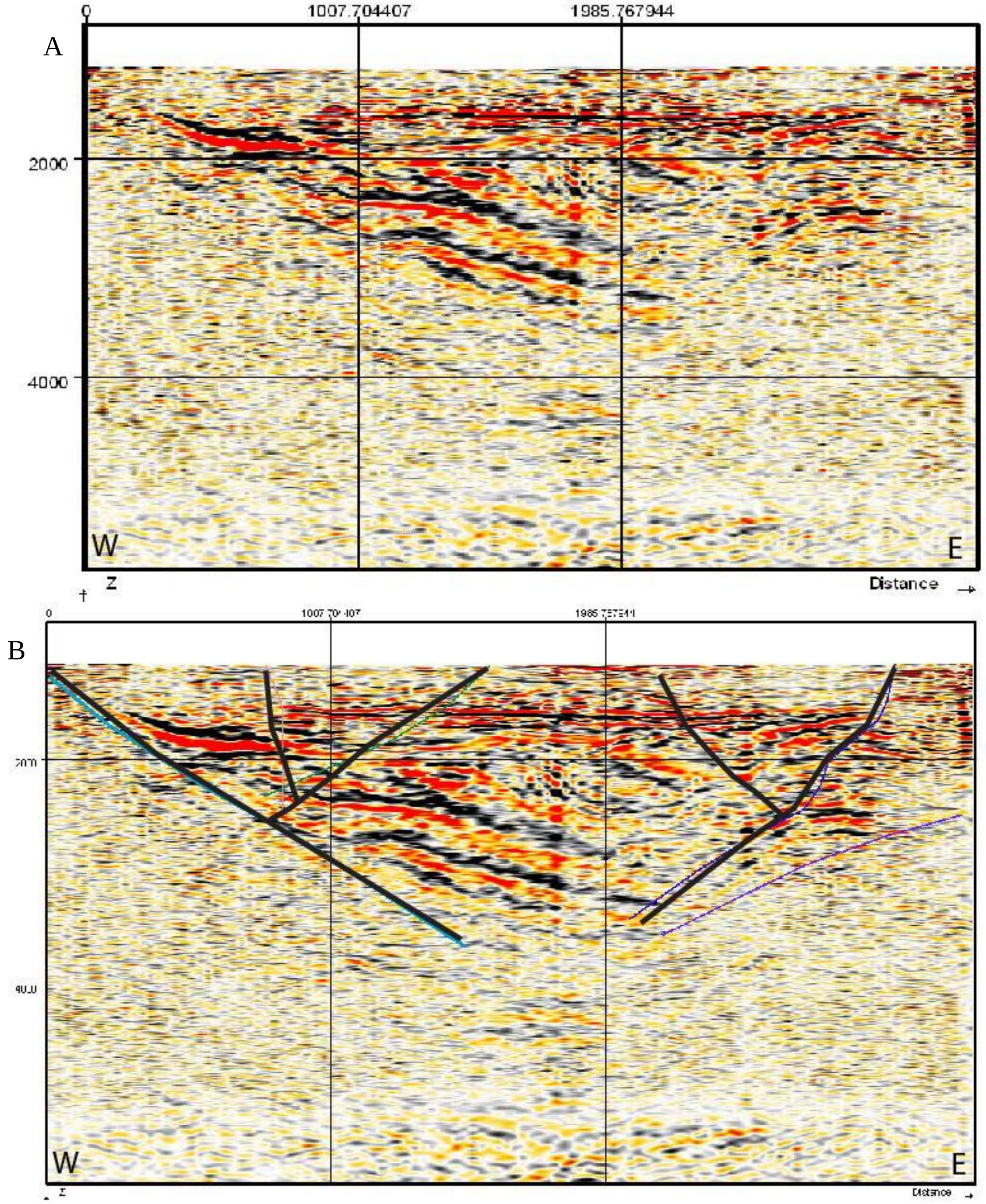

Figure A6. Seismic profile 5 used as cross section for 3D model. A. Uninterpreted. B. Initial interpretations in color with final interpretations in black.

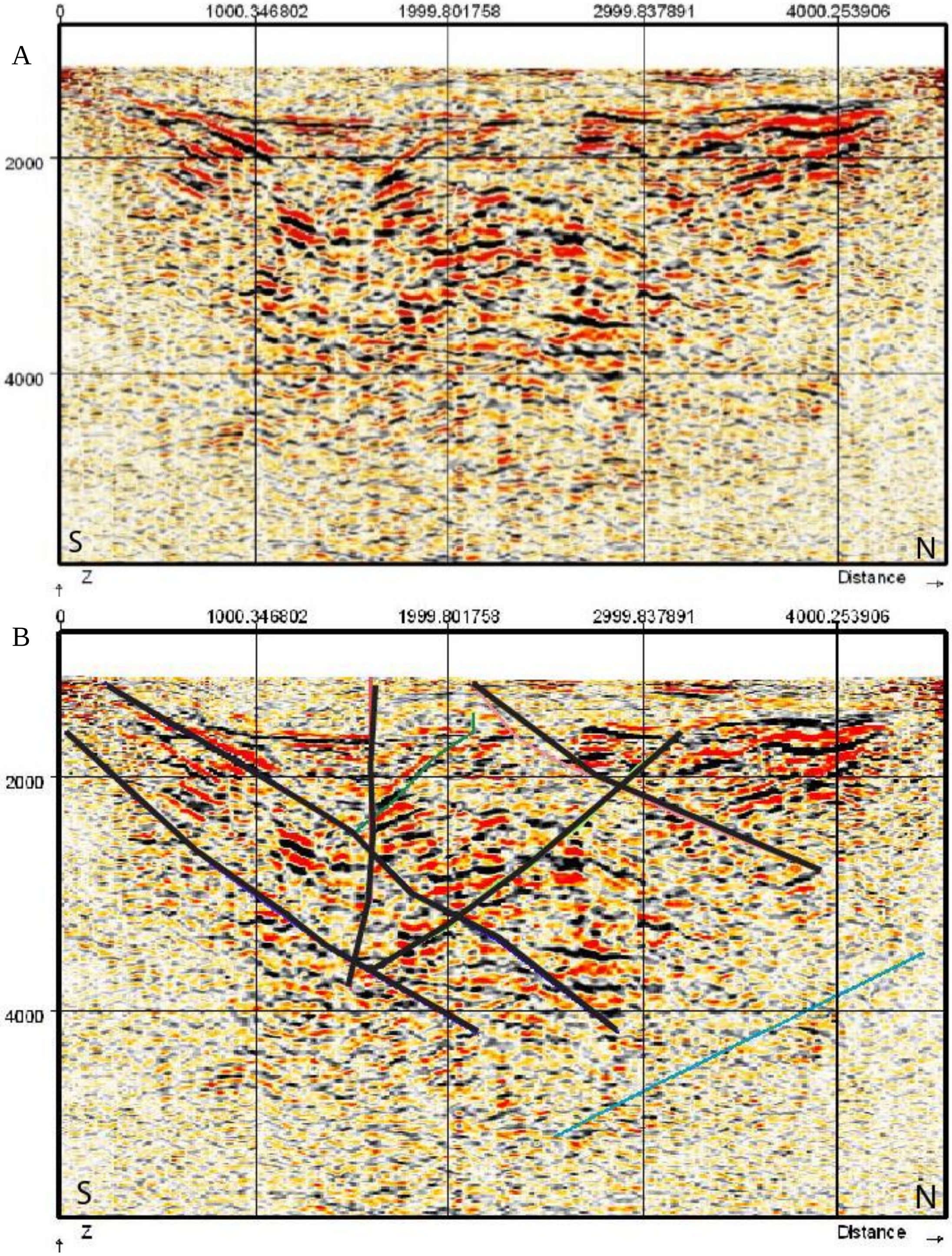

Figure A7. Seismic profile 6. A. Uninterpreted. B. Initial interpretations in color with final interpretations in black.

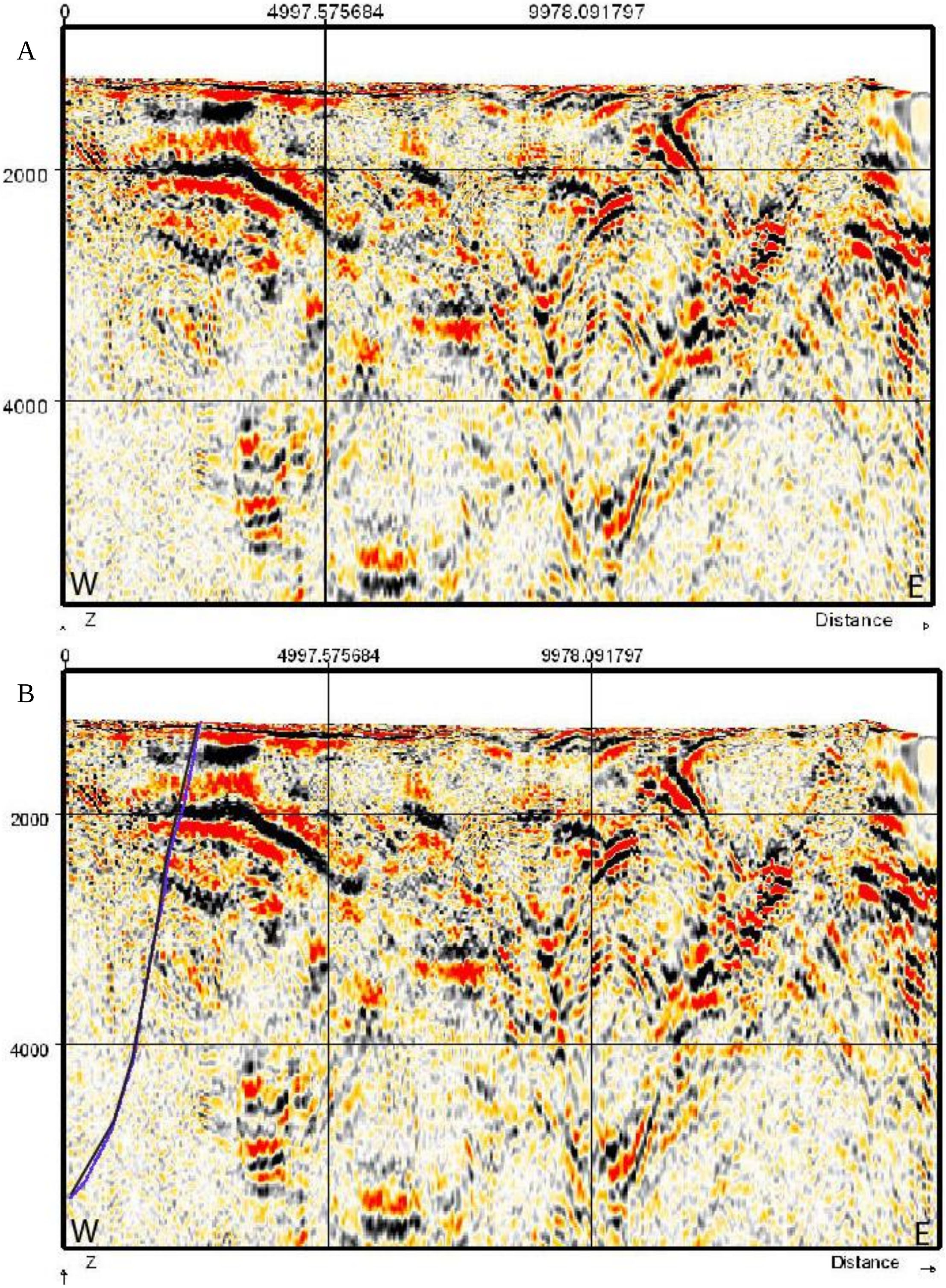

Figure A8. Seismic profile 7. A. Uninterpreted. B. Initial interpretations in color with final interpretations in black.

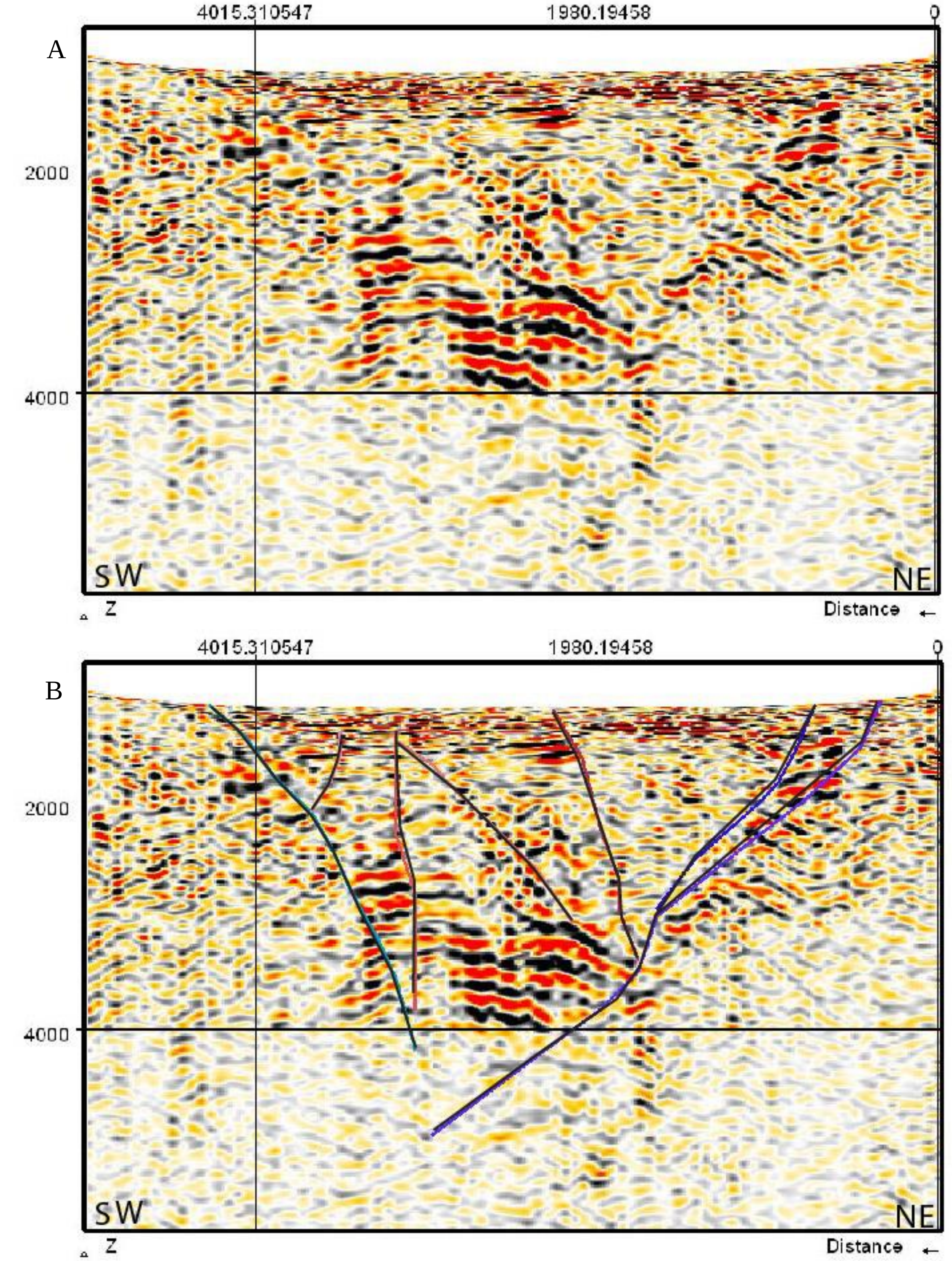

Figure A9. Seismic profile 8. A. Uninterpreted. B. Initial interpretations in color with latest interpretations in black.

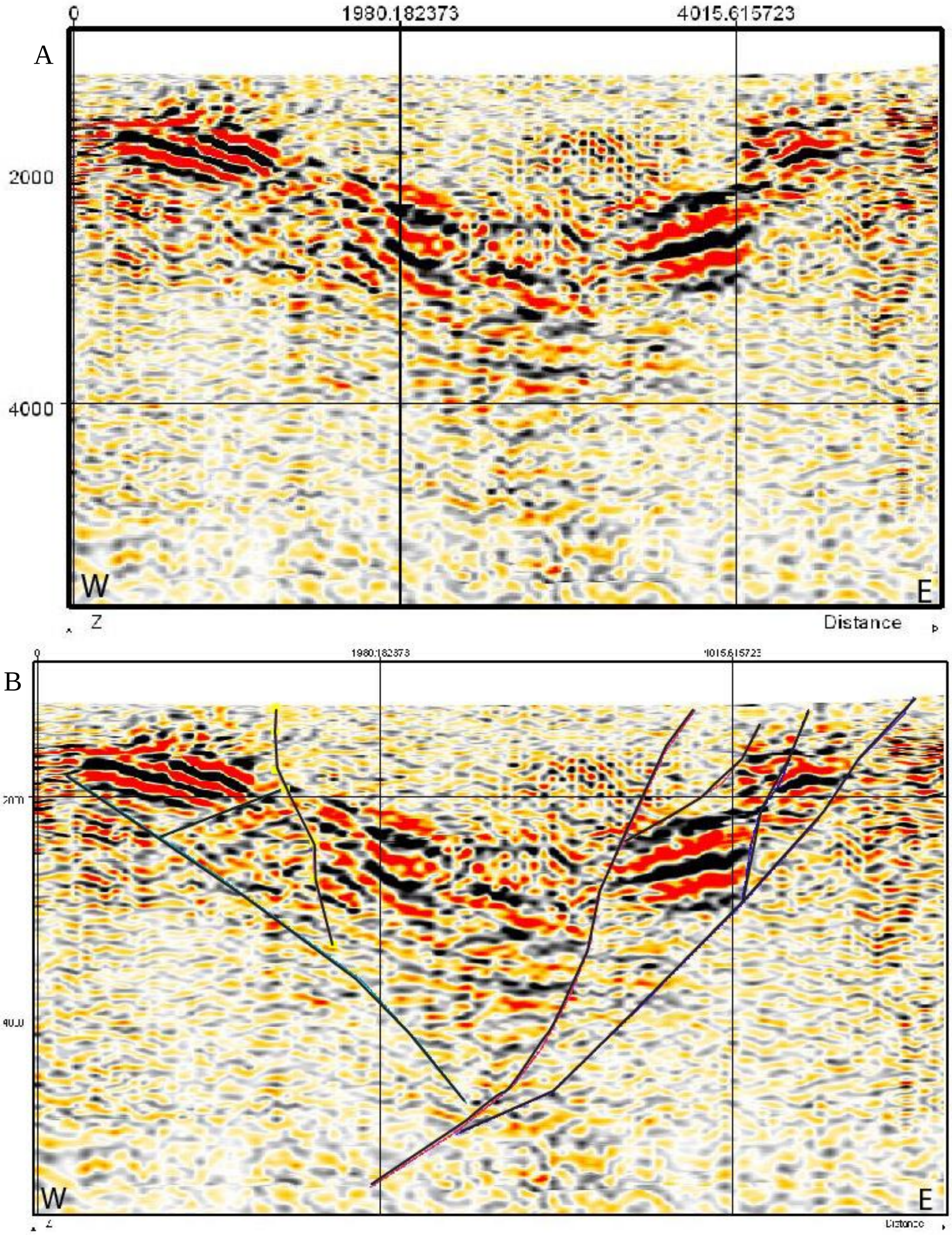

Figure A10. Seismic profile 9. A. Uninterpreted. B. Initial interpretations in color with latest interpretations in black.

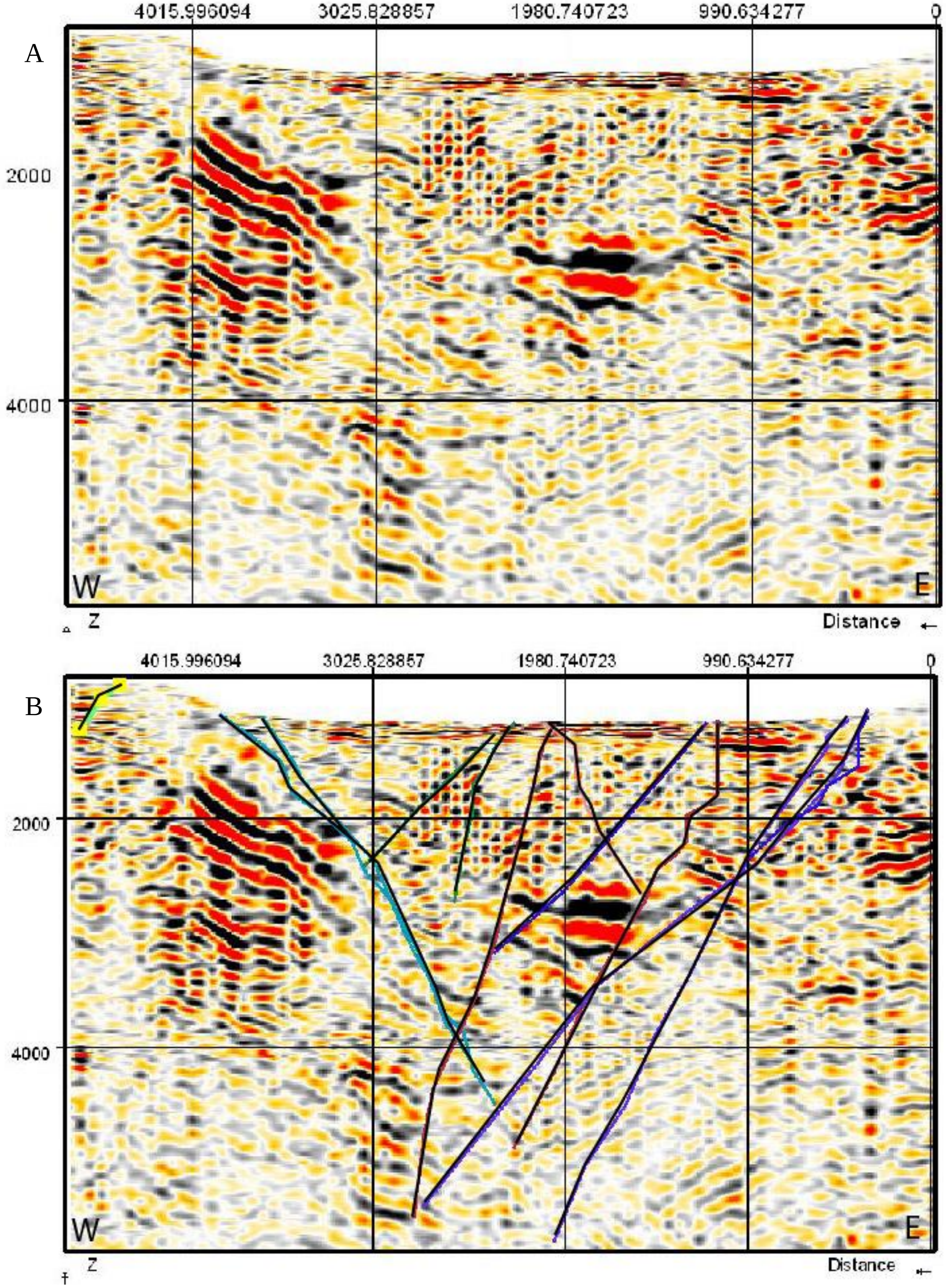

Figure A11. Seismic profile 10. A. Uninterpreted. B. Initial interpretations in color, with final interpretations in black.

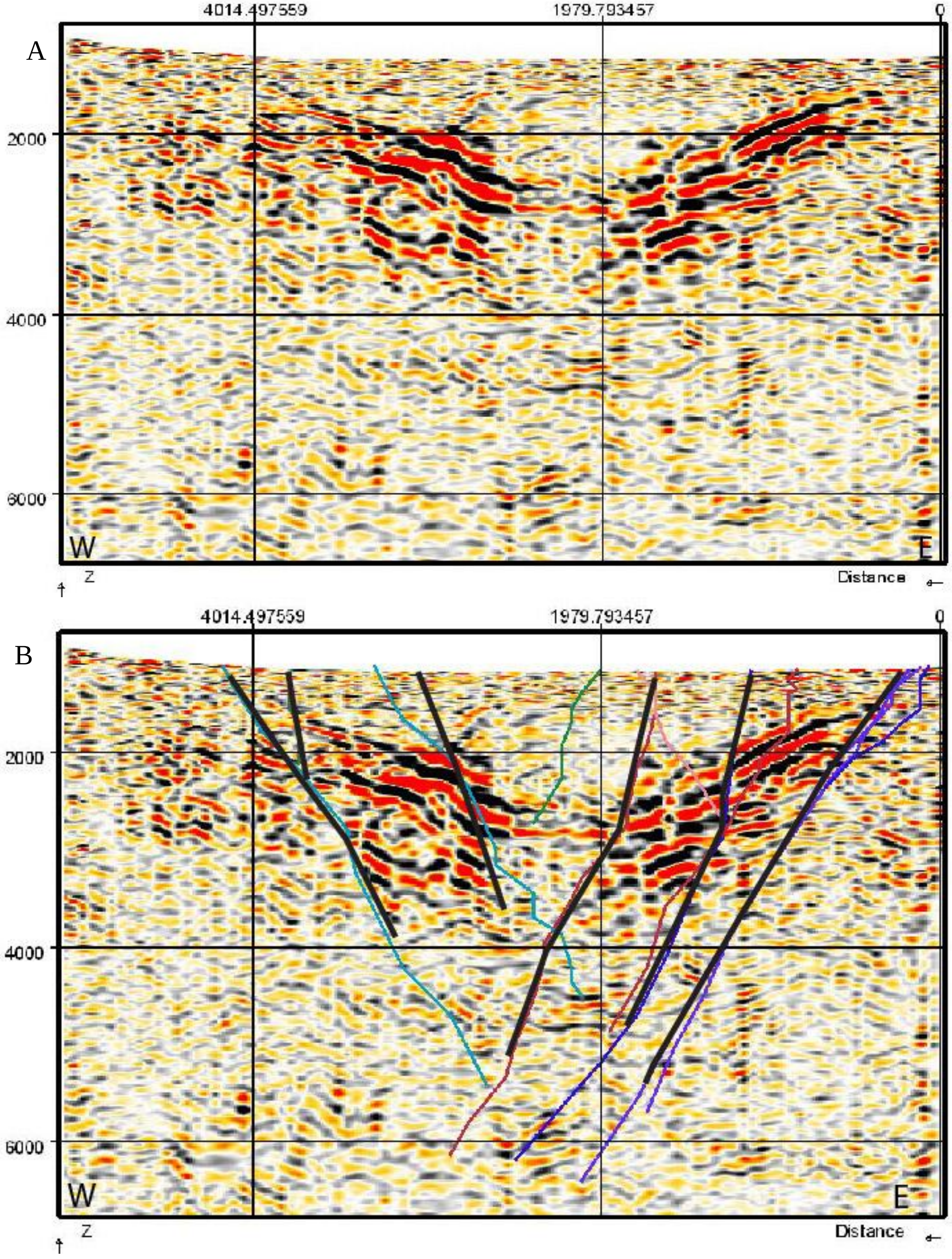

Figure A12. Profile 11, used as cross section in 3D model. A. Uninterpreted. B. Iinitial interpretations in color with final interpretations in black.

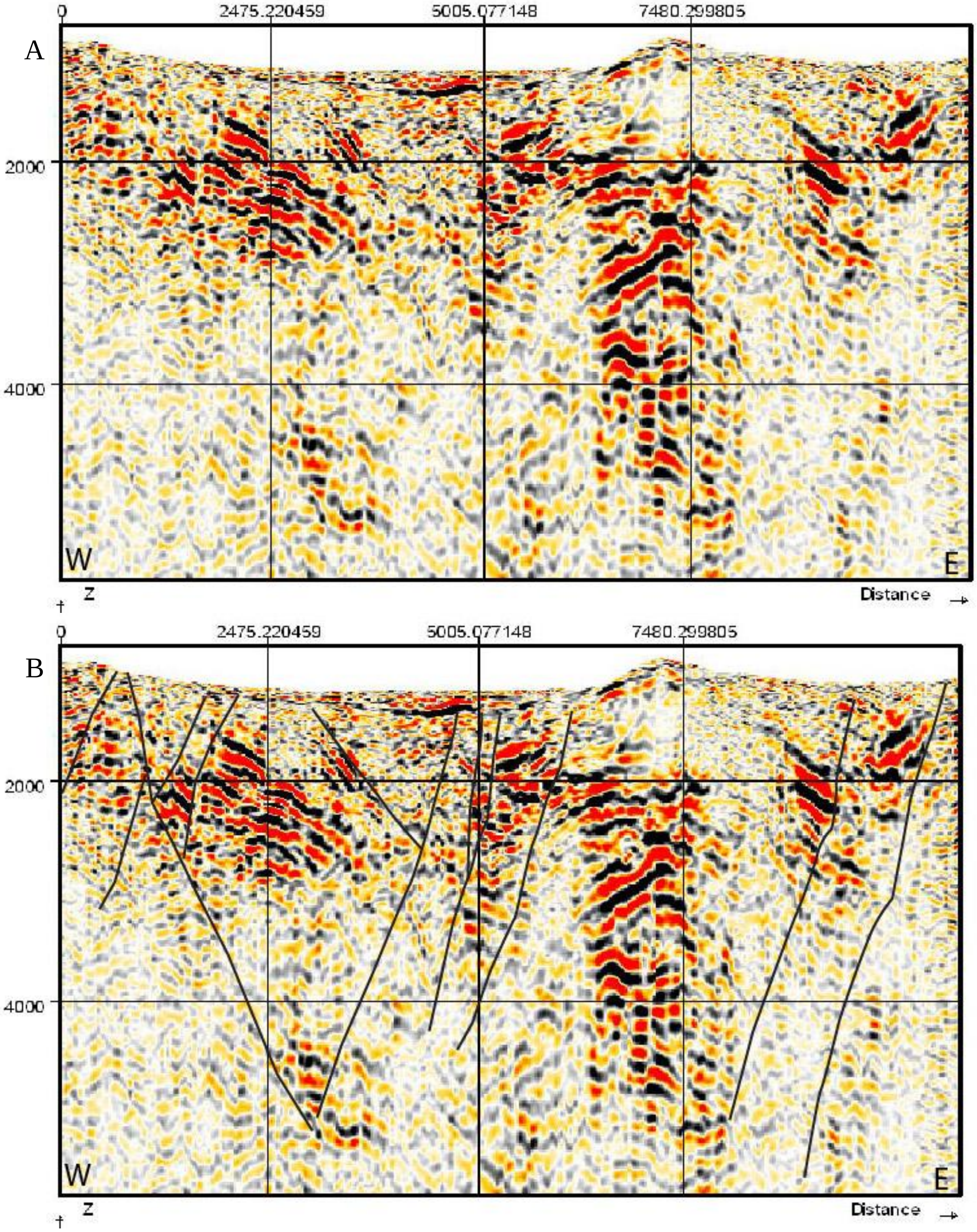

Figure A13. Seismic profile 12, used in cross section and 3D model. A. Uninterpreted. B. Initial interpretations in color with final interpretations in black.

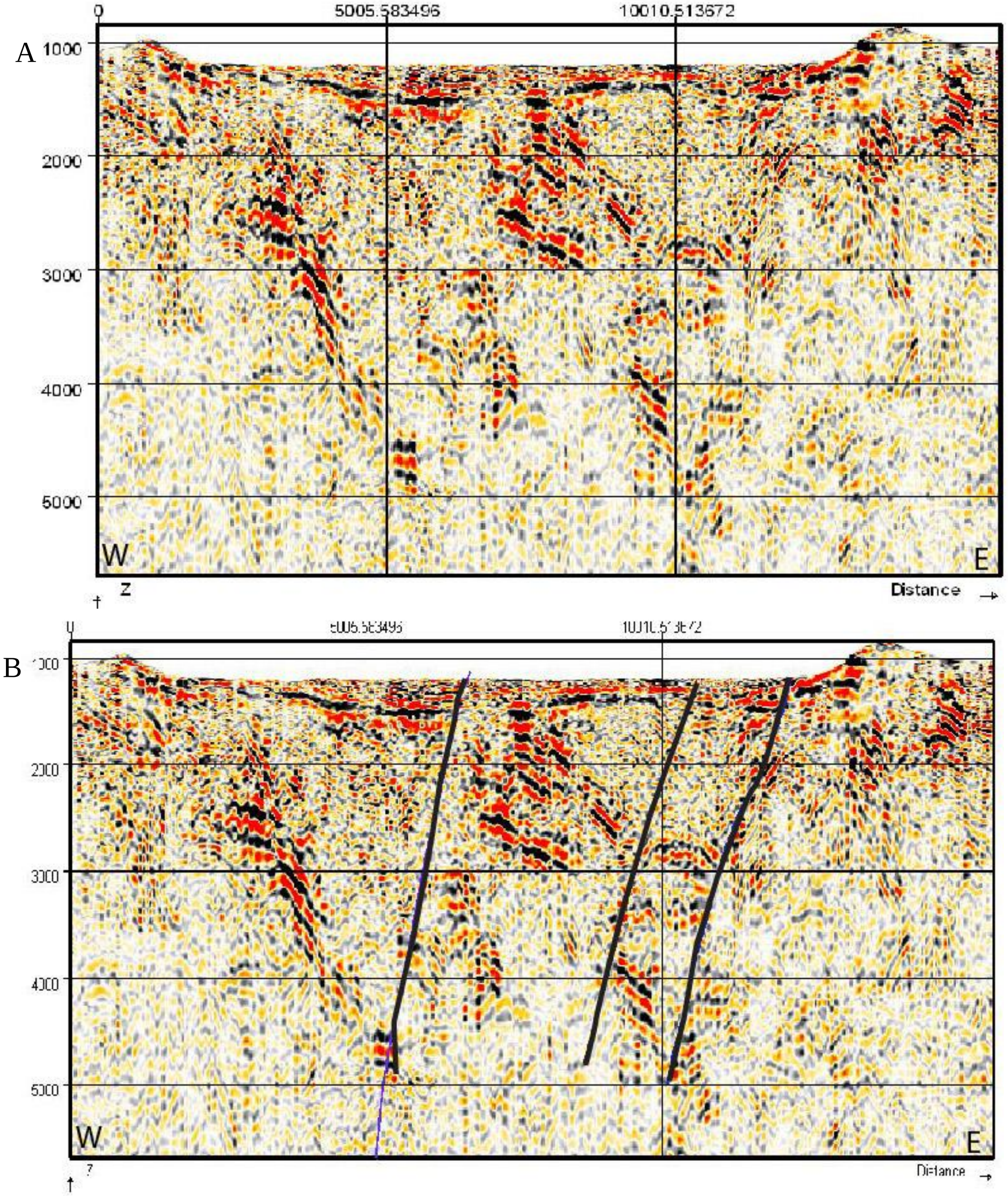

Figure A14. Seismic profile 13, used in cross section and 3D model as southern-most profile. A. Uninterpreted. B. Initial interpretations in color with final interpretations in black.

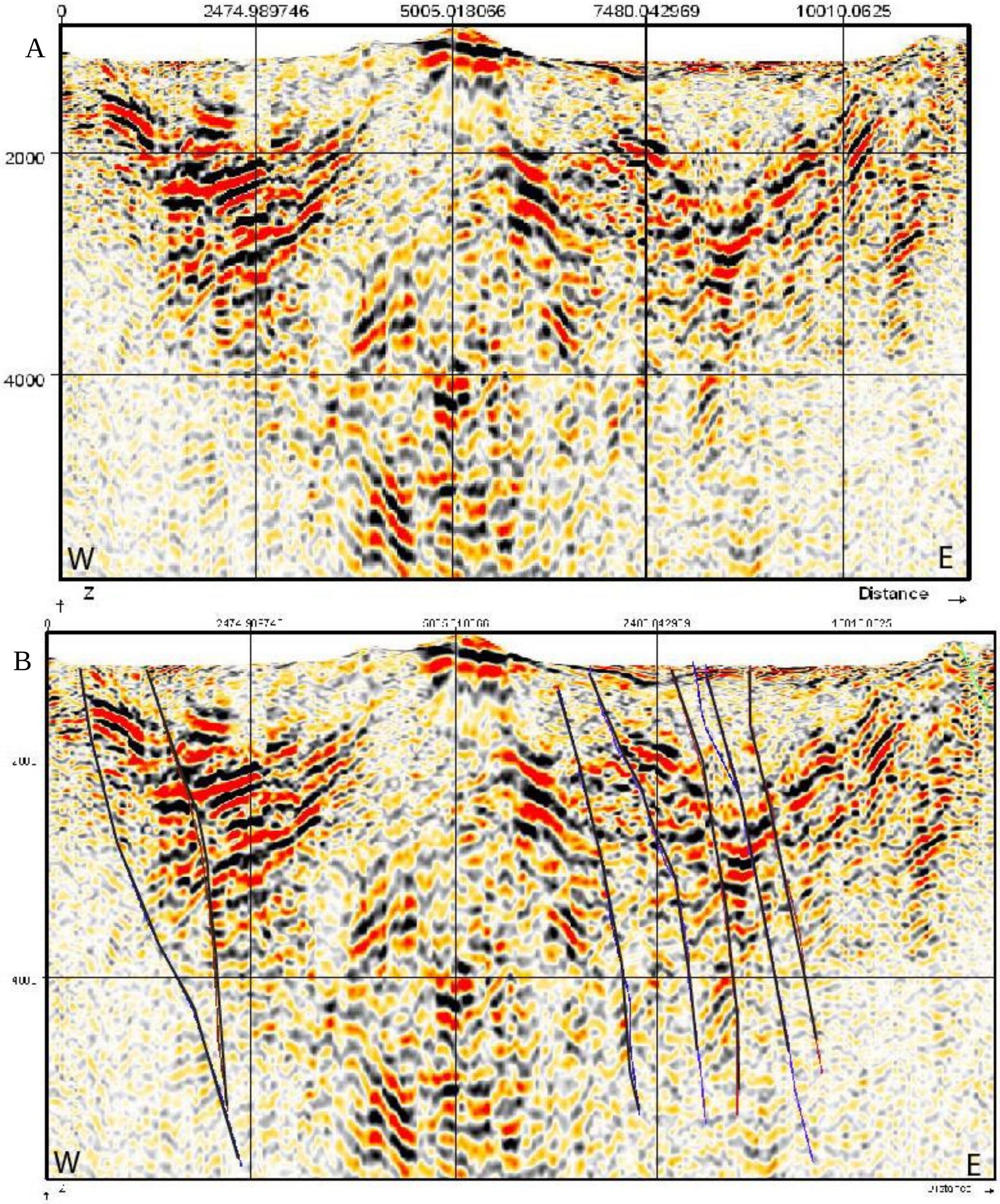

Figure A15. Seismic profile 14. A. Uninterpreted. B. Initial interpretations in color with final interpretations in black.

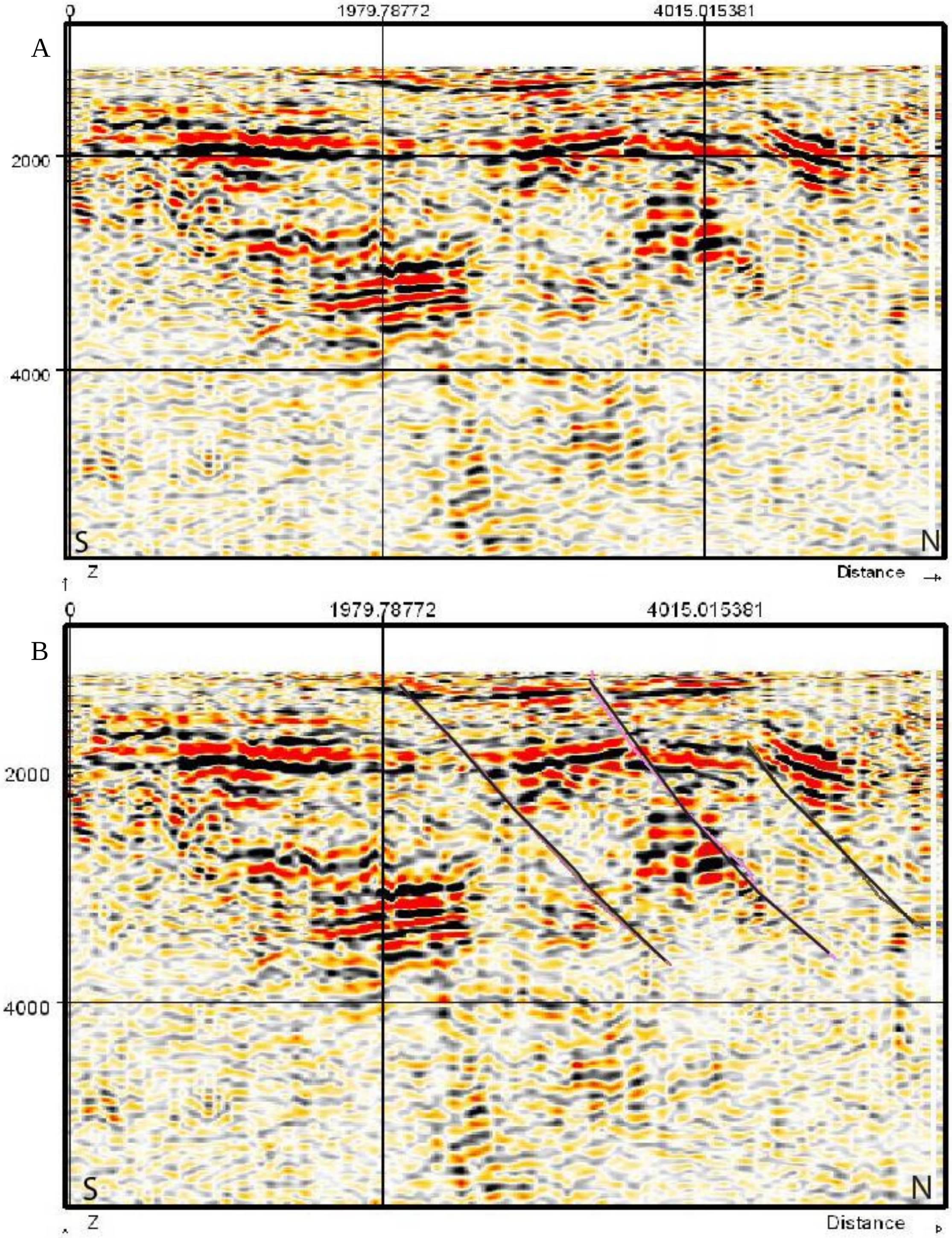

Figure A16. Seismic profile 15. A. Uninterpreted. B. Initial interpretations in color with final interpretations in black.

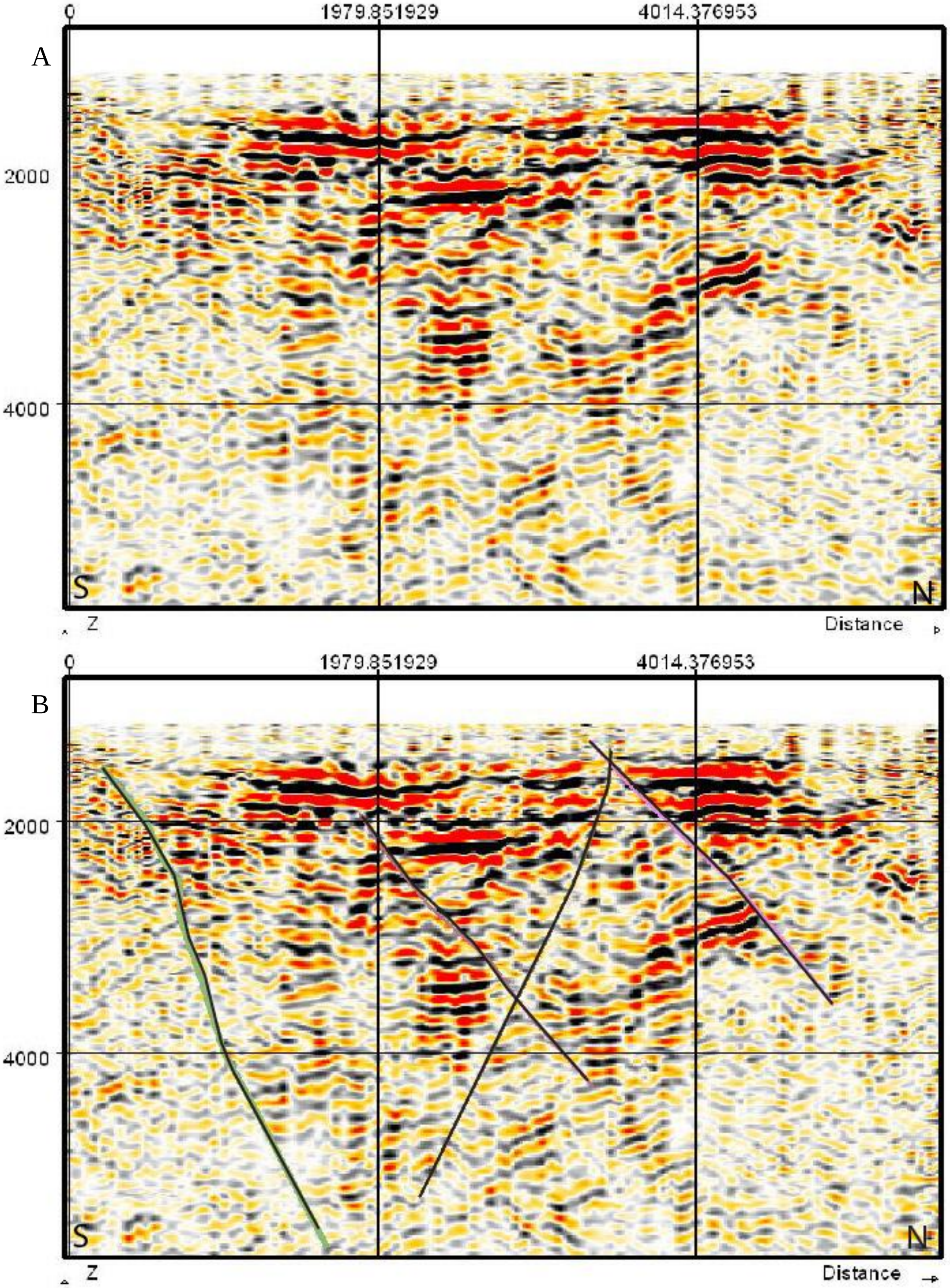

Figure A17. Seismic profile 16. A. Uninterpreted. B. Initial interpretations in color with final interpretations in black.

Appendix B

APS-2 Cuttings Analysis

Interval (feet)	Rock Type (Abbreviation for unit name where applicable, see Figure 4 and 6)	Description
10-20	**Q Silty Sandstone**	Poorly sorted sand and silt, some pebbles up to 1cm, mostly mafic volcanics with one large 1cm granitic pebble, abundant mica (muscovite), 3-5% plagioclase and trace quartz.
20 - 30	**Q Siltstone**	very light gray, well sorted, 80% silt, 20% sand, biotite and muscovite microcrysts, 8% sub mm quartz, 3% mafic sands up to 2mm.
30 - 50	**Q Sandy Siltstone**	Very similar to 20ft, 10% quartz, muscovite, silt has 5% shells, see picture, green mica at 40 ft, 1% hornblende (long tabular, glassy, black), trace reddish brown oxidation.
50	**Q Silty Sandstone**	Similar to 30-40, more mafic pebbles (basalt), quartz phenocrysts up to 1mm, significant oxide/staining orange brown, similar mica as 30-40 ft, no shells.
60-90	**Q Sandstone**	Quartz, fine to medium grain, subangular to subrounded, well sorted, slight oxidation, biotite and muscovite, sand up to 2mm, predominately 1mm.

90-210	**Q Silty Sandstone**	Weakly lithified, poorly sorted, abundant shells at 150-180 ft, light brown, 2-3% mica (biotite and muscovite), 4% quartz, predominately <1mm, up to 3mm
210-240	**Q Coarse Sandstone**	Moderately sorted, quartz dominated, 2mm up to 4mm, 3-5% plagioclase, 3% mafics up to 4mm, trace muscovite, light grayish brown.
240-270	**Q Silty Sandstone**	Quartz, 10%, up to 3mm, pumice, shells, epidote, biotite and muscovite up to 3-4%, trace mafics, pyrite (1 crystal).
270-300	**Tc Conglomerate**	Chalcedony 25%, iron oxide staining, lapilli (black hair like internal structures), angular to rounded mafics up to 6mm mostly andesitic basalt, possible fault gouge, moderate amount of quartz fine sand.
300-360	**Tlpa Basaltic Andesite**	Dark gray to slight reddish brown, plagioclase phenocrysts up to 2mm, trace chalcedony, pyroxene, chalcedony vein coated with micas, mafics are angular to sub angular, sparse red orange to light orange oxidation, 330-360 higher 40% plagioclase altered, moderate iron oxide staining.
360-420	**Tlpa Basaltic Andesite**	Altered, medium reddish gray, numerous (25%) altered plagioclase phenocrysts up to 3mm, trace pyroxene.
420-450	**Chalcedony**	Clay altered plagioclase microcrysts, epidote, pyroxene, quartz, altered plagioclase, sizes are all ½ to 1 mm occasionally up to 3mm, weakly welded, trace oxidation.

450-480	**Tlpp Andesite**	Reddish andesite, 10% altered plagioclase phenocrysts to 1mm, 5% quartz up to 4mm, similar to 420 ft, poorly sorted, also trace non-altered plagioclase.
480-510	**Tlpp Basaltic Andesite**	Pale purplish gray, medium gray, medium brown sparsely porphyritic andesite, 2% pyroxene up to 2mm, groundmass contains quartz, altered and unaltered plagioclase up to 1mm, and silica veins.
510-540	**Tlpp Basaltic Andesite**	Medium gray aphanitic andesite, 5% 1-2mm phenocrysts of plagioclase, 5% pyroxene, and some altered plagioclase.
540-630	**Ts Volcaniclastics**	Volcanic sandstone, orange brown to pale purple gray, highly variable color, very fine to fine grained, sub-rounded to angular, high clay % even after washing, grains composed of mafic volcanics, quartz, plagioclase, pyroxene, and possible tuff, 570-600 ft more purple gray dominant clasts, with microcrysts of green, luster mineral.
600-630	**Ts Volcaniclastics**	Basalt, some tuffaecous material, pyroxene, biotite medium gray to pale purple-gray, very few chips larger than 3mm, larger chips commonly purple-gray with clay altered crystals, along with 1-2% green crystal seen above, some iron oxide staining.

630-660	**Ts Volcaniclastics**	25% basaltic andesite, orange to red to purple-gray volcanics, andesite is medium gray with some iron oxides staining, 5% dark green phenocrysts (in andesite and clastics), lustrous, commonly tabular, also isolated 3% quartz crystals up to 2mm, clastics show significant clay alteration and veining and 1% green mineral, possible epidote.
660-690	**Ts Volcaniclastics**	Gravelly sand, sub-angular to rounded pebbles of andesite up to 5mm, mostly aphanitic, sand has andesite, rhyolite, clays, quartz grains, sparse staining, very fine to medium grained.
690-840	**NO CHIPS**	NO CHIPS
840-870	**Tri Rhyolite**	Light greenish gray to off white, 4% muscovite/biotite up to 1mm, 50% medium gray vitreous chips (rhyolitic vitrophyre), up to 4mm, 5% muscovite, no reaction to HCl.
870-900	**Tri Rhyolite**	Off white to light greenish gray, 4-6% mica up to 2mm (probable biotite), 5% quartz to 3mm, 20% gray vitrophyre similar to 840-870 ft with chips up to 4mm.
900-960	**Tri Rhyolite**	Some clay (15%) after washing, pale gray, 8% muscovite 1mm or smaller, 4% quartz, trace mafics <1mm.
960-1080	**Tri Rhyolite -**	Light pale gray, 5% mica, 5% quartz, trace pyrite <1mm (mostly from 1020-1050), numerous silica veins and coating from 1000-1080 ft.
1080 to 2000	**NO CHIPS**	NO CHIPS

2000-2140	**Tlpp Basaltic Andesite**	Aphanitic medium gray to slight red gray at 2200, trace black phenocrysts, also sparse chips of rhyolite or tuff, numerous silica veins up to 1mm wide from 2000-2100, trace metallic mineral coating, trace iron oxide staining 2140-4170.
2140-2260	**Tlpp Andesite**	Greenish gray to reddish purple-gray, andesite aphanitic to sparsely porphyritic, 5% plagioclase up to 3mm, blocky to tabular, secondary silica growth on some andesite, pyrite by 2200 ft, trace free quartz crystals up to 2mm.
2260-2290	**Rhyolite/Dacite**	Pale greenish gray, aphanitic, 5-8% pyrite, some cubic, no micas, 5% overall quartz (vitrophyre), crystals mostly translucent to white with rare staining, including some bright purple, strong reaction HCl.
2260-2380	**Tlpp Basaltic Andesite**	Reddish medium gray, aphanitic, no red color from 2290-2380 ft. 10% calcite up to 2mm, possibly from broken up vein, up to 3mm chips, trace red-orange silicified fragments, trace pyrite.
2380-2410	**Tlpp Basaltic Andesite**	75% pale red scoriaceoius basalt, not stained, aphanitic, trace micas, trace quartz, possible fault, high angularity of smallest grains.
2410-2440	**Breccia**	Light gray to medium dark gray to reddish orange, scoriaceous material, some trace plagioclase microcrysts, 1-2% quartz crystals up to 2mm, sub-angular to subrounded overall.

2440-2470	**Breccia**	Fault breccia/ volcanic breccia light to medium gray, some red clasts, 1-2% clay filled fractures and voids, high clay/silt content during washing, groundmass vitreous, trace pyroxene (green hue), pyrite, and quartz.
2470-2560	**Ts Volcaniclastic**	Light brown to light gray, 8-10% black pyroxene phenocrysts up to 3-4mm, trace quartz.
2560- 2770	**Tlpp Basalt**	Medium gray, aphanitic, trace red clay similar to 2620 and 2650 ft, trace iron oxide staining in 2650, one large muscovite crystal, 5mm, at 2620 ft.
2680-2710	**Tlpp Basalt**	Medium gray, aphanitic, 4% quartz fragments up to 5mm, trace pyrite up to 1mm, trace oxide staining.
2710-2740	**Tlpp Basalt**	Aphanitic, 5% reddish volcanic that is highly porphyritic primarily plagioclase, pale green anhedral phenocrysts, trace orange iron oxidation, with a shiny deep red coating on it, drillers log notes it as Barite, again as in 2650 ft, secondary white/clear crystal with long strands, 1% red clay volcaniclastic.
2740-2770	**Tlpp Basalt**	Slightly porphyritic, lighter medium gray than 2710 ft, 2-3% thin silica veins ~1mm thick, trace flow foliation (2 possible examples), trace pyrite.
2770-2800	**Ts Volcaniclastics**	60% altered to a dull reddish color, 1% pumice very soft white chips, trace silica veins.

2800-2830	**Ts Pyramid Sequence Volcaniclastics**	Basalt clastics, dominant chips are slightly porphyritic, slightly greenish gray, phenocrysts of quartz and a darker slender phenocryst, also reddish orange almost grainy groundmass, sandstone chips with plagioclase, quartz, and darker possible pyroxene fragments in it, also 6% chalcedony (opaque siliceous chips), trace pyrite, trace chlorite (brighter light green?), and iron oxide staining.
2830-2860	**Ts Basalt/clastics**	Purple gray, red gray, greenish gray, highly variable, 3% pyrite, very little free silica/quartz, most chips appear to a mix of basalt and clastics, no phenocrysts, trace chalcedony, appears to be higher clay content even after washing.
2860-2890	**Tlpp Basalt/clastics**	Medium gray chips with high % pyroxene phenocrysts ~40%, 5% cryptocrystalline quartz, probable chalcedony, high clay content.
2890-2920	**Tlpp Basalt/clastics**	Similar to 2860 ft, but also has some larger reddish chips with silica filled voids.
2920-2950	**Tlpp Basalt**	20% clastics, aphanitic, medium gray, 20% reddish clay, clastics includes some very soft white pumice, some angular fragments of volcanics.
2950-3010	**Tlpp Basalt**	- Aphanitic to slightly porphyritic, medium dark gray, trace, also trace pyroxene, see description in 2710 ft, same bright red-orange mineral.
3010-3040	**Tlpp Basaltic Andesite**	Lighter green gray to red/purple gray, slightly porphyritic, 4% trace pyroxene, trace iron oxide staining, trace slickenside, trace

		pyrite
3040-3070	**Tlpp Basaltic Andesite**	Highly porphyritic, slightly bluish gray, 20% plagioclase at 1 mm scale, 5% blocky to slightly tabular chips medium green color, some more pale and look like secondary alteration, 1% shiny red to red-orange growth, mostly in small voids
3070-3100	**Tlpp Basaltic Andesite**	Slightly porphyritic, 4% pyroxene, also trace metallic mineral, 20% reddish soft clay/siltstone with green tabular phenocrysts, 15% red blocky phenocrysts, possibly altered.
3100-3190	**Tlpp Basalt/Clastics**	80% basalt, slightly porphyritic, pyroxene, plagioclase, both sub mm, dark gray, 20% clay is pinkish-red, fairly soft, with small intrusion of an even softer white material, trace orange-red oxide staining, clay % decreases with depth.
3190-3220	**Tlpp Basalt**	Slightly porphyritic,2-4% tabular plagioclase, some pyroxene, medium dark gray, some secondary silica growth, 3-4% reddish clay still evident, trace brownish-red chips with 30-40% plagioclase.

3220-3400	**Tlpp Basaltic Andesite**	Light to medium gray, some greenish gray, porphyritic, phenocrysts - plagioclase 8% ~1mm average, thin and tabular, one large chip of epidote (5-6mm), some reddish chips with higher plagioclase content to 20%, some altered to clay, 1% quartz veins up to 2-3mm thick, trace oxide staining, trace to 1% biotite/mica, free quartz and oxidation staining increase with depth.
3400-3430	**Tlpp Basaltic Andesite**	25% reddish chips, 75% medium gray, moderately porphyritic, plagioclase and pyroxene, 1% 2-3mm quartz veins, 5% light gray dacitic looking material with biotite, quartz, and plagioclase.
3430-3460	**Tlpp Basalt**	Slightly porphyritic, very small chips.
3460-3520	**Tlpp Basalt**	Medium gray brown, larger clasts show fragments of wide variety of volcanics, silica veins, some pyrite, free quartz.
3520-3550	**Tlpp Basalt**	Aphanitic, very glassy, plagioclase, small amounts of pyroxene and possibly hornblende, trace to 2% sandstone material.
3550-3610	**Tlpp Basaltic Andesite**	Slightly porphyritic, 4% >2mm plagioclase phenocrysts, mostly separated and fragmented, trace green chips with silica growth on them, trace oxide staining, 1-2% reddish brown chips, some with silica veins and weathered plagioclase.
3610-3640	**Tlpp Basalt**	Similar to 3550 but chips more variable, 60% gray basaltic andesite, trace calcite.

3640-3670	**Meta-basalt**	Hornblende, no phenocrysts, all metamorphic, finely crystalline, 2-4% plagioclase, mafics of hornblende or pyroxene, slight reaction HCl.
3670-3730	**Tlpp' Basalt/Andesite**	Slightly porphyritic, pyroxene in the basalt, fairly vitreous surface.
3730-3760	**Ts Sedimentary**	Sedimentary
3760-3830	**Tlpp' Basaltic Andesite**	Same as 3670.
3830-3920	**Metavolcanics**	Mottled green, brown-red, and metavolcanics, meta-basalts, no phenocrysts but highly mottled white splotches containing altered plagioclase, free calcite, trace pyrite, slight banding, trace chlorite
3920-3960	**Volcanics**	Altered porphyritic red altered volcanic 75%, breccia 25%, possible fault, 5-6% plagioclase and altered plagioclase phenocrysts, 1% pyroxene, some rimmed, meta-volcanic is basalt dominated, no phenocrysts.
3960-3990	**Volcanic Breccia/Andesite/Dacite**	75% andesite, 25% porphyritic red altered, overall color more of red-purplish gray, same basic lithology as 3920-3950.
4000-4030	**Tlpp' Volcanics**	Medium to dark gray, microcrysts of plagioclase laths, pyroxene, trace silica veins and chlorite staining, few chips of large silica up to 8mm, trace pyrite/chalcopyrite.
4030-4060	**Ashflow Tuff or Rhyolite**	Glassy, vitropheric, 10-15% volcanic breccia, altered plagioclase phenocrysts.
4060-4090	**Volcanics**	98% volcanic with trace basement diorite.

4090-4270	**Kqmd basement Granodiorite**	70% quartz crystals up to 4mm clear to pink to red, 10-15% quartz has oxide staining, 15% basaltic andesite, some meta-volcanic, unaltered plagioclase up to 2mm, trace mica in basalts, 5% biotite to 1mm free or in quartz chips, trace calcite as well, 2-3% pyrite.
4150-4210	**Granodiorite**	White to pink to brick red, 10% mafic volcanics reddish, no phenocrysts, chips of quartz, feldspar (potassium feldspar, plagioclase), trace pyrite, 1-2% iron oxide staining, chip of possible large quartz vein.
4210-4270	**Granodiorite**	See description at 4090 ft.
4270-TD	**Meta-basalts and Meta-andesites**	Medium gray 5% fe staining, 3% free quartz chips.

APS-3 Cuttings Analysis

Interval	**Rock Type (Abbreviations for unit names where applicable, See Figure 4 and 6)**	Description
10	**Q Sandy Siltstone**	Light brown, numerous free quartz up to 3mm, 15% rounded to subrounded volcanic gravels, mostly basalt, 1-2% mica.
20-60	**Q Very Fine Silty Sandstone**	Very light brown, 2-3% rounded volcanics ~1mm, 2% micas, muscovite, up to 8mm, increased clay content towards 50 ft.
70-130	**Q Silty Sandstone**	Light brown, sub-rounded grains, volcanic gravels up to 6 mm, free quartz up to 5mm, 2-3% muscovite.
130-190	**Q Quartz Gravels**	-10% clay/silt, 5% sand, very light brown, 65% quartz crystals up to 5mm, 1-2% muscovite, 1% volcanic gravel.
190-220	**Q Siltstone**	Light gray to light brown, 5-8% quartz, 2% micas, both 1mm or less, trace to 2% volcanics.
220- 310	**Q Silty Sandstone**	Light brown, very fine to medium grains, 2% micas up to 3mm, quartz up to 4mm, mafic gravels, rounded to sub angular, <3mm.

310- 340	**Q/Ts Volcaniclastics and Sandstone**	Red orange, plagioclase, quartz, basalt, pyroxene lithics, average 1-2mm, angular up to 6mm, light brown sandstone similar to 220-310, high oxidation.
340-370	**Ts Volcaniclastics Clay/Siltstone -**	Same as 310-340, large plagioclase up to 5mm phenocrysts, clay/siltstone off-white to light tan, micro-grains of mafics.
370-400	**Tlpa Basaltic Andesite**	Altered, medium gray with sig, plagioclase phenocrysts, 4-5%, secondary silica filling void, odd shapes up to 4mm, pyroxene up to 3mm, 1-2% quartz, significant iron oxide staining as well as very fine metallic grains.
400-430	**Tlpa Basaltic Andesite**	Slightly altered, porphyritic, secondary silica not as prevalent as 370, also highly porphyritic basalt with 20% plagioclase up to 4mm, altered basaltic andesite, see 370-400 description.
430-460	**Tlpa Basaltic Andesite**	Porphyritic, medium gray, plagioclase up to 5mm, 10-15% phenocrysts, few altered, 5% augite and clinopyroxene, 30% is altered, up to 2mm, secondary silica void filling, trace oxidation.
460-530	**Tlpa Basaltic Andesite**	Volcaniclastics 30%, red-orange color, porphyritic, plagioclase 5%, ~1mm, trace quartz, 2-4% pyroxene which 20% is altered, 5mm quartz grain.

530-670	**Tlpp Basaltic Andesite**	15% volcaniclastics, slightly altered, highly variable color, medium gray to pinkish to slightly brown to red-orange, plagioclase 2-4%, usually 1-2mm phenocrysts, some altered to clay, 2% clinopyroxene, trace alteration, up to 2mm phenocrysts, quartz and secondary silica growth common, at 570 ft gouge, mylonitic texture, not seen in the 30ft interval chips, also at 580 ft 4mm calcite crystal, alteration increases at 640, significant greenish secondary growth with lineations/slickensides at 670.
670-700	**Tlpp Andesite**	Porphyry dominated by secondary silica growth, some possible altered plagioclase, trace to 1% pyroxene, some altered, possible poor foliation of alteration, most alteration zones empty leaving pale green cavity, also reworked tuffaceous rock.
700-790	**Tlpp Basaltic Andesite**	Highly porphyritic, pinkish to bluish gray, 5% quartz and 35% plagioclase, plagioclase more euhedral up to 2mm, trace to 1% pyroxene, usually <1mm, mild oxidation, moderate weathering/alteration, possible Tpba found southwest of Astor Pass.

790-910	**Tlpp Basaltic Andesite**	Porphyritic, more altered than 700-790, 30% plagioclase up to 2mm, slightly altered, 2-3% quartz, anhedral and pore filling, some quartz veins from 790-820 and 880 ft, oxidation increasing at 880 ft as well, very trace biotite.
910-960	**Tc Volcanic Conglomerate**	Altered reddish brown volcanic (basaltic andesite) and tuffaceous rock, reddish rock has microcrysts of plagioclase, possibly pyroxene, and some quartz, tuff is off white to sometimes greenish color, biotite phenocrysts 1%, overall medium sand grain sized, with up to 10% free quartz and plagioclase grains.
980-1030 possibly to 1100	**Tuff**	Partially welded, off white to slight green, pervasive dendritic manganese oxide strings, 1-2% biotite/muscovite mostly dark green, 1% quartz anhedral, 1030 ft silica alteration, chalcedonic quartz along with the biotite bearing tuff.
Chips	**MISSING CHIPS**	**Missing from 1000-1030 and 1040-1100, as well as from 1300-1380.**
1130	**Tri Rhyolite**	Light brownish gray, 4% biotite, 4-6% quartz, mild chlorite staining with a pyrite inclusion in on larger stain, very trace amounts of pyrite elsewhere, possibly altered.

1150-1210	**Tri Rhyolite**	Light to medium gray, porphyritic, 2-3% biotite/muscovite up to 2mm, 1% quartz, trace chlorite staining, trace pyrite <1mm, trace plagioclase, trace silica veins and rhyolitic flow banding, slight iron oxidation especially towards 1210 ft.
1220	**Tri Rhyolite/Dacite & Tuff**	Rhyolite similar to 1150-1210 ft, 30% tuff or conglomerate of tuffaceous material, quartz up to 3mm, clays, <mm calcite phenocrysts.
1250-1280	**Ts Clastic Sandstones**	Medium greenish gray/brown, frags of basalt, crystals of pyroxene, quartz up to 4mm, pyrite, most crystals 1-2mm at most, coarser grains at 1300 ft, volcanic porphyritic andesite to basaltic andesite.
1310-1360	**Ts Volcaniclastics**	Similar to 1240-1300 ft, calcite veins and crystals up to 8mm, pyroxene phenocrysts in some larger mafic clasts, silica veins, pyrite up to 2mm, trace quartz to 2mm, trace oxidation.
1360-1420	**Tlpp Basaltic Andesite**	Mixing with clastics from above 15%, medium gray, porphyritic mostly pyroxene 2-5% increasing with depth and plagioclase 1% up to 2mm, trace pyrite, trace free calcite, 1360 and 1370 ft have 10% soft red clay with white clay layers interbedded, slightly altered.

1420-1450	**Ts Volcaniclastics**	Basaltic andesite chips are angular to sub rounded pebbles up to 13mm.
1450-1540	**Tlpp Basaltic Andesite**	Medium gray, porphyritic, 1-2% plagioclase up to 6mm at 1540 ft and 1% pyroxene, trace large biotite clasts with over 1cm in length at 1450 ft, trace calcite veins up to 2mm thick, trace oxidation, clay evident at 1480 and 1540 ft, trace tuffaceous material throughout.
1550-1610	**Ts Volcaniclastics**	>50% volcaniclastics, 30-40% basaltic andesite, reddish to purplish clays with mafic clasts, quartz, plagioclase, pyrite and pyroxene, some chips at 1590 ft very vitreous, meta-volcanics.
1620-1680	**Tlpp Basaltic Andesite**	Same as 1450-1540.
1660	**Ts Volcaniclastics**	Calcite and basaltic andesite dominated.
1690-1740	**Ts Volcaniclastics**	Tuffaceous rocks, rhyolite, altered rhyolite, trace pyrite, medium light gray, slightly porphyritic, large clasts of dark mica (phlogopite) up to 6-8mm at 2%, trace calcite up to 4mm, trace chlorite, sanidine.
1750-1800	**Tlpp Basaltic Andesite**	Medium dark gray, porphyritic, still vitreous, slightly metamorphosed, 1-2% pyrite, 1% micas, trace cryptocrystalline quartz, also bright purple alteration mineral, trace to 1%.

1800-2150	**Tri Rhyolite**	Light to medium gray, porphyritic, 3% dark mica, 4-5% quartz up to 8mm. 10-15% chips of dark gray vitreous mafic andesite, trace bright purple alteration min, trace to 1% pyrite, 2020-2050 ft slight purple hue as well as trace chlorite.
2150-2320	**Basalt to Andesitic Basalt**	Medium gray to green gray, porphyritic, 2-3% plagioclase to 1mm, trace to zero pyroxene/hornblende, 1% quartz. 2200-2230 ft has slight reddish hue, no oxidation.
2320-2350	**Tuff**	Medium gray, frags of basalt and andesite up to 2mm, groundmass grainy and speckled.
2350-2530	**Tlpp Basaltic Andesite**	Slightly porphyritic, medium to light gray, plagioclase 2% up to 3mm, quartz to 1mm anhedral, very small chips overall, trace iron oxidation.
2530-2560	**Ts Tuff/Volcaniclastic**	Greenish medium gray, reddish gray, green brown groundmass, crystals of plagioclase, quartz, pyroxene, 2% chlorite staining, 2% other secondary alterations, silica veins, lithic frags of basalt.
2560-2620	**Tlpp Basaltic Andesite**	Porphyritic, green gray to red gray to gray, 4% plagioclase up to 4mm, no micas, trace iron oxide, trace quartz, possible veins, possible epidote trace.
2620-2680	**Ts Volcaniclastic**	Brown-gray, quartz, plagioclase, chlorite, pyroxene.

2680-2740	**Tlpp Basalt**	Altered, reddish brown, slightly porphyritic, 2-3% void filled cryptocrystalline quartz with crystal rims, iron oxide trace, trace flow foliation.
2740-3010	**Tlpp Basalt**	Dark gray to medium gray, aphanitic to slightly porphyritic, trace pyroxene and plagioclase, 1% free quartz crystals some showing flow banding - more at 2890-2920 ft, trace iron oxidation.
3010-3160	**Tlpp Basalt**	Basalt same as above, some volcaniclastics 20%, clay/sand conglomerate with volcanic clasts, calcite up to 6mm trace, trace pyrite, chlorite, and 4-5% reddish weathered appearance.
3160-3190	**Basalt**	Similar to 3010-3160, no reddish alteration.
3190-3220	**Basalt**	Same as above.
3220-3270	**Tlpp/Ts Basalt with Volcaniclastics**	Aphanitic to slightly porphyritic, medium gray, 1% pyroxene, clastics have mostly basalt and some andesite frags, also prevalent greenish clay-like alteration with strong reaction HCl, trace calcite and iron oxidation.
3270-3290	**Tlpp Basalt**	Majority altered, reddish brown, small chips likely porphyritic, 1% chips of plagioclase, trace calcite, unaltered dark gray basalt slightly vitreous.

3290-3650	**Tlpp' Basaltic Andesite**	Medium dark gray to brown gray, aphanitic, groundmass 5% microcrysts of plagioclase and altered green pyroxene, trace loose calcite, 5-10% reddish color alteration throughout, trace iron oxidation.
3650-3740	**Tlpp' Basaltic Andesite**	Rock same as 3290 to 3650 ft interval, with 15% clay, sample didn't wash well.
3740-3830	**Clastics with Basalt**	Dark gray, aphanitic, microcrysts of plagioclase in groundmass, 10% meta-volcanics.
3830-3890	**Clastics/Breccia/Basalt**	Brick red gray, aphanitic, trace calcite.
4110-4140	**Tri Rhyolite**	Vitrophyre, rhyolite mixing with granodiorites.
3890-4170	**Meta-Basaltic Andesite**	Medium gray with some brick red, microcrystalline plagioclase pyroxene and hornblende, 1-2% chips quartz, 1-2% Iron oxide staining, trace bright purple secondary alteration.
4170-4320	**Kqmd Granodiorite**	Basement, white to pink, 40-50% quartz, 5% micas, mostly biotite, possibly phlogopite, white feldspar, 1-2% pyrite, trace calcite staining, trace iron staining.
4320-4380	**Meta-volcanics**	50% volcanics, 30% granodiorite, mica schist 20%.
4380-4400	**Granodiorite**	Same as 4170 ft with 10% meta-volcanics and mica schist.
4400-TD	**Granodiorite**	Same with 5% mica schist.